ELECTRON CAPTURE BY MULTIPLY CHARGED IONS

by

GHULAM DASTGIR ALAM QASMI

Thesis presented for the Degree of

Doctor of Philosophy

in the Faculty of Science of the

University of London.

Experimental Atomic Physics.

University College
London.
February, 1967.

A B S T R A C T

The differential electron capture probabilities were measured for the processes $O^{++} + Ne \longrightarrow O^{+} + Ne^{+}$ and $O^{++} + He \longrightarrow O^{+} + He^{+}$ at impact energies of 1200 and 2600 eV. The mass analysed O^{++} beam was injected into a single collision reaction region and scattered O^{+} and O^{++} ion intensities measured as a function of angle. This angular data was reduced in terms of the differential electron capture probabilities as a function of impact parameter.

The results are qualitatively compared with the theoretical predictions of the semi-classical impact parameter treatment and those based on the pseudo-crossing of potential energy curves. The form of the oscillations in the 1200 eV data for the (O^{++},Ne) reaction is similar to those encountered in singly charged ion-atom collisions in the absence of curve crossing. However the oscillations in the 2600 eV impact energy data for (O^{++},Ne) and the 1200 eV data for (O^{++},He) indicate that curve crossing takes place.

It is possible that experiments of this type could be used to provide, by inspection of the probability functions, a test for whether curve crossing takes place although there is as yet no corroborative body of experimental evidence.

C O N T E N T S

CHAPTER I

INTRODUCTION TO THE PRESENT WORK

The study of the charge transfer or electron capture process was stimulated because of the important role they play in geophysics, physics of the upper atmosphere, controlled fusion reactions and the design of tandem accelerators. The reactions in which hydrogen atoms lose an electron are involved in the trapping of protons in the earths magnetic field and the lifetime of the trapped proton is determined by their cross-sections for electron capture. In controlled fusion research where the primary object is to create a hot plasma, the electron capture with the background gas acts as a heat sink and makes the attainment of high temperatures extremely difficult. Similarly in tandem accelerators where the primary ion beam has a long path length to cover, the electron capture not only results in a considerable loss of the beam intensity but also mixes neutrals in the beam as an impurity. This process is therefore the subject of many experimental and theoretical investigations in many laboratories of the world. The experimental studies are further motivated from an academic point of view by a need for data to which theoretical predictions could be compared.

The theoretical investigations divide the charge transfer process into two main classes, namely,

$$A^+ + A \longrightarrow A + A^+ \qquad 1.1$$

called the symmetric resonance and

$$A^+ + B \longrightarrow A + B^+ + \Delta E \text{ (energy defect)} \qquad 1.2$$

called the asymmetric process. The energy dependence of the cross-sections for 1.1 is different from 1.2. In the former case, the cross-section for atomic ions increases monotonically with the decrease of the impact energy whereas for the latter, the cross-section is in general very small at low impact energies, rises to a maximum and then decreases rapidly at higher energies. The maximum of the cross-section occurs at the velocity v_m given in terms of Massey's[1a] "Adiabatic Criterion" as

$$v_m \approx \frac{a\ \Delta E}{h} \qquad 1.3$$

where a represents the range of interaction, ΔE the energy defect of the process and h the Plank's constant. Thus within the adiabatic region where $v < \frac{a\ \Delta E}{h}$ the cross-sections are small for the asymmetric process. However there are a few exceptions to this rule, particularly the partial charge transfer process of the type

$$A^{n+} + B \longrightarrow A^{(n-m)+} + B^{n+} + \Delta E \qquad 1.4$$

where within the adiabatic region, the cross-sections have been observed to be large followed by a flat maximum which does not correspond to the adiabatic criterion as far as the position of the maximum is concerned. This is believed to be due to the pseudo-crossing of the potential energy curves which represent respectively the left and right hand sides of 1.4

The Landau-Zener[2,3a] formula has been applied to a number of charge transfer processes of the type 1.2 in which pseudo-crossing of the potential energy curves exists[4a]. However, the formula was derived on very strong assumptions, some of which are rather unlikely to be fulfilled for real systems, In particular it was assumed that the interactions can only take place at the crossing point. Bates[5a] has shown that in fact the width of the zone around which transitions are likely is given by

$$\Delta Z_a \simeq 0.49 \left| h_{nm}(Rc) \right|^2 Z_c^2$$

where

$$h_{nm}(R) = \int \phi_n \, H \, \phi_m \, dr$$

is the interaction matrix element between the initial state ϕ_n and the final state ϕ_m, H being the Hamiltonian. If the interactions are strong this width may be considerable and in some cases of the order of interaction range. Also recent calculations by Ellison and Borowitz[6a] based on equal exponential model and Bates, Stewart and Johnston's[7a] calculations based on the numerical integration of the coupled equations of the two-state approximation, show that for the systems for which pseudo-crossing of the potential energy curves exist, transitions can take place not only at the crossing point but also in the vicinity of the crossing point and contrary to the Landau-Zener theory the transition probability is an oscillating function of the impact parameter of the colliding system.

It was, therefore, decided to study this transition probability as a function of the impact parameter experimentally. For such a study an experiment based on the primary analysis method of Everhart[8a] was found to be most suitable, since the angular distribution of ions suffering electron capture lends information on the dependence of the electron capture probability on the impact parameter. At a fixed scattering angle the impact parameter is a function of the impact energy and at fixed energy it is a function of the scattering angle.

The partial charge transfer reaction of the type

$$A^{n+} + B \longrightarrow A^{(n-1)+} + B^{+} + \Delta E \qquad 1.3$$

for the multiply charged ions provides an interacting system in which there exists a pseudo-crossing of the potential energy curves at a calculable nuclear separation. The fast primary ions A^{n+} and the electron capture product $A^{(n-1)+}$ have the same energy since in such a collision practically no energy is transferred. It is therefore, comparatively simple to separate the two charge states A^{n+} and $A^{(n-1)+}$ with an electrostatic analyser rather than to use the magnetic analysis as used by Fedorenko et al[9a].

If $N^{n+}(\theta)$ and $N^{(n-1)+}(\theta)$ are respectively the number of A^{n+} and $A^{(n-1)+}$ scattered in the direction θ, then the electron capture probability is given by

$$P(\theta) = \frac{N(\theta)^{(n-1)+}}{N(\theta)^{n+} + N(\theta)^{(n-1)+}}$$

Due to the fact that the theoretical calculations and the Landau-Zener formula apply mainly to S - S transitions, the choice of reactions under study were limited to

$$O^{++} + Ne \longrightarrow O^{+} + Ne^{+} + \qquad 1.5$$

and

$$O^{++} + He \longrightarrow O^{+} + He^{+} \qquad 1.6$$

The second chapter is mainly concerned with the theoretical work applicable to electron capture processes with special reference to the pseudo-crossing of the potential energy curves. The third chapter deals with the experimental techniques for the study of electron capture processes. In the fourth chapter, the apparatus which was designed for the measurement of angular distributions of ions suffering electron capture is discussed in detail. The fifth chapter deals with the experimental data and how it is expressed in terms of the transition probability and the impact parameter, to render it suitable for comparison with the recent developments of the theoretical calculations. This is followed by discussion of the results obtained.

CHAPTER II

THEORY OF CHARGE TRANSFER PROCESSES

2.1 INTRODUCTION

The electron capture or charge transfer process involves the transfer of an electron from the target to the projectile and can be classified into the following classes :

$$A^+ + A \longrightarrow A + A^+ \qquad \text{(symmetric resonance)} \qquad 2.1$$

$$A^+ + B \longrightarrow A + B^+ + \Delta E \qquad \text{(asymmetric)} \qquad 2.2$$

$$A^{2+} + B \longrightarrow A + B^{2+} + \Delta E \qquad \text{(double electron capture)} \qquad 2.3$$

$$A^{n+} + B \longrightarrow A^{(n-1)+} + B^+ + \Delta E \qquad \text{(partial charge transfer)} \qquad 2.4$$

where ΔE is the energy defect of the process. From the theoretical point of view, being many body problems these are as yet incapable of exact quantum mechanical solution except in the case of simpler systems such as $p + H \longrightarrow H + p$.

In all other cases one has to resort to approximate methods which are then naturally valid only for a limited velocity range, different approximations being applicable to different velocity ranges. For this reason the velocity region has been arbitrarily divided into three ranges to be called 'high', 'intermediate' and 'low'. According to Rapp and Francis [1] the dividing line between low, intermediate and high velocity is taken as 10^5 cm/sec and 10^8 cm/sec. For velocities $> 10^8$ cm/sec, where

$$\frac{e^2}{\hbar v^2} \leq 1$$

the Born approximation has been successfully applied to a number of charge transfer processes e.g., McCarrol[2], Schiff[3], Bransden[4].

In the low and intermediate velocity range two methods have been employed, namely, the wave treatment in which both the electronic and molecular motions are described by the wave-functions, the scattered wave approximation being an example, and the impact parameter treatment where the nuclear motion is described by the classical orbits and the electronic motion by the quantum mechanical wave-functions. The impact parameter treatment is thus valid only when the de Broglie wavelength of the incident particle is sufficiently small so that the classical trajectory of the particle is a good description of the wave packet motion. Because of its relative simplicity, this treatment has been extensively applied to the charge transfer processes. It has been shown by Gurnee and Magee[5] that in the intermediate velocity range the impact parameter treatment is identical to the more rigorous wave treatment.

The following section will therefore be concerned with the theory of the charge transfer in the intermediate velocity range studied in terms of the impact parameter treatment.

2.2 General Mathematical formalism of the impact parameter treatment.

Consider the general charge transfer process

$$A^+ + (B^+ + e) \longrightarrow (A^+ + e) + B^+ + \Delta E \qquad 2.5$$

During the collision the system $(A^+ + B^+ + e)$ can be considered as a pseudo-molecule with $\left[(A^+ + e) + B^+\right]$ and $\left[A^+ + (B^+ + e)\right]$ as two

asymptotic states. The single valence electron can be either attached to A^+ or B^+ and it is assumed that the total wave function ψ which represents the system $(A^+ + B^+ + e)$ can be expanded as a linear combination of the orbital wave-functions of the electron around A^+ and B^+, thus

$$\psi = C_A(t)\,\phi_A(r_A)\exp\left(-\frac{i\,E_A t}{\hbar}\right) + C_B(t)\,\phi_B(r_B)\exp\left(\frac{-i\,E_B t}{\hbar}\right) \qquad 2.6$$

where the C's are the time dependent coefficients of the expansion, ϕ_A and ϕ_B are the atomic orbitals for the electron on nuclei A^+ and B^+; r_A and r_B the distances of the electron from A^+ and B^+. E_A and E_B are the eigen energies. ϕ_A and ϕ_B satisfy the Schrödinger equation

$$\left[\left(-\frac{\hbar}{2m_e}\right)\nabla^2 + V_A(r_a) - E_A\right]\phi_A = \left[\left(-\frac{\hbar}{2m_e}\right)\nabla^2 + V_B(r_b) - E_B\right]\phi_B = 0 \qquad 2.7$$

If H is the total Hamiltonian of the system $(A^+ + B^+ + e)$, then ψ satisfies the Schrödinger time dependent equation

$$H\psi = i\hbar\frac{\partial\psi}{\partial t} \qquad 2.8$$

where

$$H = \left[\left(-\frac{\hbar}{2m_e}\right)\nabla^2 + V_A(r_a) + V_B(r_b)\right] \qquad 2.9$$

substituting 2.6 in 2.8 and making use of 2.7, we get

$$C_A\phi_A\exp\left(\frac{-i\,E_A t}{\hbar}\right)V_B + C_B\phi_B\exp\left(-\frac{E_B t}{\hbar}\right) = i\hbar\frac{dC_A}{dt}\phi_A\exp\left(-\frac{iE_A t}{\hbar}\right) + i\hbar\frac{dC_B}{dt}\phi_B\exp\left(-\frac{iE_B t}{\hbar}\right) \qquad 2.10$$

Alternatively multiplying by ϕ_A^* and ϕ_B^* and integrating over all space two coupled differential equations in C_A and C_B are obtained, which after simplification are

$$i\,\dot{a}_B = K_1(t)\,\exp(i\,\Omega\,t)\,a_A \qquad 2.11$$

$$i\,\dot{a}_A = K_2(t)\,\exp(-i\,\Omega\,t)\,a_B \qquad 2.12$$

where

$$K_1 = \frac{(V_B)_{BA} - S(V_B)_{AA}}{(1 - S^2)\,\hbar}, \qquad K_2 = \frac{(V_A)_{AB} - S(V_A)_{BB}}{(1 - S^2)\,\hbar}$$

$$\Omega = \omega t + \int_{-\infty}^{t} (\eta_1 - \eta_2)\,dt, \qquad \omega = \frac{E_B - E_A}{\hbar} \qquad 2.13$$

$$\eta_1 = \frac{(V_A)_{BB} - S(V_A)_{AB}}{(1 - S^2)\,\hbar} \qquad \eta_2 = \frac{(V_B)_{AA} - S(V_B)_{BA}}{(1 - S^2)\,\hbar}$$

$$(V_A)_{AB} = \int \phi_A^*\, V_A\, \phi_B\, d\tau, \quad S = \int \phi_A^*\, \phi_B\, d\tau = \int \phi_B^*\, \phi_A\, d\tau \qquad 2.14$$

The coefficients a_A and a_B differ from C_A and C_B only in phase.

The integrals in 2.14 are functions only of R, the internuclear separation, and from the classical collision

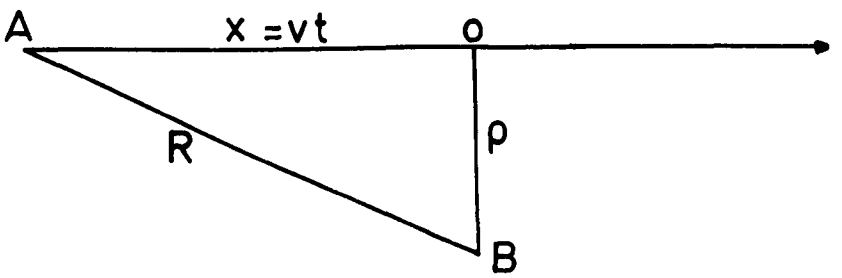

FIG. 2.1

trajectory x = vt of Figure 2.1, are therefore, functions of time and the impact parameter. $|a_A|^2$ and $|a_B|^2$ are respectively the probabilities of locating the electron on A^+ and B^+ at any particular time and since initially ($t = -\infty$), the electron is located on B^+, we have the initial conditions,

$$\begin{aligned} &\text{(i)} \quad a_A(-\infty) = 0 \\ &\text{(ii)} \quad a_B(-\infty) = 1 \end{aligned} \qquad 2.15$$

The probability of locating the electron on the nucleus A^+ after the collision is $|a_A(+\infty)|^2$, which can be determined from the coupled equations 2.11 and 2.12 subject to the boundary conditions laid down in 2.15. The charge transfer probability $P = |a_A(+\infty)|^2$ is thus a function of the impact parameter. The cross-section can then be calculated by integrating this probability over all values of the impact parameter, i.e.,

$$\sigma = \int_0^\infty 2\pi P \rho d\rho \qquad 2.16$$

If it is assumed that the expansion of the wave-function for the quasi-molecule formed by ($A^+ + B^+ + e$) in terms of the atomic orbitals of A and B is correct, then the treatment so far is general and correct and is applicable to both symmetric and asymmetric charge transfer processes.

2.3 Symmetric Resonance Process.

In the symmetric resonance $A^+ + A \longrightarrow A + A^+$ if it is assumed that only two states i.e. the initial and the final

are involved and there is no coupling between other states, then in equation 2.11 and 2.12,

$$K_1 = K_2 = K$$

$$E_B - E_A = o = \eta_1 - \eta_2$$

which simplify the equations 2.11 and 2.12 to

$$\frac{i\, da_B}{dt} = K a_A \qquad 2.17$$

and

$$\frac{i\, da_A}{dt} = K a_B \qquad 2.18$$

These equations can be solved exactly to give the probability for the symmetric case

$$P_{sy}(\rho, v) = \sin^2 \int_{-\infty}^{+\infty} \frac{K}{2hv}\, dx \qquad 2.19$$

in which we put dx = vdt. At finite internuclear separation there are two stationary state wave-functions for the molecule A_2^+, namely (A^+A) and (AA^+), one being a symmetric combination of the atomic wave-functions and the other anti-symmetric. At a given internuclear separation R, the two states have the energies E_s and E_a respectively, with $E_s < E_a$, the example being the two states $2\Sigma_u$ and $2\Sigma_g$ of the H_2^+ molecule. Pauling and Wilson[6] have shown that the combination of the matrix element K is given by

$$K = (E_a - E_s) \qquad 2.20$$

thus

$$P_{sy}(\rho,v) = \sin^2 \int_{-\infty}^{+\infty} \frac{E_a - E_s}{2 h v} \, dx \qquad 2.21$$

The energy difference $(E_a - E_s)$ has been evaluated accurately[8] for the simplest of the collision problems,

$$H^+ + H \longrightarrow H + H^+$$

and less accurately[9] for

$$He^+ + He \longrightarrow He + He^+$$

for which the atomic wave-functions are known, but for all other complex systems approximate wave-functions must be used. Gurnee and Magee[5], for example, use one electron nodeless slater wave-function[10]

$$\varphi(r) = r^{n-1} e^{-\alpha r} \qquad 2.22$$

where n and α are adjustable parameters for different atoms. Rapp and Francis[1] use semi-empirical orbitals of the type

$$\varphi = (\pi a_o^3)^{-\frac{1}{2}} \left(\frac{I}{13.6}\right)^{3/4} \exp\left[-\left(\frac{I}{13.6}\right)^{\frac{1}{2}} \frac{r}{a_o} \right] \qquad 2.23$$

where a_o is the radius of the first Bohr orbit, and I the ionization potential in eV. They obtain

$$(E_a - E_s) = 2I\left(\frac{R}{a_o}\right) \exp\left[- \left(\frac{I}{13.6}\right)^{\frac{1}{2}} \frac{R}{a_o} \right] \qquad 2.24$$

which on substitution in 2.21 gives

$$P_{sy}(\rho,v) = \sin^2 \int_{-\infty}^{+\infty} \frac{I}{a_o h v} (x^2 + \rho^2)^{\frac{1}{2}} \exp\left[- \frac{I}{13.6}^{\frac{1}{2}} \frac{x^2 + \rho^2}{a_o} \right]^{\frac{1}{2}} dx \qquad 2.25$$

in which the relation $R^2 = x^2 + \rho^2$ has been used.

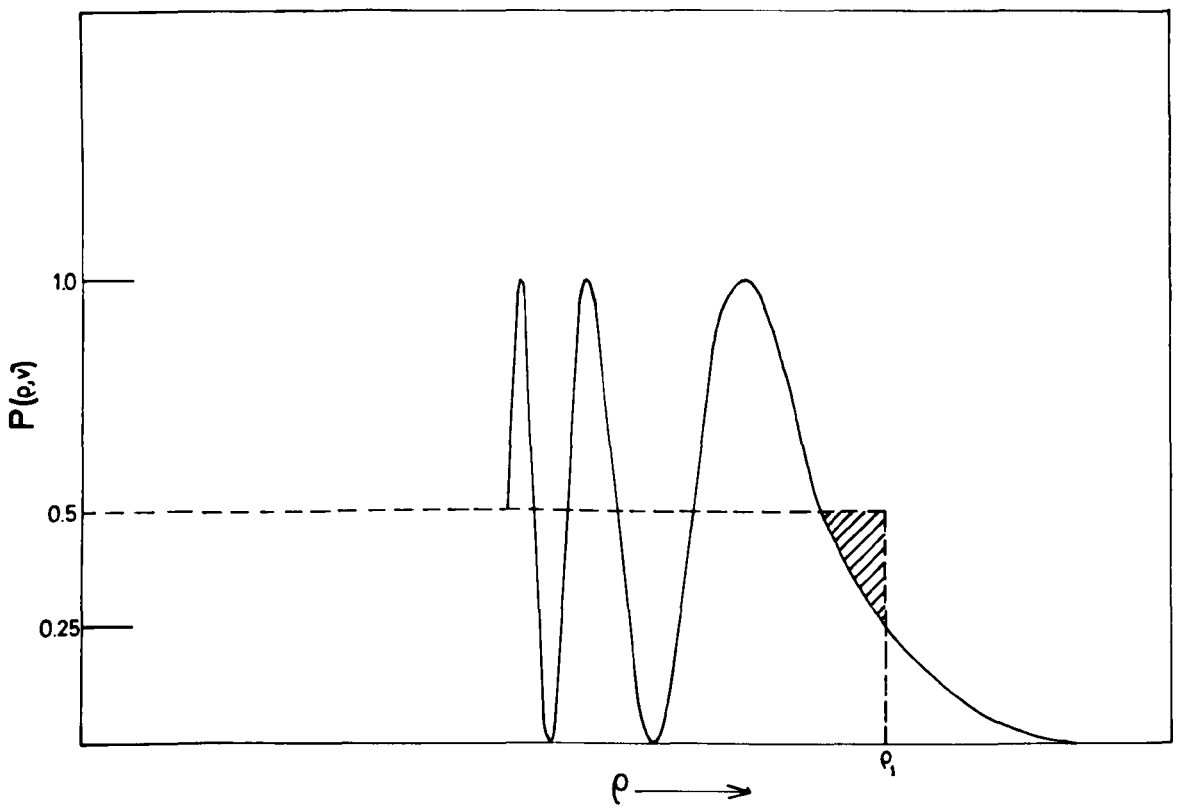

FIG. 2.2

The integral in 2.25 has been evaluated by Dalgarno[11] in terms of the Bessel functions and the result for $(\frac{I}{13.6})\ \frac{\gamma\rho}{a_o} \gg 1$, simplifies to

$$P(\rho,v) = \sin^2\left[\left(\frac{2\pi}{a_o\gamma}\right)^{\frac{1}{2}}\left(\frac{I}{h\nu}\right)\rho^{3/2}\left(1+\frac{a_o}{\gamma\rho}\right)\exp\left(-\frac{\gamma\rho}{a_o}\right)\right] \qquad 2.26$$

$$\gamma = \frac{I}{13.6}$$

This probability, shown in Figure 2.2 is seen to oscillate between 0 and 1 at small ρ and finally decays exponentially to zero at large ρ. Rapp and Francis approximate the probability to 0.5 up to an impact parameter ρ_1 as indicated in the figure, ρ_1 being the point where $P_{sy}(\rho,v)$ falls to 0.25, thus

$$\sigma_{sy} = 2\pi\int P_{sy}(\rho,v)\ \rho\ .d\rho \qquad 2.27$$

$$= \frac{1}{2}\pi\rho_1^2$$

ρ_1 is given by the equality

$$P(\rho_1,v) = \frac{1}{4} = \sin^2 A(\rho_1,v) \qquad 2.28$$

i.e;

$$A(\rho_1,v) = \left(\frac{2\pi}{\gamma a_o}\right)^{\frac{1}{2}}\left(\frac{I}{h\nu}\right)\rho_1^{3/2}\left(1+\frac{a_o}{\gamma\rho_1}\right)\exp\left(\frac{-\gamma\rho_1}{a_o}\right) = \frac{\pi}{6} \qquad 2.29$$

Equation 2.27 can be simplified to give

$$\sigma_{sy}^{\frac{1}{2}} = K_1 - K_2 \log v \qquad 2.30$$

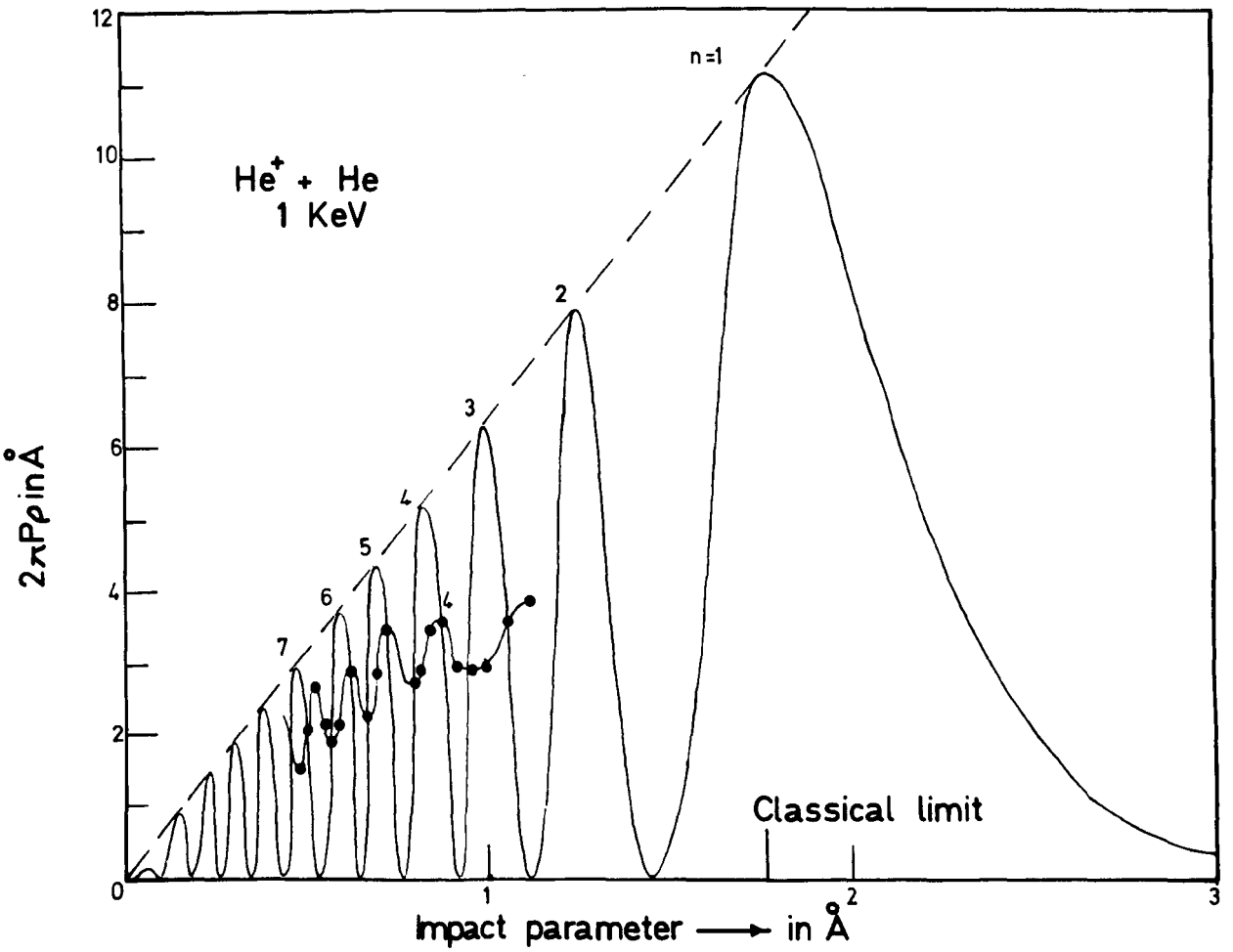
12
10
8
6
4
2
0
$2\pi P\rho$ in Å
$He^+ + He$
1 KeV
n=1
2
3
4
5
6
7
4
4
Classical limit
1
2
3
Impact parameter ⟶ in Å

FIG. 2.3

where K_1 and K_2 are constants depending only on the ionization potential I. This equation has been used for extrapolating charge transfer data over velocity ranges but it is improbable that such a simple law holds over more than a limited range of energies.[12]

The differential measurements by Everhart et al[13] of the charge transfer probability P in

$$He^+ + He \longrightarrow He + He^+$$

at 1 keV are plotted vs impact parameter in Figure 2.3 and compared with the predictions of the impact parameter treatment method. Although the experimentally observed oscillations do not range from zero to unity, the location of peaks is in good agreement and points to the success of the impact parameter treatment of the problem. Such oscillations have also been observed by Jones et al[14] for

$$Ar^+ + Ar \longrightarrow Ar + Ar^+$$

at 240 eV; although these have not been compared with the theory.

A comparison of Rapp and Francis' calculations for the processes

$$p + H \longrightarrow H + p \qquad 2.31$$

and

$$Kr^+ + Kr \longrightarrow Kr + Kr^+ \qquad 2.32$$

is compared with the experimental data in Figure 2.4. The experimental data for the process 2.31 is due to Fite et al[15] while for the process 2.32, the data is due to Hasted[16], Kushnir et al[17] and Flaks et al[18]. It is seen that in general the agreement is good.

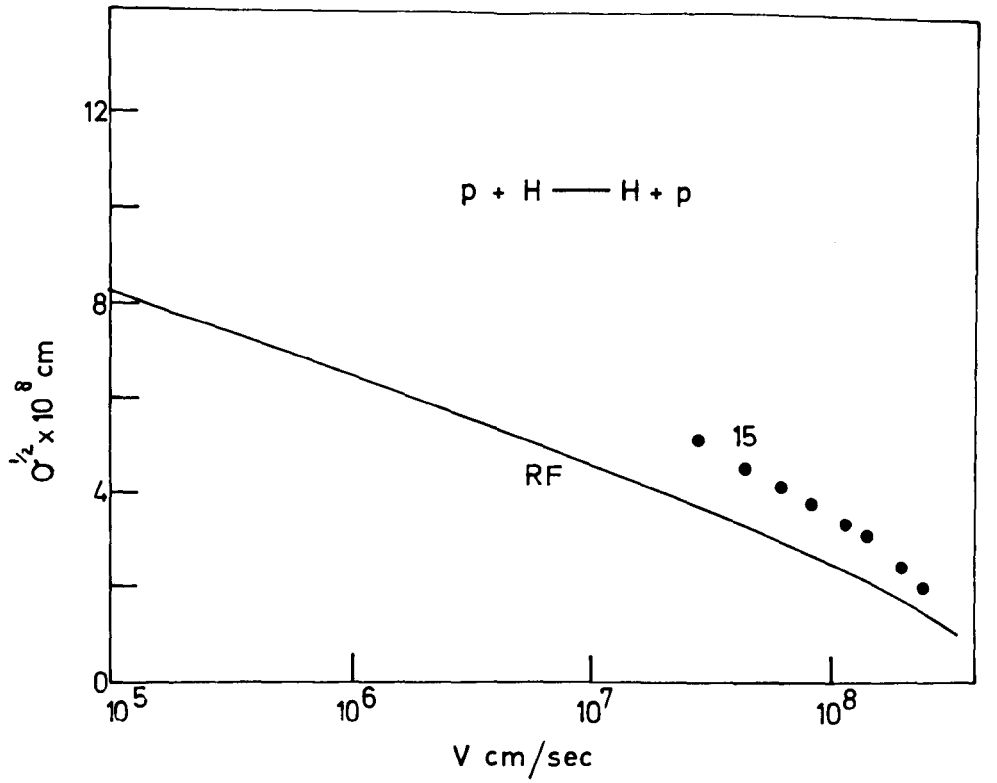
p + H —— H + p
RF
15
$\sigma^{1/2} \times 10^8$ cm
V cm/sec
0
4
8
12
10^5
10^6
10^7
10^8

FIG. 2.4

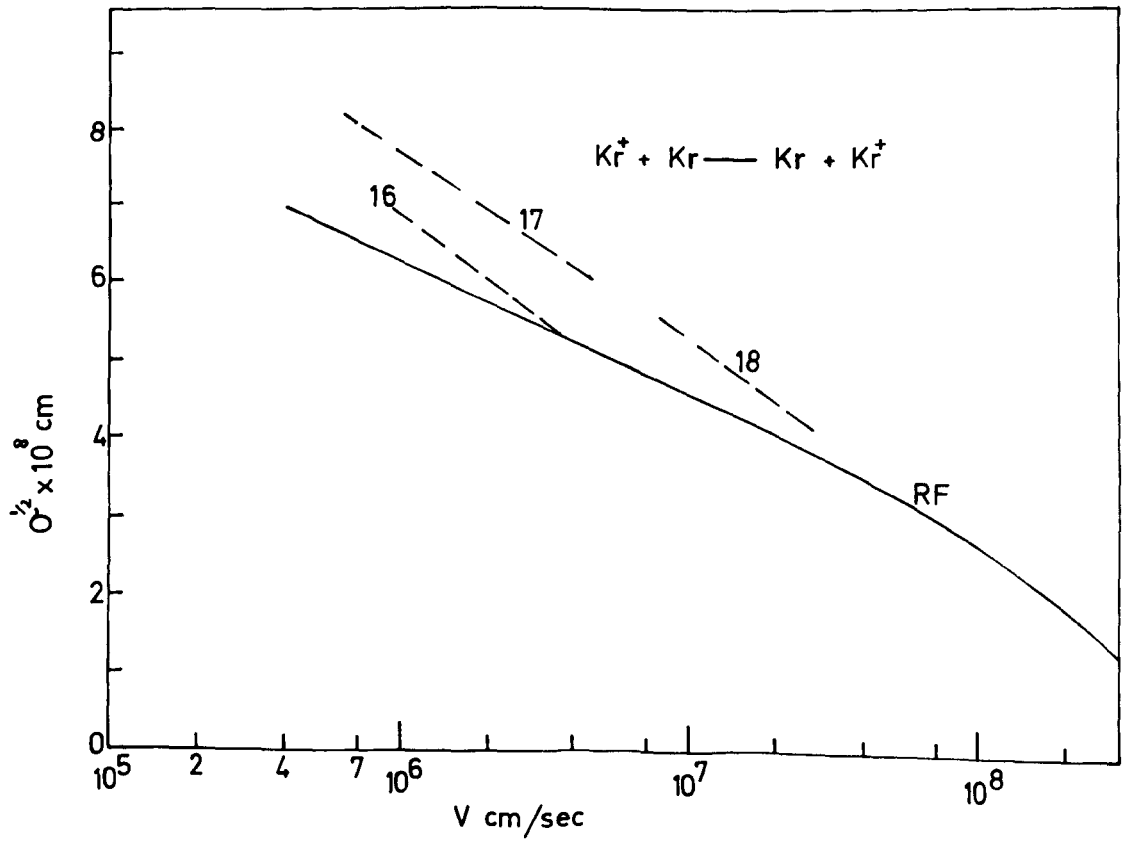
$Kr^+ + Kr$ —— $Kr + Kr^+$
16
17
18
RF
$\sigma^{1/2} \times 10^8$ cm
V cm/sec
0
2
4
6
8
10^5
2
4
7
10^6
10^7
10^8

2.4 Asymmetric charge transfer process

The impact parameter treatment when applied to the asymmetric process $A^+ + B \longrightarrow A + B^+ + \Delta E$ is faced with two problems not encountered in the symmetrical resonance case.

Firstly, the difficulty in assigning molecular orbitals to the collision complex $(AB)^+$ which in this case goes to two different asymptotic forms as $R \longrightarrow \infty$, namely $(A^+ + B)$ and $(A + B^+)$, separated by an energy ΔE, whereas in the symmetric case there is only one asymptotic state $(A + A^+)$. Rapp and Francis use the semi-empirical orbitals of 1.23 where I is the mean of the ionization potentials of A and B.

Secondly the principle of detailed balance, which states that the probability of a transition for a process and its reversal are equal, is not satisfied. In a charge transfer process there is a transition from one electronic state to another and in the intermediate velocity range where the impact parameters are large, it is assumed that spin and angular momentum are conserved. In other words transitions leading to charge transfer only occur to identical symmetry states of the AB^+ complex. Now the collision complex may dissociate into a number of states all of which do not lead to charge transfer. The statistical weight factor f, is the ratio of the states which lead to the charge transfer and the total number of states to which the collision complex $(AB)^+$ can dissociate. Similarly f_2 is the corresponding statistical weight factor for the process in the reverse direction. The principle of detailed balance requires that

$$\frac{\sigma_{\text{forward}}}{\sigma_{\text{backward}}} = \frac{f_1}{f_2}$$

This requirement is not satisfied for the asymmetrical process by the equation 2.11 and 2.12 since $K_1 \neq K_2$. To satisfy the principle of detailed balance an arithmetic mean of K_1 and K_2 is used, equations 2.11 and 2.12 can then be written as

$$\frac{ivda_B}{dx} = a_A \bar{K}(x) \exp\left(\frac{i w x}{v}\right) \qquad 2.33$$

and

$$\frac{ivda_A}{dx} = a_B \bar{K}(x) \exp\left(\frac{-i w x}{v}\right) \qquad 2.34$$

$$w = (E_B - E_A)/\hbar,$$

with $a_A(-\infty) = 1$, $a_B(-\infty) = 0$, and $P = f_1 \, a_B(+\infty)^2$

2.4.2 Behaviour of asymmetric charge transfer with impact energy. "The Adiabatic Maximum Rule".

$\bar{K}(x)$ in the above equations is a bell shaped function of x with a maximum at x = 0 and decreasing to zero at $\pm\infty$. At high velocities when $\frac{wx}{v} \ll 1$, the exponential term in (2.33), and (2.34) may be set equal to 1, giving

$$\frac{ivda_B}{dx} = a_A \bar{K}(x)$$

and

$$\frac{ivda_A}{dx} = a_B \bar{K}(x)$$

which being identical with the corresponding equation for the symmetrical

resonance case, shows that the behaviour of the asymmetrical cross-section at high velocities is similar to that of the symmetric resonance cross-sections. In this velocity range the cross-section increases with decreasing velocity because an increase in the time of collision results in an increase of the corresponding electron transition probability. This situation does not extend to low velocities since the exponential terms in 2.33 and 2.34 begin to oscillate wildly and reduce $a_B(+\infty)^2$ despite the factor $\frac{1}{v}$ acting weakly in the opposite direction. Thus at lower velocities where $\frac{wx}{v} \gg 1$, $a_B(+\infty)^2$ falls off rapidly with decreasing velocities. This region of the impact energy is termed the "Adiabatic Region" proposed by Massey[19]. The projectile velocities in this region are comparable to the electronic orbital velocities and the collision time is long enough for the electron to adjust its motion to the outside perturbations. This makes the transition an unlikely event at very low velocities. The collision in this region is an adiabatic process and the electron capture cross-sections are very low. At some nuclear separation a, where $\frac{wa}{v} \approx 1$ the charge transfer cross-section will be a maximum, and

$$\frac{w\,a}{v} = \frac{\Delta E\ a}{\hbar v} = 1$$

$$a\ \frac{\Delta E}{h} = \left[\frac{2eE}{300M}\right] \qquad 2.35$$

terminates the adiabatic region. E is the energy defect of the process and a is called the adiabatic parameter. Equations 2.35 may be written in the form

$$V_{max} = \left(1.76a\,\Delta E\right)^2 M$$

where V_{max} is the energy in eV at which the cross-section attains its maximum value, M is the mass number of the impacting species, a is given in Å, and ΔE in eV. The value of 7 Å for 'a' is constant[20,21] over a wide range of atomic system and is a useful tool to predict the energy of the cross-section function maximum. Hasted and Lee[22] include in the energy defect ΔE, the contributions for Coulomb and polarization interactions which reduce the probable error for the adiabatic parameter a $\sim$7 Å from 65% to 20% for the charge transfer.

2.4.3 Approximate computations of the asymmetric charge transfer cross-sections.

Using semi-empirical wave-function 2.23, with I as the mean of the ionization potentials of A and B, Rapp and Francis[1] obtain the transition probability $P_{asy}(\rho,v)$ for the asymmetrical case as

$$P_{asy}(\rho,v) = f_1 \, P_{sy}(\rho,v) \, \mathrm{sech}^2 \left[\frac{w}{v} \, \frac{a_o \pi \rho}{2\gamma} \right]^{\frac{1}{2}} \qquad 2.36$$

and the cross-sections for the three regions of energy have been computed as follows:

Figure 2.5 shows $P_{sy}(\rho,v)$

and $\mathrm{sech}^2 \left[\frac{w}{v} \, \frac{a_o \pi \rho}{2\gamma} \right]^{\frac{1}{2}}$ plotted

against ρ for different energy ranges.

i. When $\frac{w}{v} \ll 1$, for high velocities, the sech^2 function is represented

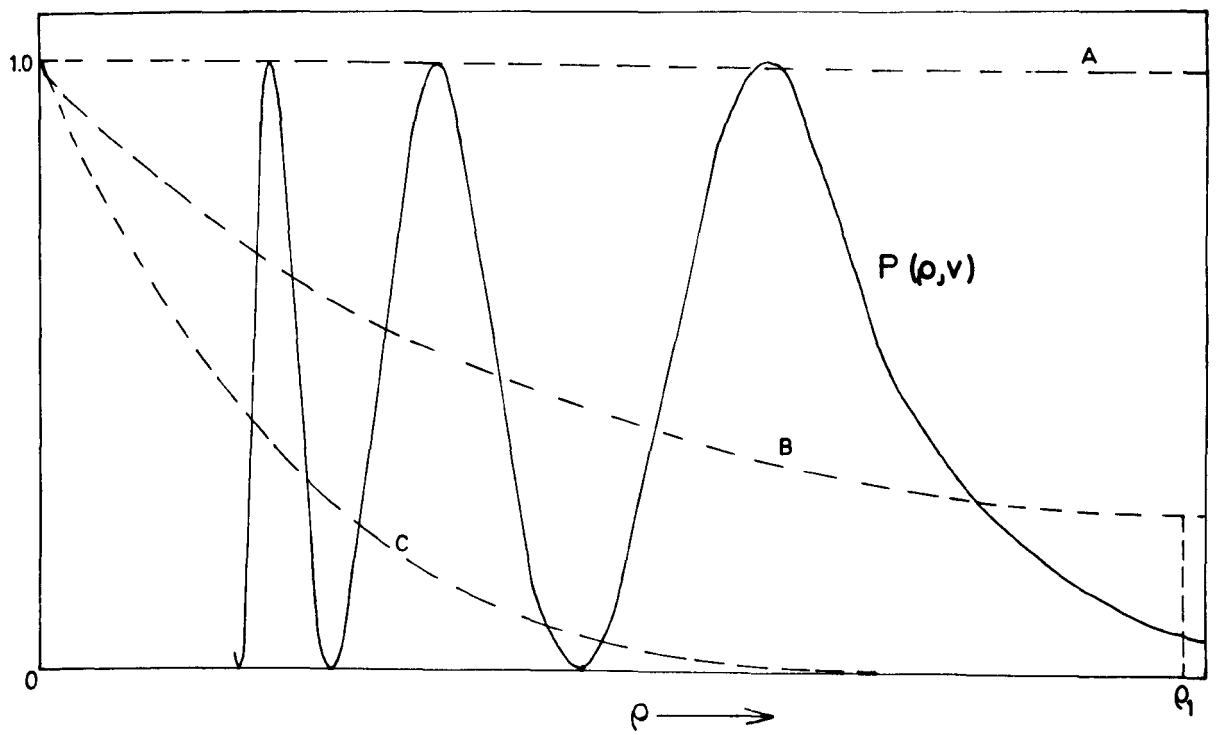

FIG. 2.5

by the curve A and remains unity over the important range of ρ. The behaviour of the asymmetric charge transfer cross-section is therefore the same as for the symmetric resonance case given by equation 2.30.

ii. For intermediate velocities where $\frac{w}{v} \approx 1$, the sech^2 function is given by curve B in which case $P_{sy}(\rho,v)$ can be replaced by 0.5 with an upper limit of ρ , in this case taken at a point such that

$$\text{sech}^2 \left[\frac{w}{v} \frac{a_o \pi \rho_1}{2\gamma} \right] = 4 P_{sy}(\rho_1, v) \qquad 2.37$$

and

$$\sigma = \tfrac{1}{2} f \int_0^{\rho_1} \text{sech}^2 \left[\frac{w}{v} \frac{a_o \pi \rho}{2\gamma} \right] 2\pi\rho d\rho \qquad 2.38$$

iii. For very low velocities when $\frac{w}{v} \gg 1$, the sech^2 function is given by the curve C_1. The sech^2 function in this case decays to zero within the important range of ρ, the upper limit in 2.38 can therefore be replaced by infinity, giving,

$$\sigma(v) = \frac{2\pi}{\alpha} \int_0^{\infty} (\text{sech}^2 u)\, u^3\, du$$

$$= \frac{9}{8} (1.202) \frac{2\pi}{\alpha^4} \qquad 2.39$$

with $\alpha = \left(\frac{\pi a_o}{2\gamma}\right)^{\frac{1}{2}} \left(\frac{w}{v}\right)$

Instead of dividing the velocity range into three regions, Hasted and Lee[23], choose the limit ρ_1 for all values of v as in the case of the symmetric resonance i.e. where

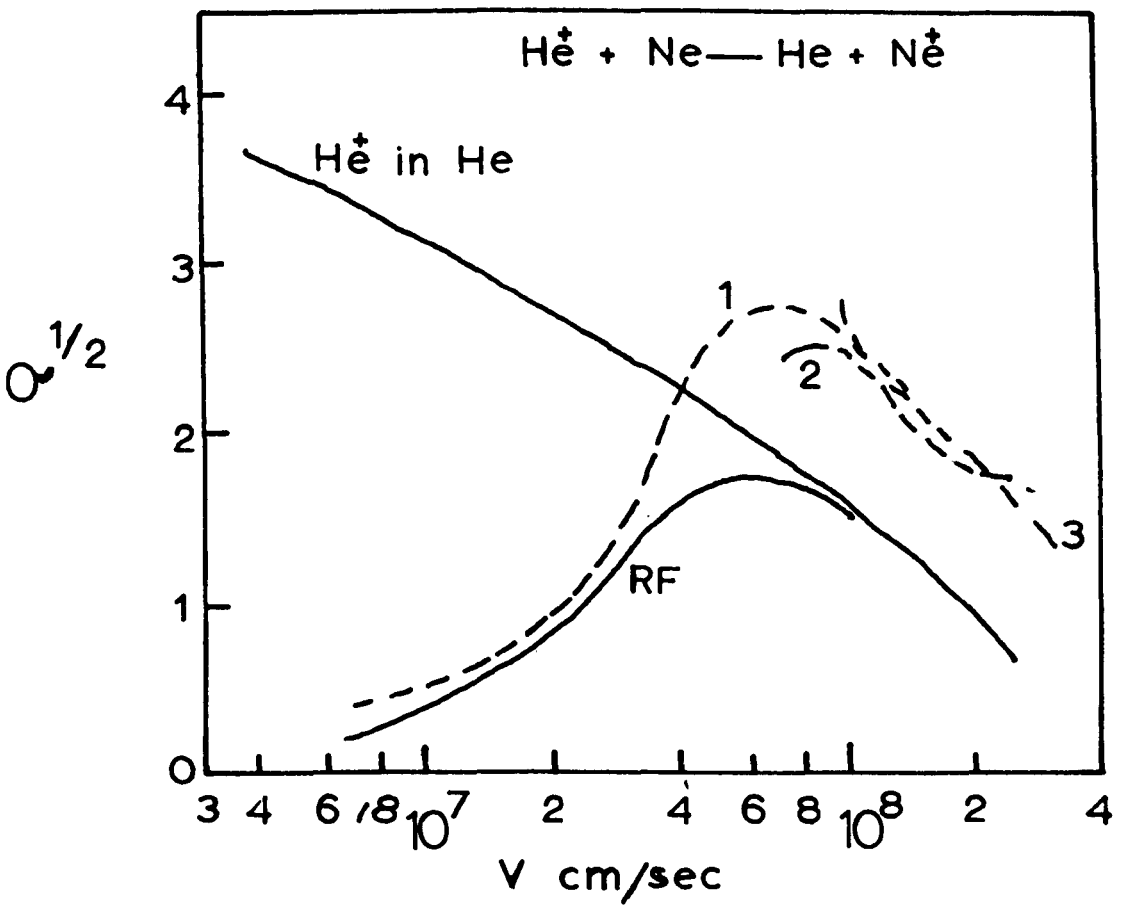
He⁺ + Ne — He + Ne⁺
He⁺ in He
1
2
3
RF
4
3
2
1
0
$\sigma^{1/2}$
3 4 6 8 10^7 2 4 6 8 10^8 2 4
V cm/sec

FIG. 2.6

$$P(\rho_1, v) = \frac{1}{4}$$

ρ_1 is then given by the equation 1.29. They obtain

$$\sigma(v) = \frac{2\pi\rho_1^2}{u_1^4} \int_0^{u_1} u^3 \operatorname{sech}^3 u \, du$$

$$= f \, \sigma_{sy}(v) \, I(u_1) \qquad 2.40$$

where $$u = \left(\frac{\pi a_o}{2\gamma}\right)^{\frac{1}{2}} \left(\frac{w\rho}{v}\right)^{\frac{1}{2}} = \alpha \rho^{\frac{1}{2}} \qquad 2.41$$

The integral $I(u_1)$ has been tabulated against u_1. $\sigma(v)$ can then be directly written down with the aid of equations 2.41 and 2.29. They have also shown that the velocity corresponding to the maximum in the cross-section function is given by

$$v^2(\sigma_{max}) = 2.95 \times 10^{14} \left(\frac{\Delta E}{\gamma}\right)^2 \left[2.54 \times 2 \log \frac{E}{\Delta E}\right] \qquad 2.42$$

Figure 2.6 shows the comparison of the theoretical and the experimental results for the process

$$He^+ + Ne \longrightarrow He + Ne^+ + \Delta E \ (3 \text{ eV})$$

together with the theoretical calculations for the resonant process

$$He^+ + He \longrightarrow He + He^+$$

The theoretical calculations are due to Rapp and Francis and the experimental data due to 1. Hasted and Stedeford[24], 2. Jones et al[25], 3. Fedorenko et al[26]. It is seen that although the qualitative shape of the $\sigma(v)$ curve agrees with the theory very well and the maxima occur

in the correct velocity region, the theoretical calculations give lower values to the $\sigma(v)$ than the experimentally determined values. This behaviour may be due largely to the approximate methods used in the calculation whereby an average ionization potential is used for both A and B.

2.4.4 Discussion of the results.

In these calculations, however, no account is taken of the possibility that the separation of the potential energy curves representing respectively the quasi-molecule $(A^+ + B)$ and $(A + B^+)$ may be smaller than the energy defect ΔE and in the absence of any interaction may be zero at a particular value of the internuclear separation R. A low value of ΔE for this R, Greatly increases the probability of the charge transfer at this point. This happens to be the case for the process 1.4, the partial charge transfer, of which

$$A^{++} + B \longrightarrow A^+ + B^+ + \Delta E \qquad 2.43$$

is a particular case. The measurements of Hasted and Smith[27] for the partial charge transfer of N^{2+}, A^{2+}, C^{2+} in He, Ne, A and Flaks and Solov'ev's measurements of Ne^{2+}, Xe^{2+} in He, Ne, A, Kr, Xe show that the cross-sections have indeed large magntiudes well within the adiabatic region and are slowly varying functions of the energy. The maximum of the cross-section is obtained at a different velocity than is predicted by the adiabatic maximum rule or for that matter by this simple form of the impact parameter treatment. Such discrepancies are not only common to the above processes but have also been observed by Gilbody and Hasted[20] for

$$Ar^+ + Kr \longrightarrow A + Kr^+$$

$$Ne^+ + Ar \longrightarrow Ne + Ar^+$$

$$C^+ + Kr \longrightarrow C + Kr^+$$

where the observed cross-section is fairly energy independent in the low energy limit and is many times larger than to be expected in a similar case such as H^+ in He. In this connection it was pointed out by them that this effect is due to the pseudo-crossing of the potential energy curves.

Since the potential energy curves play an important part in the above processes, the next sections will, therefore, be devoted to the detailed discussion of the intersection of the potential energy curves, derivation of the Landau-Zener formula and its application to the above processes in which there exists pseudo-crossing at a finite internuclear separation. More recent calculations of Bates and Johnston[28] along these lines which are relevant to the present experimental work will also be discussed.

2.5.1 Potential energy curves and their intersection

The electron capture process

$$A^+ + (B^+ + e) \longrightarrow (A^+ + e) + B^+ + \Delta E \qquad 2.44$$

where ΔE is the energy defect, involves the transfer of an electron from the nucleus B to the nucleus A. The systems on the right and left of the above equation can be considered as a quasi-molecule with the electron in different states. Unlike the atomic case where the energy levels are certain numbers, the electron terms in molecules are not numbers but functions of the distance between the nuclei in the molecule. These terms,

called the potential energy curves can be represented graphically by plotting the energy as a function of R, the inter-nuclear separation.

Let $U_1(R)$ and $U_2(R)$ be the different potential energy curves and if they intersect at some point, then the functions U_1 and U_2 will have neighbouring values near the point. If R is such a separation where U_1 and U_2 have very close vlues E_1 and E_2, then it is possible by a small displacement R to make U_1 and U_2 equal. The energies E_1 and E_2 are the eigen values of the Hamiltonian H of the electron in the field of the nuclei which are fixed at a distance R from each other. For a small displacement δR, the Hamiltonian is

$$H + V = H + \frac{\partial H}{\partial R} \cdot \delta R \qquad 2.45$$

If φ_1 and φ_2 be the eigen functions of the operator H with the eigen energies E_1 and E_2, then the total wave-function is a linear combination of the two i.e:

$$\varphi = C_1\varphi_1 + C_2\varphi_2 \qquad 2.46$$

The Schrödinger equation for the perturbed system is

$$(H + V)\varphi = E\varphi \qquad 2.47$$

substituting 2.46 in 2.47 we get

$$C_1(E_1 + V - E)\varphi_1 + C_2(E_2 + V - E)\varphi_2 = 0 \qquad 2.48$$

Multiplying 2.48 on the left by φ_1^* and φ_2^* in turn and integrating,

$$C_1(E_1 + h_{11} - E) + C_2h_{12} = 0 \qquad 2.49$$

$$C_1h_{21} + C_2(E_2 + h_{22} - E) = 0 \qquad 2.50$$

where $h_{ik} = \int \phi_i^* V \phi_k \, d\tau$

Equations 2.49 and 2.50 give after simplification

$$E = \tfrac{1}{2}(E_1 + E_2 + h_{11}) \pm \sqrt{\tfrac{1}{4}(E_1 - E_2 + h_{11} - h_{22})^2 + h_{12}^2} \qquad 2.51$$

The curves will intersect each other (Figure 2.7a) if the expression under the radical in equation 2.51 vanishes i.e;

$$E_1 - E_2 + h_{11} - h_{22} = 0, \; h_{12} = 0 \qquad 2.52$$

The above two equations cannot generally be satisfied simultaneously. It may happen, however, that the matrix element h_{12} vanishes identically. This happens in all cases where the two terms are of different symmetry. Thus in this case, there remains only one equation which can be satisfied by suitable choice of R and then the potential energy curves will cross, but in general the intersection of the terms of like symmetry is impossible[29]. In such cases, the potential energy curves are found to move apart as shown in Figure 2.7b.

Thus the curve I_b has the character of an $A^+ + (B^+ + e)$ written $A_1 + B_1$ combination at small nuclear separation but the character of an $(A^+ + e) + B^+$ $A_2 + B_2$ combination at large separations. This situation is reversed for the curve II_b. Such pseudo-crossings are common in the systems in which both the collision products or both the reactants are

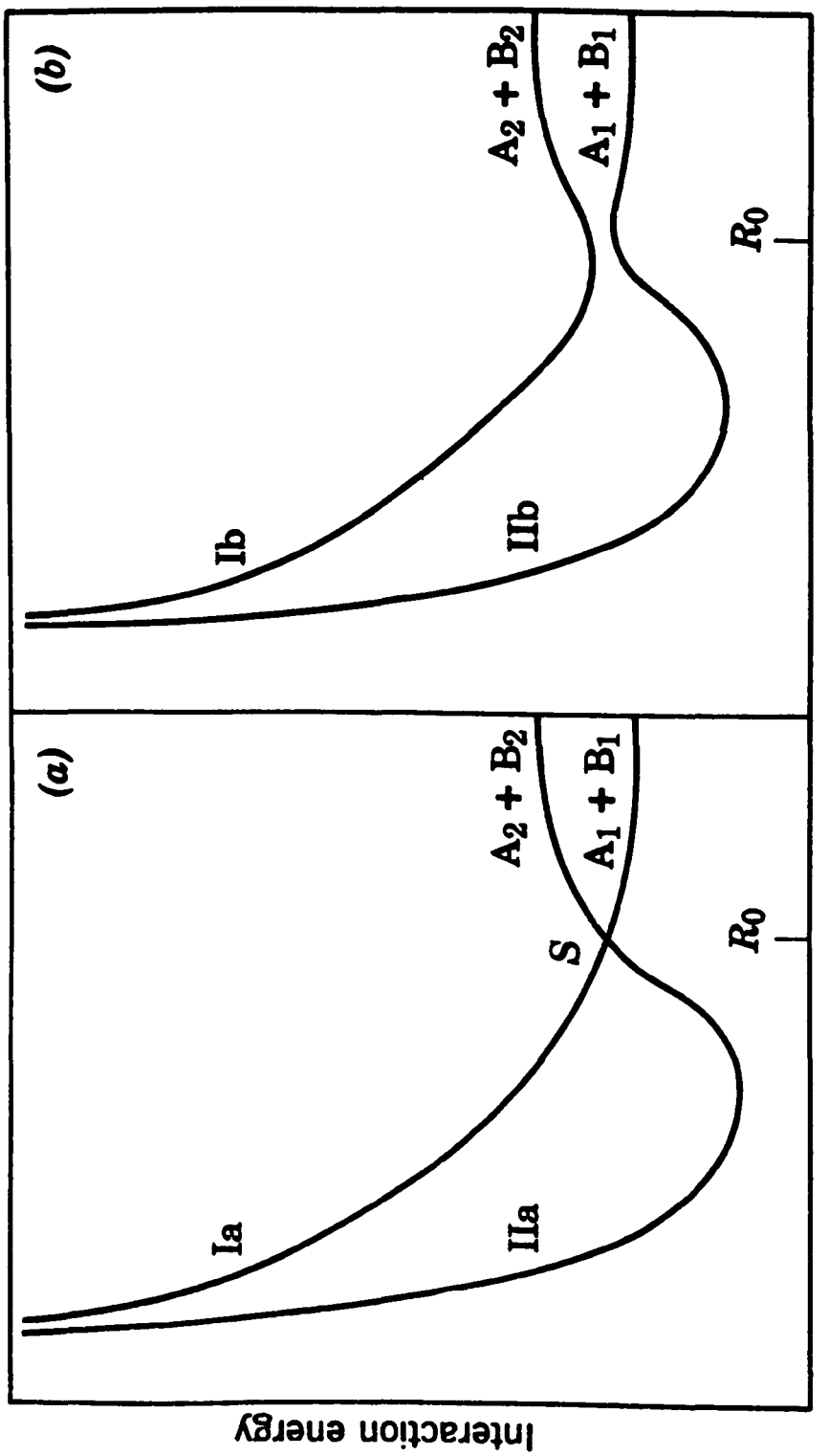
(a)
(b)
Ia
IIa
Ib
IIb
S
$A_2 + B_2$
$A_1 + B_1$
R_0
Interaction energy
Nuclear separation (R)

FIG. 2.7

charged, as is the case for the partial charge transfer

$$A^{+n} + B \longrightarrow A^{+(n-1)} + B^{+} + \Delta E$$

and the mutual neutralization process

$$A^{+} + B^{-} \longrightarrow A + B + \Delta E$$

In such cases, one state has a strong Coulomb interaction and the other a weak polarization interaction. Neglecting the latter, it is possible in such systems to find the curve crossing point R_x from the relation[30]

$$R_x = \frac{(n-1)\, e^2}{\Delta E} = \frac{27.2\ (n-1)}{\Delta E} \quad \text{a.u.} \qquad 2.53$$

where ΔE is the energy defect in volts and n is the charge in atomic units on the projectile A before the collision.

2.5.2 Landau Zener formula

The exact electronic eigenfunction $\psi_m(r/R)$ and $\psi_n(r/R)$ of the quasi-molecule for fixed nuclei are functions of the electronic coordinate r and depend on R, the internuclear separation as a parameter while $E_m(R)$ and $E_n(R)$ belonging to them depend only on R as a parameter. If the eigenfunctions interchange their characters as R changes from $R > R_x$ to $R < R_{x1}$ there is a pseudo-crossing of the potential energies, in which case the exact eigenfunctions can be expressed as a linear orthogonal combination of the functions $\phi_n(r/R)$ and $\phi_m(r/R)$. In the case of the electron transfer from the state n of the atomic system A to the state m of the atomic system B

$$(A + e)_n + B \longrightarrow A + (B + e)_m \qquad 2.54$$

$\phi_n(r/R)$ represents the left hand side for all R and $\phi_m(r/R)$ represents the right hand side for all R. If the relative nuclear velocity is constant, $Z = \underline{R}\cdot\underline{v} = vt$, then the perturbation calculation gives the equation for the amplitudes $C_m(z)$ and $C_n(z)$ associated with the states $\phi_m(r/R)$ and $\phi_n(r/R)$. The result is two coupled equations[31]

$$i\hbar v \frac{\partial C_n(Z)}{\partial Z} = h_{nm}(R)\, C_m(Z) \exp\left\{ - \frac{i}{\hbar v} \int^Z \left(h_{mm}(R) - h_{nn}(R) \right) dZ \right\} \qquad 2.55$$

and

$$i\hbar v \frac{C_m(Z)}{Z} = h_{mn}(R)\, C_n(Z) \exp\left\{ \frac{i}{\hbar v} \int^Z \left[(h_{mm}(R) - h_{nn}(R) \right] dZ \right. \qquad 2.56$$

where

$$h_{pq} = \int \phi_p^{*}\, (r/R)\, H\, \phi_q\, (r/R)\, dr$$

The crossing distance is defined by

$$h_{mm}(R_c) = h_{nn}(R_c)$$

Eliminating $C_m(Z)$ in 2.55 and 2.56 gives

$$\frac{\partial^2 C_n(Z)}{\partial Z^2} + \left[- \frac{1}{h_{nm}} \frac{\partial h_{nm}}{\partial Z} + \frac{i}{\hbar v} (h_{mm} - h_{nn}) \right] \frac{\partial C_n(Z)}{\partial Z} + \left(\frac{h_{nm}}{\hbar v} \right)^2 C_n(Z) = 0 \qquad 2.57$$

In the Landau[32]-Zener[33] theory it is assumed that the transitions can only occur in a very narrow zone around the crossing point, so that

$$h_{nn}(Z) - h_{mn}(Z) = \alpha(Z - Z_c); \qquad 2.58$$

$$\alpha = \text{constant}$$

$$h_{nm}(Z) = h_{mn}(Z) = \beta = \text{constant} \qquad 2.59$$

These assumptions lead to an exact solution of 2.55 and 2.56 and are justified if most of the transitions take place near the crossing point so that the values of the matrix elements are unimportant elsewhere. The boundary conditions are

$$C_n(-\infty) = 1 \quad \text{and} \quad C_m(-\infty) = 0$$

The transition probability

$P = \left| C_m(+\infty) \right|^2$ is then the solution of 2.57 subject to the conditions of 2.58 and 2.59. The Landau-Zener formula is then given by

$$P = \exp -\left[\frac{2}{h\nu} \left[\frac{\Delta U(R_x)^2}{\left| \frac{d}{dR}(U_i - U_f) \right|_{R=R_x}} \right] \right] \qquad 2.60$$

where $\Delta U(R_x)$ is the energy difference between the two potential energy curves at $R = R_x$ and

$$U_i = \int \phi_i^* \, V \, \phi_i \, d \quad , \quad U_f = \int \phi_f^* \, V \, \phi_f \, d$$

V(R) being the appropriate interaction energy.

If the atoms A and B in states A_1 and B_1 respectively are allowed to come together infinitely slowly, the interaction between them will follow curve II_b and no transfer will take place. However if the atoms approach with a finite relative velocity v, there is a finite probability that a transition will occur in which the system will jump from II_b to I_b. This is the probability P given by 2.60. The probability that the system will continue along II_b is (1 - P). When the atoms reach their

distance of closest approach, their relative motion will reverse and there is again a chance P, that a transition will occur. Thus if the atoms are brought together and then allowed to separate again, the total probability of transition is

$$\rho = 2P(1 - P) \qquad 2.61$$

2.5.3 Charge Transfer cross-section from Landau-Zener formula.

The probability P depends upon the relative angular momentum $\sqrt{\ell(\ell + 1)}\ h$, of the colliding system and the charge transfer cross-section is

$$\sigma = \frac{\pi}{K^2} \sum (2\ell + 1)\ 2P(1-P) \qquad 2.62$$

where $K = \frac{8\pi\mu E}{h^2}$, E being the initial kinetic energy of relative motion and μ the reduced mass. Replacing the summation sign by integration in 2.62 and making use of 2.60, Bates and Moiseiwitsch[34] obtain

$$\sigma = 4\pi\ R_x^{\ 2}\ f\ I(\eta) \qquad 2.63$$

with

$$I(\eta) = \int_0^{\infty} \exp(-\eta x) \left[1 - \exp(-\eta x)\right] x^{-3}\, dx \qquad 2.64$$

where

$$\eta = 247\ (n-1)\ \mu^{\frac{1}{2}} \left[\frac{\Delta U(R_x)}{\Delta E}\right]^2 E^{-\frac{1}{2}}\ (1+\lambda)^{-\frac{1}{2}}(1+\mu)^{-1} \qquad 2.65$$

$$\lambda = U_i(\infty) - U_i(R_x) \qquad 2.66$$

$$\mu = \left[\frac{e^4}{R_x^5}\ (\Delta E)^2\right] \left(n^2\ \alpha_A - (n-1)^2\ \alpha_{A+} - \alpha_{B^+}\right) \qquad 2.67$$

where f is the probability that the particles approach along the particular potential energy curves and the α's the corresponding polarizabilities. Integral $I(\eta)$ has a maximum value of 0.113[35] when $\eta = 0.424$, which implies that the cross-section function should behave likewise. Using experimentally determined maxima, it is thus possible to calculate the cross-sections at other energies. Bates and Moiseiwitsch also calculate the energy separation

$$\left| \Delta U(R_x) \right| = 2 \left| S(\rho - p_f) - \xi/(1-S^2) \right|_{R = R_x} \qquad 2.68$$

when

$$S = \int \phi(r_A/n_A)\ \phi(r_{B^+}/n_{B^+})\ d\tau \qquad 2.69$$

$$\rho = \int \phi\ (r_{B^+}/n_{B^+})^2\ r_A^{-1}\ d\tau \qquad 2.70$$

$$\xi = \int \phi(r_A/n_A)\ \phi(r_{B^+}/n_{B^+})\ r_A^{-1}\ d\tau \qquad 2.71$$

$$p_f = e^2 \left\{ (m-1)^2\ \alpha_{A^+} + \alpha_B(m-1) + \right\} / 2R_x^4 \qquad 2.72$$

in which ϕ represents the initial and final wave functions of the active electron, r the position vectors and m the principal quantum number. Hasted, Lee and Hussain[36] using an asumptotic wave function of the type

$$\phi = N_n\ r^{(m^*-1)}\ \exp\ -\left\{ (2\ E_i)^{\frac{1}{2}}\ r \right\}$$

in which m* is the effective quantum number, N_n the normalising factor, E_i the ionization energy in a.u. have computed $\Delta U(R_x)$ for the partial

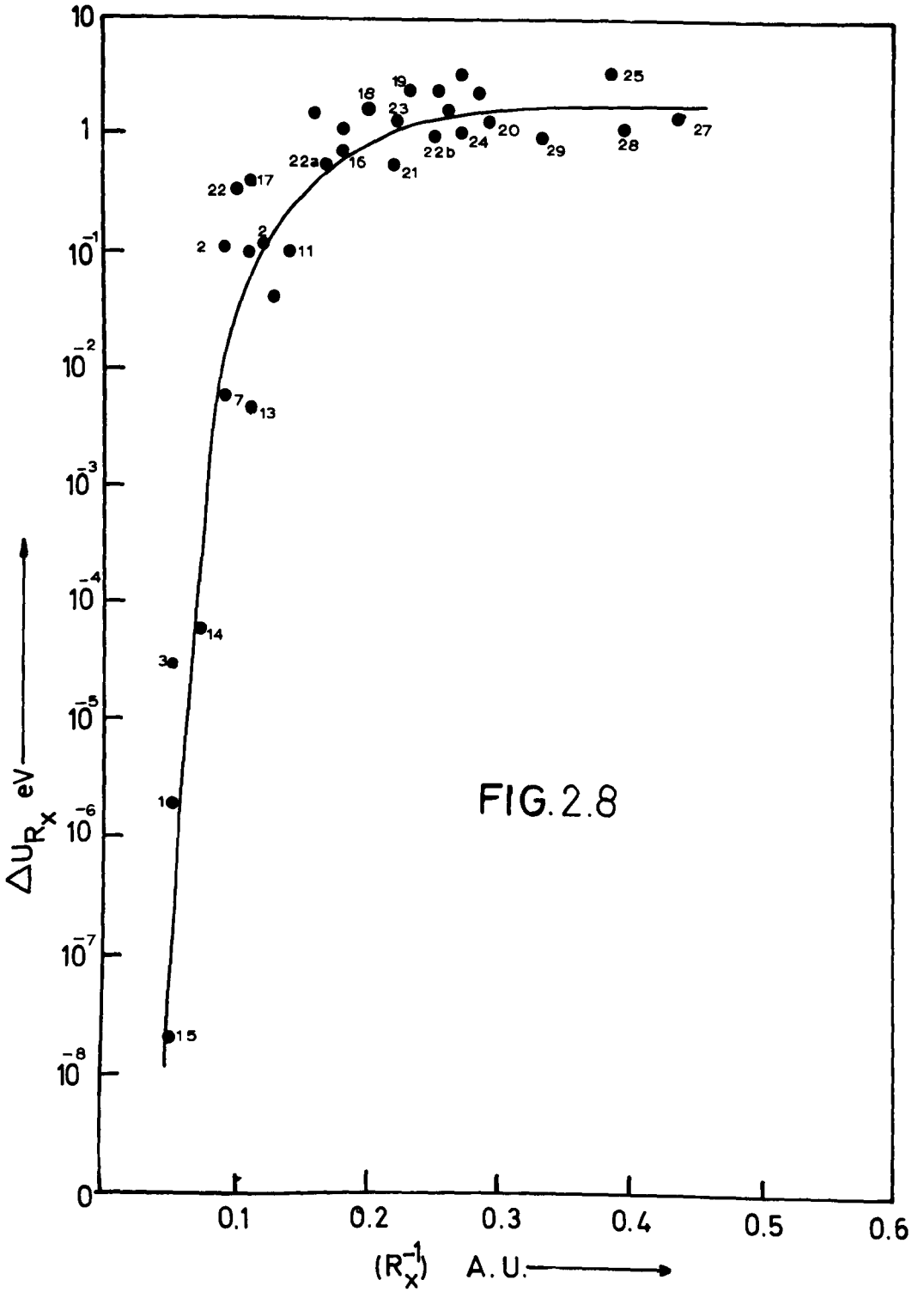
10
1
10^{-1}
10^{-2}
10^{-3}
10^{-4}
10^{-5}
10^{-6}
10^{-7}
10^{-8}
0
ΔU_{R_X} eV
0.1
0.2
0.3
0.4
0.5
0.6
(R_X^{-1}) A.U.
1
2
3
7
10
11
13
14
15
16
17
18
19
20
21
22
22a
22b
23
24
25
27
28
29

FIG. 2.8

charge transfer process for a number of projectile and target atoms. They have plotted all the available data on $\Delta U(R_x)$ as log (ΔU_{R_x}) against R_x^{-1} and have shown that $\Delta U(R_x)$ is dependent on R_x. The values of $\Delta U(R_x)$ estimated from the measurements of Hasted and Hussain[37], Hasted and Smith , Hasted and Chong[38] and the theoretical calculations of Dalgarno[39], Bates and Moiseiwitsch[40], Boyd and Moiseiwitsch[41] provide a means of determining empirically the dependence of $\Delta U(R_x)$ on R_x, the internuclear separation at the crossing point. Figure 2.8 shows such a curve in which the key to numbers is shown in Table 1.

This curve enables the Landau-Zener formula to predict the cross-sections of the processes proceeding by way of transitions at the pseudo-crossing of the potential energy curves. For a given process, ΔE the energy defect may be calculated from the ionization potentials; R_x may be calculated from equation 2.53 and $\Delta U(R_x)$ corresponding to R_x may then be deduced from Figure 2.8. With $\Delta U(R_x)$ thus determined, equation 2.63 may be used to predict the energy of the maximum cross-section to within 60% and the maximum cross-section may also be calculated.

2.5.4 Limitations of the Landau-Zener formula and recent calculations based on the impact parameter treatment.

Although the Landau-Zener formula discussed in the preceding sections, is valuable in providing a qualitative explanation of the occasional failure of Massey's adiabatic criterion, Bates[44] has argued that this formula is in general not applicable for quantitative calculations. The most criticized assumption, that the transitions can only take place at

TABLE 1

	Reaction (Quantum calculations)	
1.	Li^{2+} H (Li^{+} ^1S)	
2.	Li^{2+} H (Li^{+} ^3S)	
3.	B^{2+} H (B^{+} ^1P)	Dalgarno.
4.	A^{3+} H	
5.	A^{3+} H (A^{2+} ^2P)	
6.	Be^{2+} H	
7.	Mg^{2+} H	Bates and Moiseiwitsch.
8.	Si^{2+} H	
9.	H^- Li^+ (Li ^2S)	Bates and Boyd.
10.	Be^{3+} He (Be^{2+} 2^3S)	
11.	Be^{3+} He (Be^{2+} 2^3P)	
12.	Li^{3+} He (Li^{2+}, 2s or 2p)	
13.	Be^{3+} He (Be^{2+} 2^1P)	Boyd and Moiseiwitsch.
14.	A^{3+} He (A^{2+} $3s$ ^2S)	
15.	Mg^{3+} He (Mg^{2+} $3s$ ^3P)	
	Experimental	
16.	Ne^{2+} He	Hasted and Smith.
17.	A^{2+} + He	" " "
18.	Kr^{3+} He	Hasted and Chong.
19.	Kr^{4+} He	
20.	N^{2+} Ne	
21.	A^{2+} Ne	Hasted and Smith.
22.	Kr^{2+} Ne	
23.	Kr^{3+} Ne	
23a.	Kr^{3+} Ne (Kr^{2+} ^1S)	
23b.	Kr^{3+} Ne (Kr^{2+} ^1P)	
24.	Kr^{4+} Ne	
24a.	Kr^{4+} Ne (Kr^{3+} 4P)	
25.	Kr^{4+} Ne (40/31)	Hasted and Hussain.
26.	Kr^{4+} Ne (40/22)	
27.	Ar^{2+} + Ar	
28.	Kr^{2+} + Kr	
29.	Xe^{2+} + Xe	

or near the crossing point, severely limits its range of validity. In fact the limits within which it is valid are seldom found in actual practice. Contrary to the Landau-Zener assumptions, the refinements proposed by Bates show that the range of inter-nuclear separation over which transitions are likely is given by

$$\Delta R = \frac{4\pi v h\ (R-R_x)}{h_{nn} - h_{mm}} \qquad 2.73$$

$$\approx 0.5 \left| \Delta U(R_x) \right| R_x^{\,2} \qquad 2.74$$

where R_x is the crossing point. If the interaction is strong this width may be so large that the failure to take account of the variation of the interaction energies with nuclear separation leads to serious error in the calculation of the transition probabilities. Therefore for an exact solution of the coupled equations 2.55 and 2.56 it is necessary to integrate over the entire range of $Z = vt$. The probability is then given by

$$P = 2 \left| \frac{1}{i\hbar v} \int_{-\infty}^{+\infty} h_{nm} \exp\left\{ - \frac{i}{\hbar v} \int_{0}^{Z} (h_{nn} - h_{mm})\, dZ \right\} dZ \right|^2 \qquad 2.75$$

the solution of which in some cases results in a second maximum in the cross-section function, not predicted by the over simplified Landau-Zener theory. The second maximum in the cross-section function has not so far been observed experimentally. In the event of the failure of the equation 2.75, it becomes imperative to solve the coupled equations numerically which has been attempted by Bates et al[28] along the following lines.

Treating the nuclei A and B as classical particles with constant relative velocity $\underline{v}$, they obtain the coupled equations similar to the equations 2.33 and 2.34 for the asymmetric charge transfer process 2.2 (relating the coefficients C_p and C_q). These equations are

$$\frac{ivdC_p(Z)}{dt} = C_q(Z)\,\bar{K}(R)\,\exp\left\{i\,\frac{I(Z)}{v}\right\} \qquad 2.76$$

and

$$\frac{ivdC_q(Z)}{dZ} = C_q(Z)\,\bar{K}(R)\,\exp\left\{-\,i\,\frac{I(Z)}{v}\right\} \qquad 2.77$$

where

$$\bar{K}(R) = \frac{K_1(R) + K_2(R)}{2}$$

$$K_1(R) = \frac{h_{pq} - S\,h_{qq}}{1 - S^2}\,, \quad K_2(R) = \frac{h_{qp} - S\,h_{pp}}{1 - S^2}$$

$$I(R) = \int_{Z_o}^{Z} g(R)\,dZ$$

$$g(R) = E_p - E_q + \frac{h_{pp} - h_{qq} + S(h_{pq} - h_{qp})}{1 - S^2}$$

$$h_{pq} = \int \phi_p\, V^A\, \phi_q\, d\tau\,, \quad h_{qp} = \int \phi_q\, V^B\, \phi_p\, d\tau$$

$$h_{pp} = \int \phi_p\, V^B\, \phi_p\, d\tau\,, \quad h_{qq} = \int \phi_q\, V^A\, \phi_q\, d\tau$$

$$S = \int \phi_p\, \phi_q\, d\tau$$

E_p and E_q being the eigen values of the eigen-functions ϕ_p, ϕ_q

respectively, and V^A and V^B the corresponding potentials. The boundary conditions are

$$C_p(-\infty) = 1, \quad C_q(-\infty) = 0$$

and the probability that the collision results in a transition of the electron from state p around B to state q around A is

$$P = \left| C_q(+\infty) \right|^2$$

They express P in terms of the solutions at the origin and the coefficients in polar form,

$$P = 4\, r_p^2(0) \left\{ 1 - r_p^2(0) \right\} \sin^2 \eta(0) \qquad 2.78$$

where $r_p(Z)$ and $\eta(Z)$ are the solutions of the purely real equations

$$v \frac{dr_p(Z)}{dZ} = \left\{ 1 - r_p^2(Z) \right\}^{\frac{1}{2}} \bar{K}(R) \sin \eta(Z) \qquad 2.79$$

and

$$v \frac{d\eta(Z)}{dZ} = -g(R) + \left[\frac{2r_p^2(Z) - 1}{r_p(Z) \left\{ 1 - r_p^2(Z) \right\}^{\frac{1}{2}}} \right] \bar{K}(R) \cos \eta(Z) \qquad 2.80$$

which are obtained from 2.76 and 2.77. The boundary conditions for these equations are

$$r_p(-\infty) = 1, \qquad \eta(-\infty) = 0$$

The transition probability P as a function of the impact parameter obtained from equation 2.78 by the numerical solution of the equations 2.79, 2.80 for the process

$$Be^{2+} + H \longrightarrow Be^{+} + H^{+} + 4.61, \quad R_x = 5.81\, a_o \qquad 2.81$$

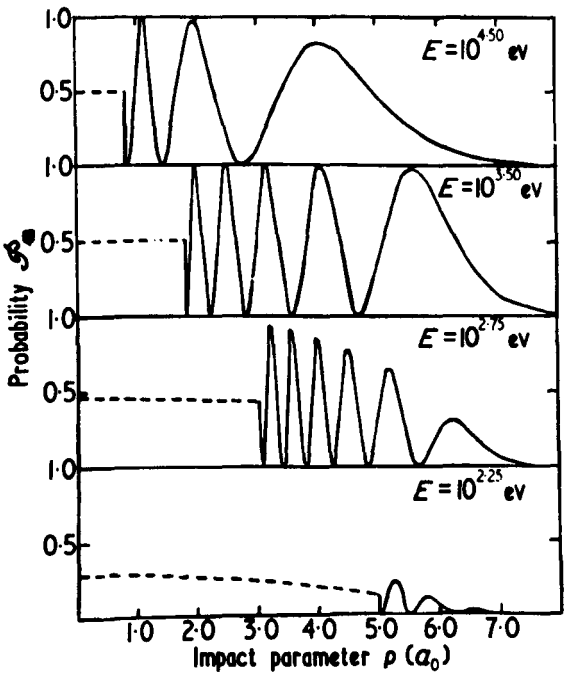

FIG. 2.9

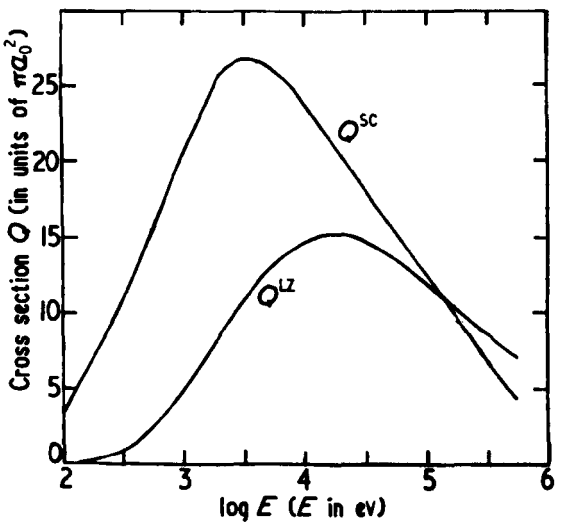

FIG. 2.10

is shown in Figure 2.9. It is seen that P is a rapidly oscillating function of ρ, the impact parameter. The derived cross-section is shown in Figure 2.10 where it is observed that the maximum of the cross-section σ_{sc} obtained from the solution of the coupled equations is almost twice that of the maximum of the cross-section σ_{iz} obtained from the Landau-Zener approximation. Two other features are also apparent, namely, the cross-section maxima do not coincide and at lower energies $\sigma_{sc} \gg \sigma_{iz}$.

The advantage of the numerical solution is that it enables one to compare the experimentally and theoretically derived transition probabilities as a function of the impact parameter. The laboratory measurements of the angular distribution of A^{++} and A^{+}, when A^{++} traverses the target atoms in the collision chamber under single collision conditions, may be converted into the transition probabilities as a function of the impact parameter, provided the angular deflection may be related to the impact parameter. The difficulty arises in the choice of an interacting system for which the theoretical calculations are readily available and for which the measurements in the laboratory may be carried out with relative ease. For example, the theoretical calculations are only available for the reaction

$$Be^{++} + H \longrightarrow Be^{+} + H^{+} + 4.61 \text{ eV}$$

for which laboratory measurements are tricky, because they require an ion source capable of producing doubly charged metal ions and an oven type source to produce atomic hydrogen for the collision chamber. If for experimental simplicity other systems are to be chosen, then it must

also be bourne in mind that these calculations are only applicable to s - s transitions. This of course limits the choice of systems for experimental study. Two such systems for which the angular measurements can be carried out in the laboratory are

$$O^{++} + Ne \longrightarrow O^{+} + Ne^{+} + 13.55 \text{ eV} \quad R_x = 2.00\ a_o \qquad 2.82$$

and

$$O^{++} + Ne \longrightarrow O^{+} + He^{+} + 10.528 \quad R_x = 2.583\ a_o \qquad 2.83$$

Experimental investigations of the angular distributions of O^{++} and O^{+} for the above reactions were carried out at two energies 1200 eV and 2600 eV. The experimental set up will be discussed in the third chapter while the fourth chapter will be concerned with the data and the method of reduction to a form suitable for comparison with the theory.

CHAPTER III

EXPERIMENTAL STUDY OF CHARGE TRANSFER

3.1 INTRODUCTION

An ideal charge transfer experiment has the following requirements i) an ion source producing charged particles in a known state and narrow energy distribution. ii) a magnetic analyzer to obtain a monoenergetic beam of particular ions in a known charge state. iii) the analyzed ions must be accelerated or decelerated to the required impact energy and then permitted to pass through a gas target at known pressure. There are then three signals available for study after the collision, namely

a, Fast atom signal
b, Fast ion signal
c, Slow ion signal

and to obtain complete information of the collision process each of the above signals must be subjected to mass , energy and charge state analysis. Moreover study of the angular distribution of the fast and slow signals furnishes information on the dependence of the transition probability on the impact parameter of the colliding system. Further, for the measurement of the absolute cross-sections the efficiency of the detection system must be known. All these measurements cannot be carried out in a single experiment and most experimentalists have either analyzed the

post collision primary beam or measured and analyzed the slow collision products when the projectile beam traverses the collision chamber. These primary or secondary analysis techniques however provide enough data for the determination of the cross-sections for the inelastic heavy particle collisions. Various experimental methods have been reviewed by Massey and Burhop[43], Allison[44], Allison and Garcia Munoz[45] and Hasted[46].

The following sections will be concerned with a discussion of the various experimental techniques together with a description of different experimental arrangements.

3.2 Thick and Thin Targets

Experimental determination of the collision cross-sections can be divided into two classes, namely, "thick" and "thin" target techniques. The former class of experiments consist of either determining the equilibrium charge state composition of a beam of projectiles when passed through a gas target thick enough to ensure an equilibrium between the production and loss reactions of each of the possible charge state components, or determining the attenuation of a beam of projectiles in a gas filled collision chamber across which is applied a transverse electric or magnetic field. These fields sweep aside the slow ions, produced by the charge changing collisions with the target gas as soon as they are formed. This transverse field method is therefore suitable for studying the electron capture or loss processes by beams of neutral projectiles. In the thin target technique also called the "single collision technique", the pressure of the target gas is such that the mean free path of the projectile is

comparable to the dimensions of the collision chamber so that chances of multiple collisions are negligible.

3.3 The Total Charge Collection Method.

The passage of the fast ion beam through the gas in the collision chamber produces slow ions due to electron capture and ionization processes. The two processes can be separated because of the fact that the ionization produces an electron-ion pair. The collection of all these slow ions and electrons without any discrimination of the charge state of the slow ions is the basis of the total charge collection method of the cross-section measurements. If single collision technique is employed and if I_c is the slow ion current detected, σ_T, the total collision cross-section producing the slow charged particles, p the pressure and ℓ the collision path length, then

$$I_c = I_o \sigma_T \ell p \qquad 3.1$$

where I_o is the fast projectile ion beam current passing through the collision chamber. The single collision conditions can be verified by studying the collected current I_c as function of the target pressure. As shown by equation 3.1 the variation of I_c with p should be linear. Addition of the electron and the slow ion current ensures that the current I_c has no component due to the ionization process. Separation of the electron and ion current is effected by means of weak electric and or magnetic fields applied across a pair of parallel plates sometimes called "Condenser Plates". These fields do not appreciably affect the fast

primary ion beams but should be strong enough to make the path of the slow ions transverse to the primary beam, and to achieve "saturation conditions". The transverse path of the slow ions towards the collector and the saturation conditions ensure that i) all the slow ions are being collected, ii) the path length of the collision region is accurately known.

Experiments utilising a uniform electric field applied across the collision chamber have been performed by, amongst others Keene[47], Gilbody and Hasted[48], Donahoe and Hushfar[49] with uniform electric and magnetic fields parallel and transverse to the ion beam by Wolf[50] and Hasted[51], An alternative method to using "static" gas in the collision chamber is to let the ion beam pass through a neutral beam referred to as "the crossed beam technique". A modulated atomic beam from a furnace is crossed with a fast ion beam and slow ions produced are collected by a total ion collector or analysed by the mass spectrometric detector. The modulation is interposed in order to distinguish between charge transfer with beam particles as opposed to charge transfer with the background gas in the vacuum chamber. The A.C. beam signals so produced can be separated electronically from the D.C. background gas signals. This technique has been applied by Fite et al[52] in an experimental arrangement shown in Figure 3.1. The ions produced in an electron bombardment source are extracted and focussed before they enter the analysing magnetic field. The ions receive their final energy when they enter the main experimental chamber. The area carrying the ion source and the analyser is insulated from the experimental chamber by a Teflon flange. Three electrostatic

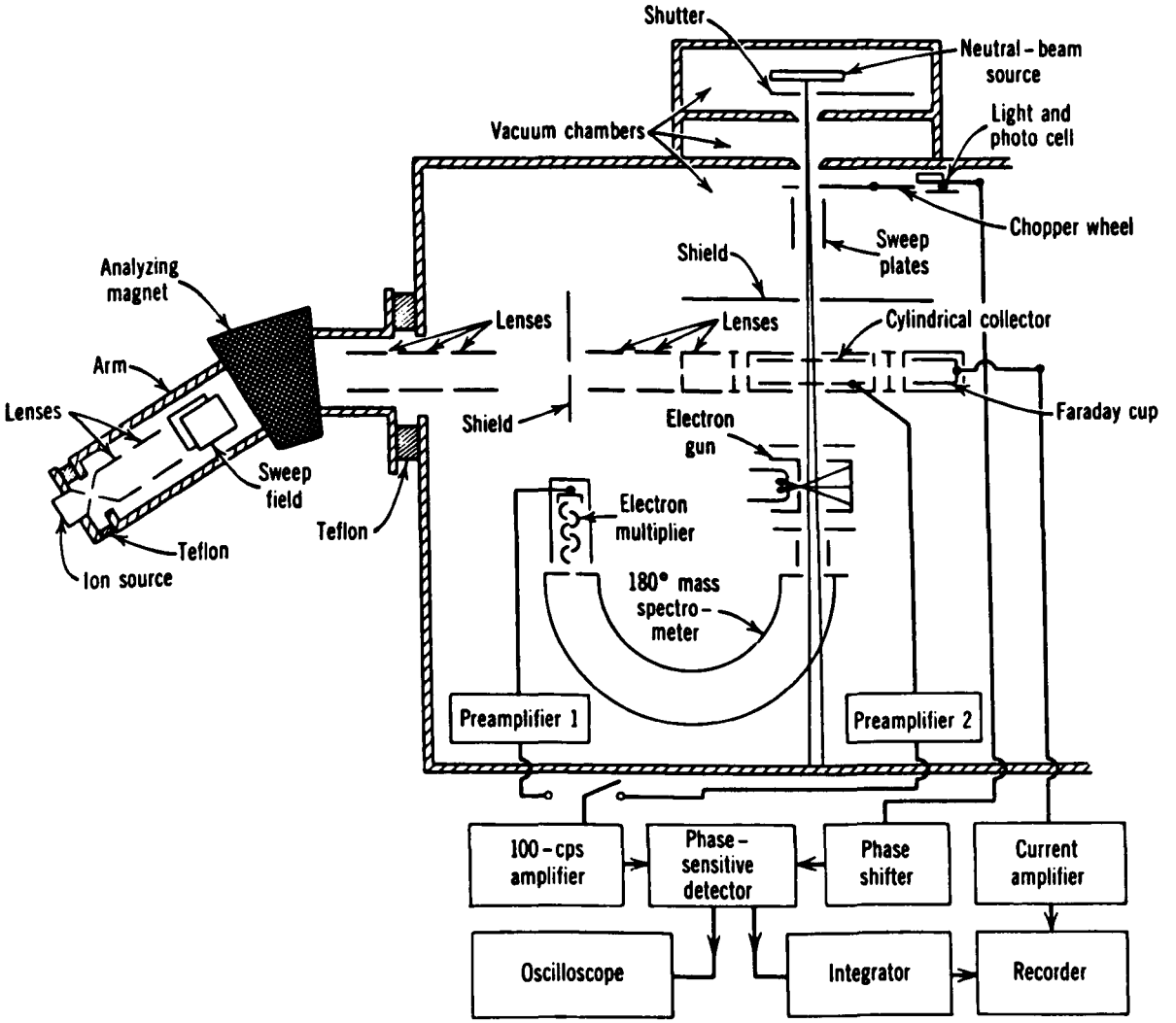
Shutter
Neutral-beam source
Vacuum chambers
Light and photo cell
Chopper wheel
Sweep plates
Shield
Analyzing magnet
Lenses
Lenses
Cylindrical collector
Arm
Lenses
Shield
Faraday cup
Electron gun
Sweep field
Teflon
Teflon
Electron multiplier
Ion source
180° mass spectro-meter
Preamplifier 1
Preamplifier 2
100-cps amplifier
Phase-sensitive detector
Phase shifter
Current amplifier
Oscilloscope
Integrator
Recorder

FIG. 3.1

lenses are provided to keep the ion beam focussed. The ions then pass through a narrow collimating slit which intercepts unwanted ions of adjacent masses. After passing through another set of cylindrical lens and collimating slit systems, the ion beam enters the interaction region. The ion and the neutral beams are made to intersect at the centre of a cylindrical collector whose axis coincides with the axis of the primary ion beam, the potential of which is maintained negative with respect to the surrounding electrode and slow charge transfer ions are then collected on the surface of this cylinder. The primary ions pass through a further defining slit and are collected in a Faraday cup. The apertures in the collision region are such that all those ions which pass through this slit necessarily pass through the neutral beam. The neutral beam is produced in a tungsten furnace and is modulated at 100 cps by a mechanically driven, toothed chopper wheel, any ions present in the beam are removed by the deflector plates. The beam is then passed through two apertures positioned diametrically opposite in the cylindrical collector. These apertures are covered with a 90% optically transparent grid to prevent field penetration. A mass spectrometer is used with an electron gun to determine the degree of dissociation of the neutral beam by observing the reduction in the signal of the molecular ions as the furnace is heated. The dissociation fraction D is given by[53]

$$D = {}^{1}/\left(1 + \sqrt{2}\ \frac{Q_1^{\,i}\ S_2^{\,i}}{Q_2^{\,i}\ S_1^{\,i}}\right) \qquad 3.2$$

where $S_1^{\,i}$ and $S_2^{\,i}$ are atomic and molecular peak strengths on the mass

spectrometer and $Q_1^i/Q_2 i$ is the ratio of the cross-sections for ionization of the atomic and molecular species. $Q_1^i/Q_2 i$ was determined in a similar set-up with the exception that the ion beam was substituted by an electron beam. If S_1 is the charge transfer signal due to the atoms in the neutral beam, $\frac{Q_2}{Q_1}$ the ratio of the molecular to the atomic signals and S the total signal due to the slow ions formed in the collision, then Fite et al find that

$$S = S_1 \left[1 + \frac{Q_2}{Q_1} \left(\frac{1 - D}{\sqrt{2}D} \right) \right] \qquad 3.3$$

Thus the measurements in this experiment yield both the atomic and molecular charge transfer cross-sections.

3.4 Secondary Analysis Method

The total charge collection method does not yield any information about the state of the target atom or molecule and an obvious extension of the investigation is to subject the secondary ions to mass analysis. Relatively slow secondary ions can be extracted by an electric field perpendicular to the main beam of sufficiently small intensity as not to distort the paths of the main beam unduly. The extracted slow ion beam can be accelerated and mass analysed into a spectrum of ions of different mass numbers. Provided the single collision conditions prevail, it is possible to measure the cross-section for the formation of ions of a given charge to mass ratio. In this analysis, however, the contributions of the positive ion ionization and stripping must be taken into account. The energies and angles at which slow ions are produced pose major problems in the efficient extraction of the secondary ions.

The exit slit must therefore be made sufficiently wide and the extraction potential sufficiently large to effect complete extraction. In which case the extraction field sets a lower limit to the primary ion energy at about 30 eV, below which excessive distortion of the primary beam would occur. Two conditions must then be satisfied, i) The extracted beam strength must be independent of the transverse collision chamber field. ii) The analysis peaks must be found to be "flat top", that is, independent of magnetic field over a certain range not only when the exit slit is widened abnormally but also with a narrow slit. Only then will the ion current be proportional to the number of ions entering the mass spectrometer.

Calibration of the instrument against total charge collection measurement is necessary in order to determine absolute cross-sections. The secondary analysis method has been employed by Fedorendo and Afrosimov[55,56] in the primary ion energy range 3 - 180 keV, by Lindholm[57] for the study of secondary ion formation in dissociation of molecular gases, by Hasted and Hussain[58] for the study of electron capture by multiply charged ions and by Morgan and Everhart[59], for the study of angular and energy distributions of recoiling target particles.

3.5 Primary Beam Analysis Method

Measurements of the cross-section have been carried out by studying the charge composition of the primary beam after it has passed through the gas in the collision chamber by using thick or thin target techniques.

3.5.1 Studies using thick target technique

Stier and Barnet[60] have measured the electron capture cross-sections

by the method of beam equilibrium or attenuation in a transverse electric field. As an A^+ ion beam enters the collision chamber filled with gas with number density n, electron capture occurs (cross-section σ_{10}) and the beam becomes a mixture of fast ions and neutrals. The neutrals are further subject to electron stripping (cross-section σ_{01}) so that if F_1 and F_0 are respectively the fraction of ions and neutrals, then

$$\frac{dF_1}{dx} = (\sigma_{01} F_0 - \sigma_{10} F_1) \qquad 3.4$$

and

$$F_1 + F_2 = 1 \qquad 3.5$$

If the pressure now is sufficiently increased, $\frac{dF_1}{dx}$ approaches zero and the beam achieves equilibrium between the charged and neutral components. Under these conditions, from 3.4 and 3.5

$$F_{1\infty} = \frac{\sigma_{01}}{\sigma_{01} + \sigma_{10}} \qquad 3.6$$

$$F_{0\infty} = \frac{\sigma_{10}}{\sigma_{01}+\sigma_{10}} \qquad 3.7$$

$$F_{1\infty} + F_{0\infty} = 1 \qquad 3.8$$

Substituting F_0 and σ_{01} from 3.5 and 3.6 in 3.4 and integrating, remembering that when x = 0, F_1 = 1,

$$\sigma_{10} = \frac{1 - F_{1\infty}}{nx} \log_e \frac{1 - F_{1\infty}}{F_1 - F_{1\infty}} \qquad 3.9$$

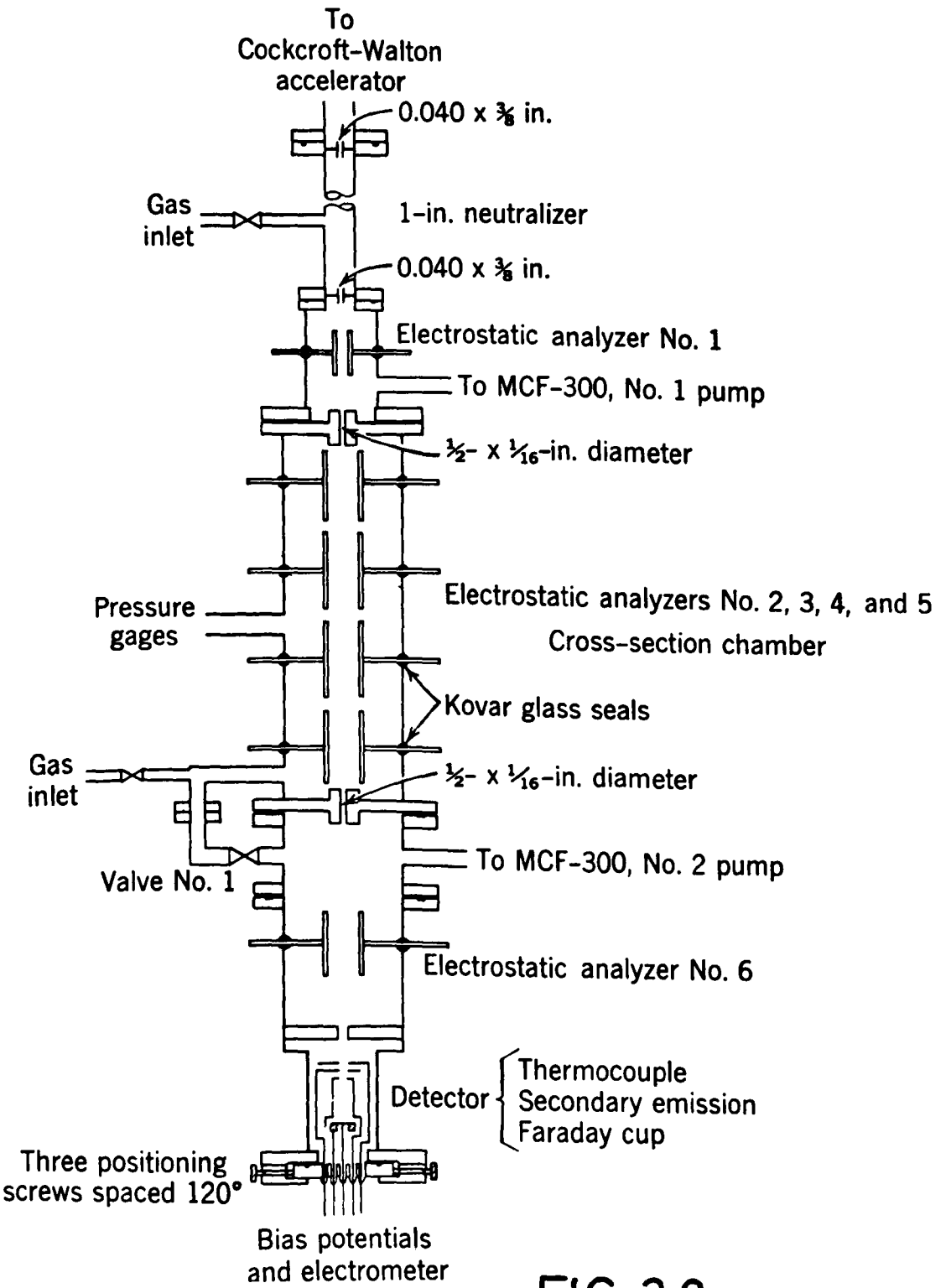
To
Cockcroft-Walton
accelerator
0.040 x ⅜ in.
Gas
inlet
1-in. neutralizer
0.040 x ⅜ in.
Electrostatic analyzer No. 1
To MCF-300, No. 1 pump
½- x 1/16-in. diameter
Pressure
gages
Electrostatic analyzers No. 2, 3, 4, and 5
Cross-section chamber
Kovar glass seals
Gas
inlet
½- x 1/16-in. diameter
To MCF-300, No. 2 pump
Valve No. 1
Electrostatic analyzer No. 6
Detector
Thermocouple
Secondary emission
Faraday cup
Three positioning
screws spaced 120°
Bias potentials
and electrometer

FIG. 3.2

$$\sigma_{01} = \frac{F_{1\infty}}{nx} \log_e \frac{1 - F_{1\infty}}{F_1 - F_{1\infty}} \qquad 3.10$$

It is only necessary to measure $F_{1\infty}$, the equilibrium fraction of A^+ and F_1, the fraction at a known pressure below the equilibrium pressure, in order that σ_{10} and σ_{01} can be calculated. If the beam passes through a collision chamber of length l containing a gas having ς atoms per molecule, at a pressure p dynes/cm^2, then

$$nx = \frac{N l \varsigma P}{RT} \qquad 3.11$$

where N is Avogacho's number, T the absolute temperature and R the gas constant. At this pressure F_1 is the fraction of singly charged ions. Relationships 3.9 and 3.10 are for a two component system but by analogous arguments formulae for more than two charged state components can also be written down.

A typical apparatus used by Stier and Barnet [60, 61, 62] is shown in Figure 3.2. A beam of ions from an accelerator enters at the top of the apparatus. The beam could be neutralized by the electron capture process with the remaining charged species swept aside by the electrostatic analyzer No. 1. The neutral beam then entered the collision chamber and the tube could be used through analyzer 6 to measure charge fractions in an equilibriated beam. The apparatus was also used to measure the attenuation of the fast neutrals to determine electron loss cross-section σ_{01} and negative ion formation cross-section σ_{0-1}. Complications may arise however since the neutral beam obtained in these experiments by electron capture invariably contain[63] metastables whose abundance varies

with the pressure of the gas used for the production of the neutral beam.

3.5.2 Primary Beam Studies using thin target technique.

For the quantitative study of all the collision products in a primary ion beam it is necessary to work under single collision conditions and to use electrostatic or magnetic analysis to separate the neutrals and different charge state components. However the errors that might arise due to elastic scattering and from pressure variations outside the collision chamber must be fully investigated. Since the neutral particle detectors usually employ secondary effects, the calibration of the detector is necessary.

Figure 3.3 shows Flaks and Solov'ev's[64] arrangement for the study of the charge transfer of singly and doubly charged ions. Such ions of inert gases were produced in an arc source placed in a magnetic field transverse to the ion beam and were analyzed in the 90^{o} sector type magnetic analyzer M_1. The ion beam was collimated by circulat diaphragms D_2 and D_3, passed into the collision chamber and emerged from it through the diaphragm D_4. The condensers K_1 and K_2, the diaphragms D_5 and D_7 and the bellows B_1 and B_2 were used to adjust the beam. The guard electrode K_3 served to collect the secondaries scattered at the edges of D_3. The primary beam in the collision chamber was monitored by the Faraday cup formed by the condenser K_4 and lid L. When the lid was removed upwards the electrodes K_3 and K_4 were grounded and the ion beam could pass into the magnetic analyzer, M_2 which was similar to M_1. The fast neutral

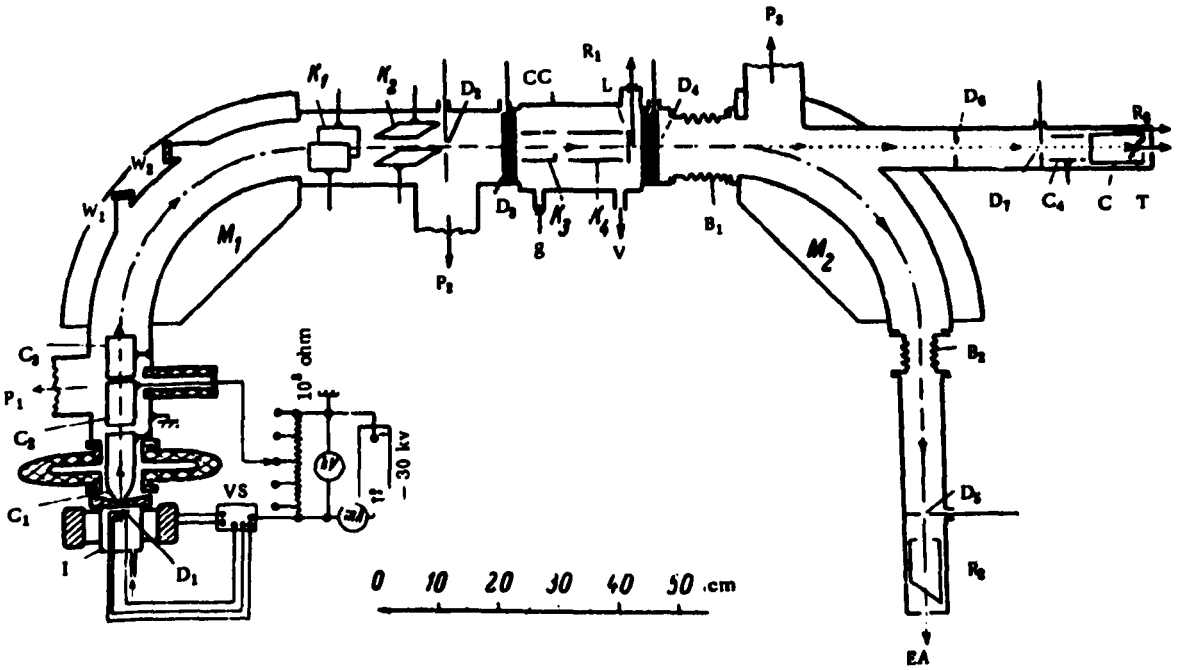
P3
R1
K1
K2
D2
CC
L
D4
D6
R6
W2
W1
M1
D3
K3
K4
B1
M2
D7
C4
C
T
P2
g
V
C3
P1
C2
10⁸ ohm
B2
VS
-30 kv
C1
D5
I
D1
R5
0 10 20 30 40 50 cm
EA

FIG.3.3

beam was recorded on R_3 by measuring the secondary electron current emitted by the target T and collected by C. The cross-sections were computed from the equations

$$\sigma_{10} = \frac{1}{3.3 \times 10^{16}} p\ell \left[\frac{i_3}{J_3 + i_3} \text{ gas} - \frac{i_3}{J_3} \text{ bkgd} \right] \qquad 3.12$$

$$\sigma_{20} = \frac{1}{3.3 \times 10^{16}} p\ell \left[\frac{i_3}{J3/_2 + i_3 + i_2} \text{ gas} \quad \frac{i_3}{J3/_2} \text{ bkgd} \right] \qquad 3.13$$

$$\sigma_{21} = \frac{1}{3.3 \times 10^{16}} p\ell \left[\frac{i_2}{J2/_2 + i_3 + i_2} \text{ gas} \quad \frac{i_2}{J2/_2} \text{ bkgd} \right] \qquad 3.14$$

where

J_2 and J_3 are the primary beam currents measured by R_2 and R_3 respectively. i_2 is the current of the fast singly charged ions appearing as a result of the capture $I^{2+} \longrightarrow I^{+}$ and measured by R_2. i_3 is the neutral current measured by R_3. ℓ is the length of the collision chamber = 23 cms. and p is the pressure in mmHg of the gas under investigation.

This method has also been used by Flaks and Filipenko[65] and by Fogel and co-workers[66,67,68] for capture processes.

3.5.3 Measurements of the Angular Distributions.

The total electron capture cross-sections derive their magnitude from the electron transferring from one atom to another when the atoms are substantially separated in distance involving many values of impact parameters between the colliding particles that contribute to the total

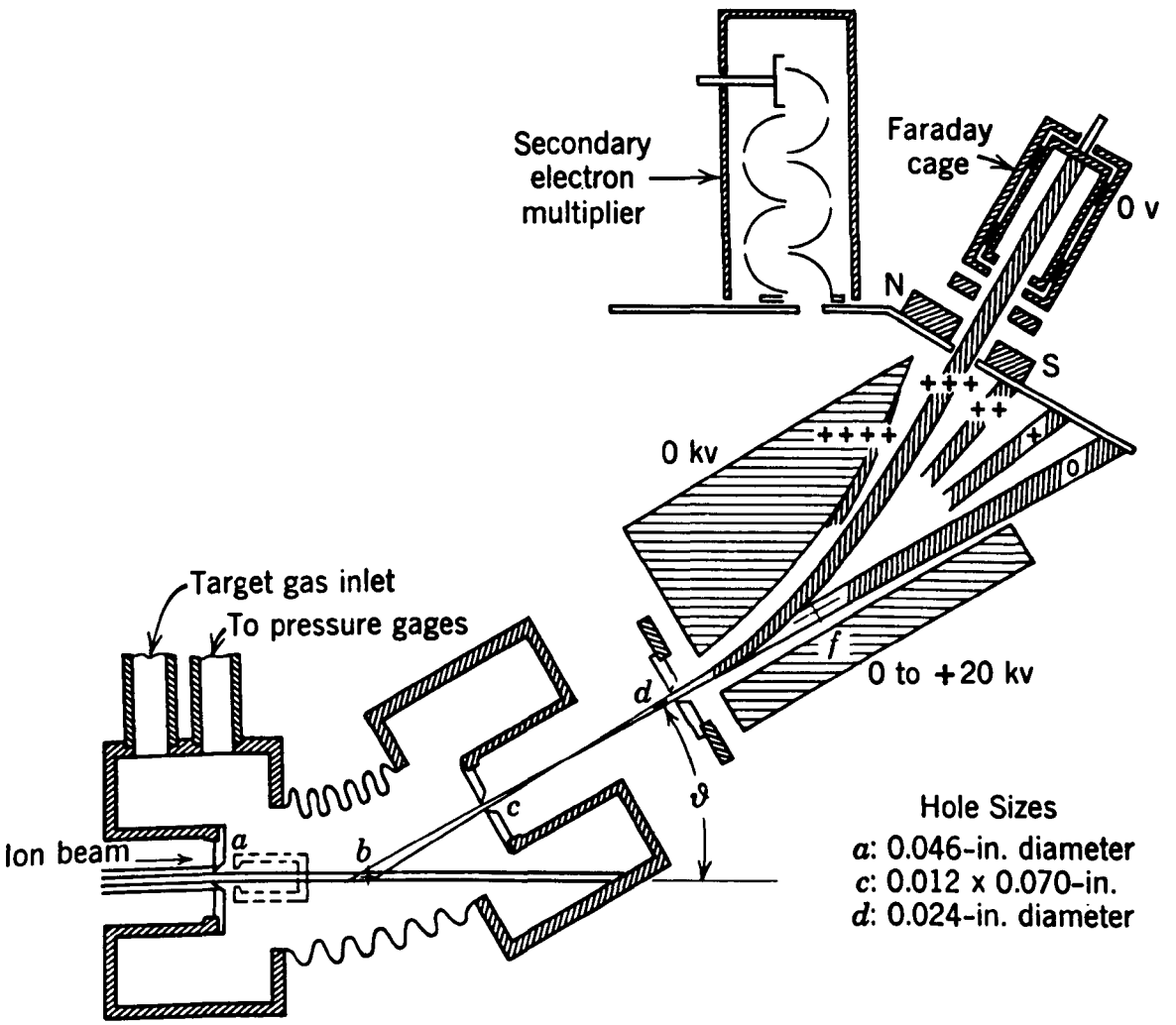
Secondary
electron
multiplier
Faraday
cage
0 v
N
S
0 kv
0 to +20 kv
Target gas inlet
To pressure gages
Ion beam
a
b
c
d
f
ϑ
Hole Sizes
a: 0.046-in. diameter
c: 0.012 x 0.070-in.
d: 0.024-in. diameter

FIG. 3.4

cross-section. As has been seen in Chapter 2, the electron capture probability is an oscillating function of the impact parameter. The oscillatory behaviour is not generally seen in the charge transfer measurements discussed in the previous sections since a particular oscillatory pattern is associated with a given value of the impact parameter and all parameters contribute to the total cross-section. The separate oscillatory patterns are thus averaged out.

The projectile undergoing charge transfer in a gas almost always suffers a small change in direction, and the ions formed in the gas acquire only a small amount of momentum from the projectile. Although the number of projectiles scattered into unit solid angle at polar scattering angle θ decreases as $\mathrm{cosec}^4 \theta/2$, there are an appreciable number of scattered projectiles with angular deviations of several degrees. Such deflections result from encounters in which a fast projectile passes very close to a target particle. Everhart and his colleagues[69,70,71] have performed a series of experiments in which they measured the angular distributions of different charge states produced when singly charged ions struck the target atoms in the collision chamber. One such experimental arrangement for scattering into angles greater than 1° is shown in Figure 3.4. The incident ion beam entered the target gas chamber through the hole a and a few of the large angle collisions occurring near b resulted in the scattered particles passing through the resolution holes c and d. These were analyzed in their several charge states and were then detected with the Faraday cage or secondary electron multiplier. The pressure in the

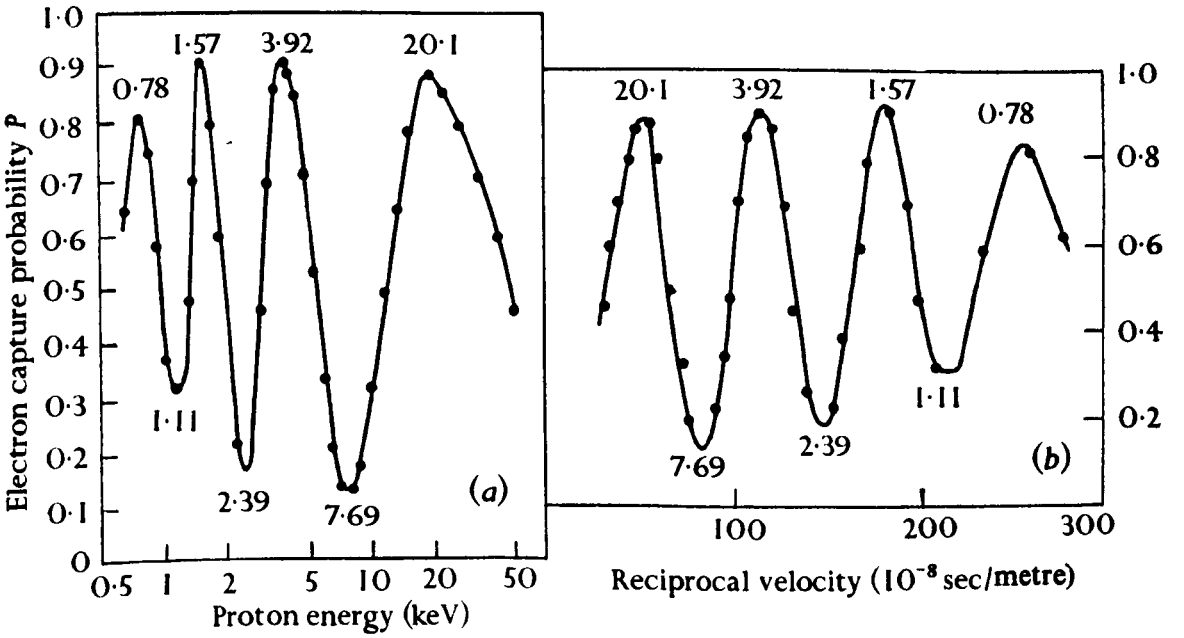
Electron capture probability P
1·0
0·9
0·8
0·7
0·6
0·5
0·4
0·3
0·2
0·1
0
0·78
1·57
3·92
20·1
1·11
2·39
7·69
(a)
0·5
1
2
5
10
20
50
Proton energy (keV)
20·1
3·92
1·57
0·78
1·11
2·39
7·69
(b)
100
200
300
Reciprocal velocity (10⁻⁸ sec/metre)

FIG.3.5

collision chamber was kept low $\sim$ 1 micron of Hg so that almost all the detected particles resulted from single collisions. In addition to the primary rotation about the axis through b, the detectors could be further rotated about an axis through f which permitted any of the detectors to examine an individual component in the scattered beam in any position.

The most interesting results in this case are for protons colliding with hydrogen atoms and molecules. These are shown in Figure 3.5 where the probability is plotted as a function of the inverse velocity of the projectile. Since the inverse velocity is a measure of the time of interaction of the two colliding particles, the results show that in the resonant p + H collision, the electron actually oscillates between one proton and the other as predicted by the theory. This oscillatory behaviour is also predicted for non-resonant cases.

Experiments on these lines have also been carried out by Fedorenko et al[72] with the difference that they used magnetic analysis for the study of the scattered particles.

CHAPTER IV

CONSTRUCTION AND OPERATION OF THE APPARATUS

4.1 Introduction

An apparatus for the study of the angular distribution of multiply charged ions suffering charge transfer includes certain basic units, namely, an ion source which produces multiply charged ions, a momentum analyzer, a lens system, a collision chamber where the reaction takes place, an arrangement to select the post-collision particles scattered in a particular direction, a charge state analyzer, a detection system, and finally the vacuum equipment. The general layout of the experimental set up is shown in Figure 4.1. Multiply charged ions, produced in an oscillating electron ion source were accelerated by the slit system S_1 and momentum analyzed through the analysis chamber which was placed between the rectangular pole faces of the electromagnet forming a 180° mass-spectrometer. The ion beam of known mass, charge state and homogeneous in energy obtained by the analysis, was focussed on the diaphragm 3 by the electrostatic lens consisting of three co-axial cylinders 8,9 and 10. No slit or aperture was placed at the exit of the 180° analysis chamber since diaphragm 3 also acted as a virtual aperture at the exit. The ion beam was collimated by a further aperture 6 before it entered the collision chamber, In the vicinity of the line $x - x_1$ the incident beam encountered the target gas and a small fraction of the incident ions were scattered

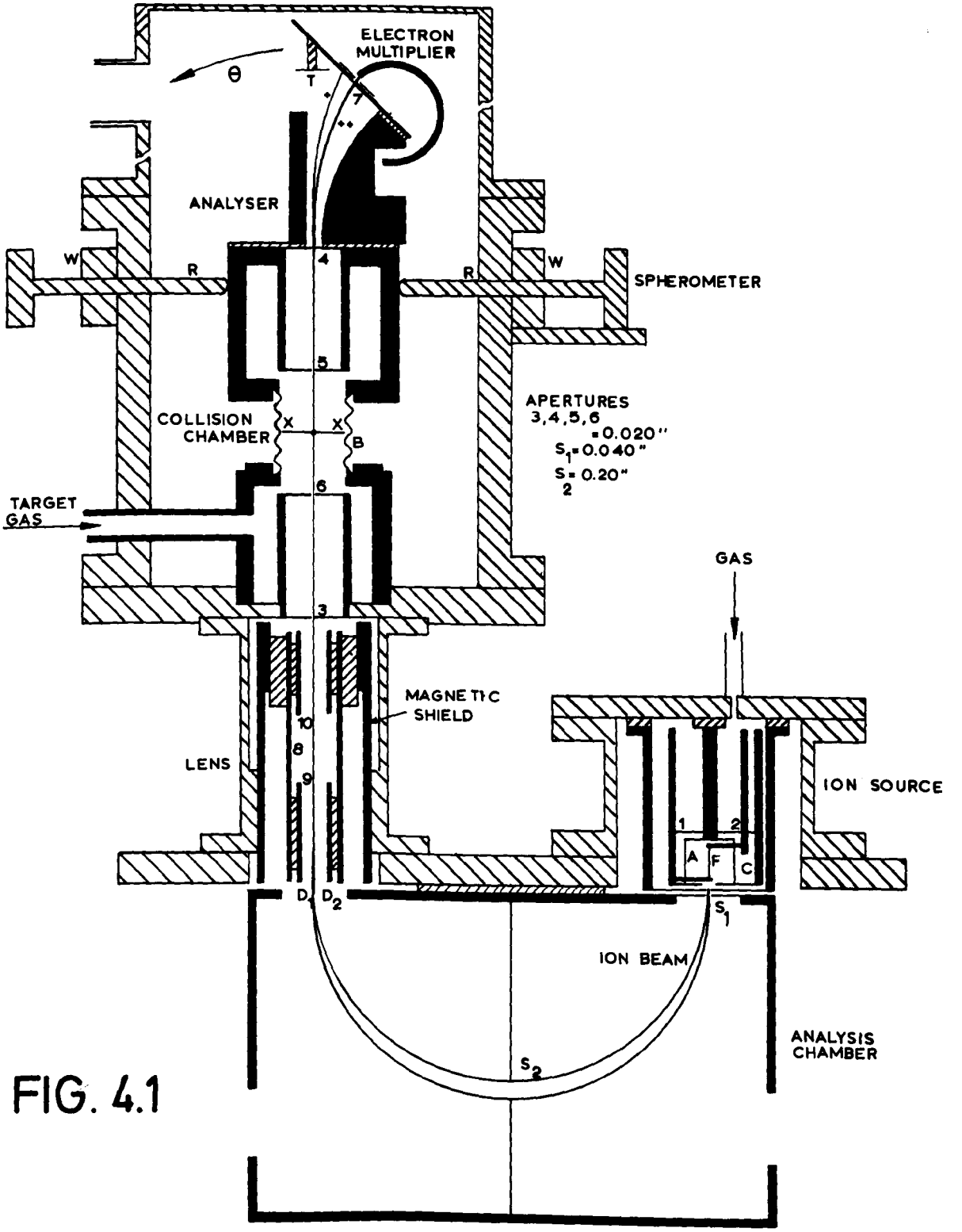
ELECTRON MULTIPLIER
θ
T
ANALYSER
W
R
4
R
W
SPHEROMETER
5
APERTURES
3,4,5,6
=0.020"
S1=0.040"
S2=0.20"
COLLISION CHAMBER
X
X
B
6
TARGET GAS
GAS
3
MAGNETIC SHIELD
10
8
LENS
9
ION SOURCE
1
2
A
F
C
D1
D2
S1
ION BEAM
ANALYSIS CHAMBER
S2

FIG. 4.1

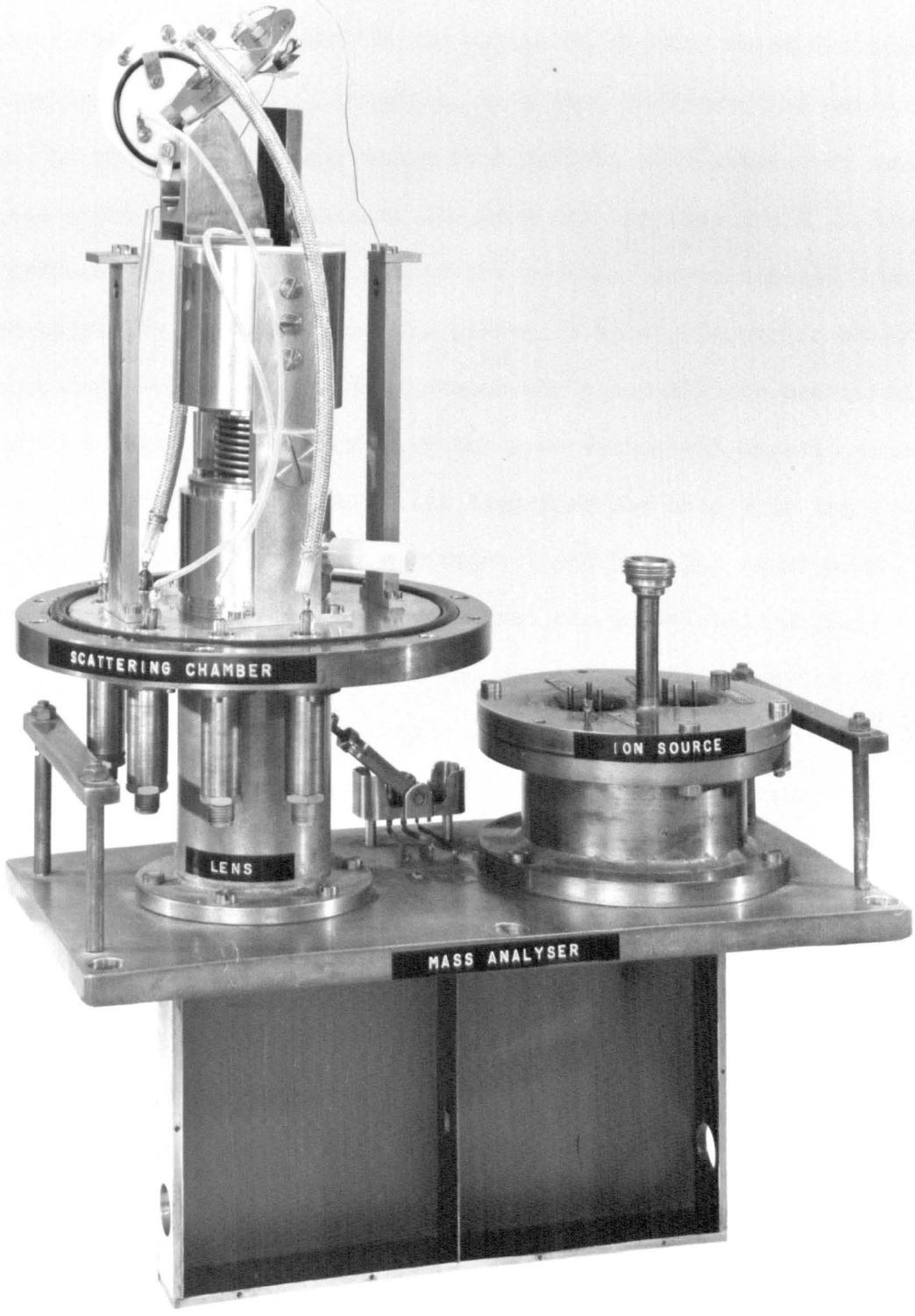
SCATTERING CHAMBER
LENS
ION SOURCE
MASS ANALYSER

to the chosen polar angle O measured by the micrometer and defined by the apertures 4 and 5 which follow the collision chamber. A flexible bellows B allowed the upper part of the collision chamber which included the collimating holes 4 and 5, (together with the) analysing and detecting apparatus, to rotate through any angle to a maximum of 5^{o}, about an axis through the point of intersection of the beam and the line x - x . After passing through holes 4 and 5 back into the vacuum, the collimated beam of scattered particles passed between the plates of an electrostatic analyzer, which separated the two charge state components since all the scattered particles at a given angle have nearly the same mechanical kinetic energy. There was no focussing of the particles therefore the hole 7 in the detector was made larger than the apertures 4 and 5. The continuous channel electron multiplier was used to count the individual particles. The pressure in the collision chamber was such that all the particles scattered in angle resulted from single collisions.

In the following sections the individual systems comprising the apparatus will be discussed in detail.

4.2.1 The Ion Source.

The ideal ion source produces a large current of the desired species of ions with unique velocity and all the ions so produced are in a known state. Most of the sources, however, scarifice certain of the above requirements and different sources have been used in order to satisfy the essential requirements of the experiments for which they are designed.

For reactions at intermediate and large relative velocities, it is usual to use a source which produces large current as this simplifies detection problems. The energy spread in such cases is usually small compared with the impact energy to be acceptable for most experiments. A basic drawback of the electron impact and discharge sources is that the ions are undoubtedly formed in various excited states which produce considerable ambiguity in the interpretation of the experimental data. It is, however possible by utilising mono-energetic electrons with impact energies close to the ionization threshold to produce ground state ions, but under these conditions the ion yield is very small;at such energies the ionization cross-sections and the electron currents are small.

The ion source used for the present work was of the oscillating electron type similar to that described by von Ardenne[73] and Heil[74]. Such a source is efficient for obtaining multiply charged ions and is suitable to work with a 180° momentum analysis system since the same magnetic field can also be used to operate the ion source. It was assumed that most of the multiply charged ions were formed in the ground state.

4.2.2 Principle and construction of the oscillating electron source

Figure 4.2 shows the electrode system and a two dimensional plot of the equipotential lines in an oscillating electron source. The electrons emitted by either of the two filaments F are made to oscillate to and fro in helical paths along the line AB, due to the action of the - + - electric field configuration and the axial magnetic field H.

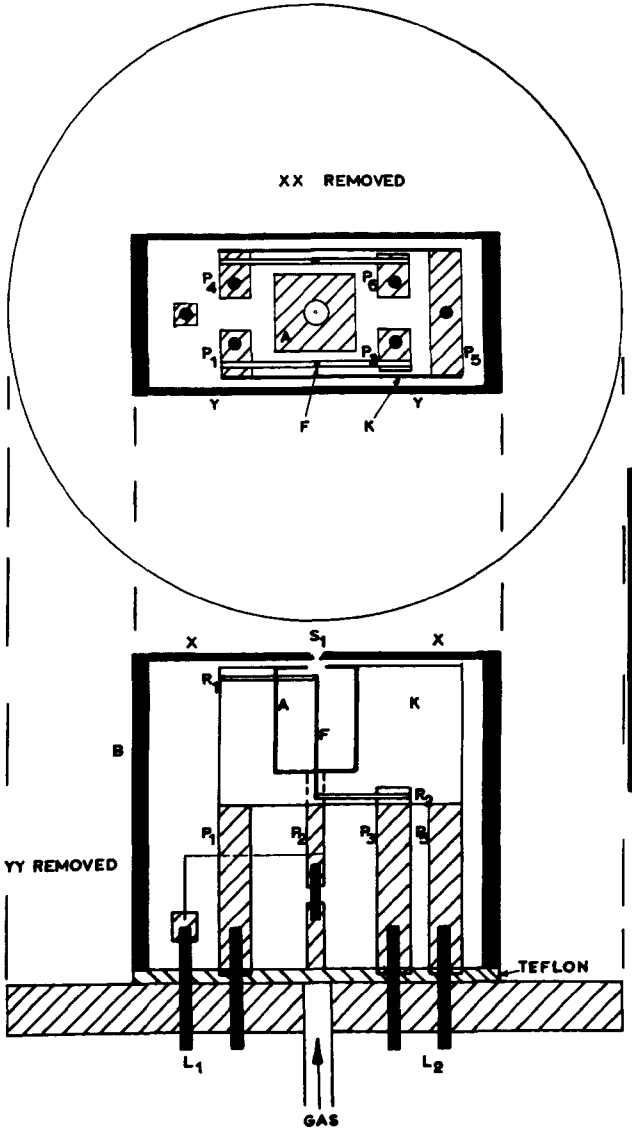

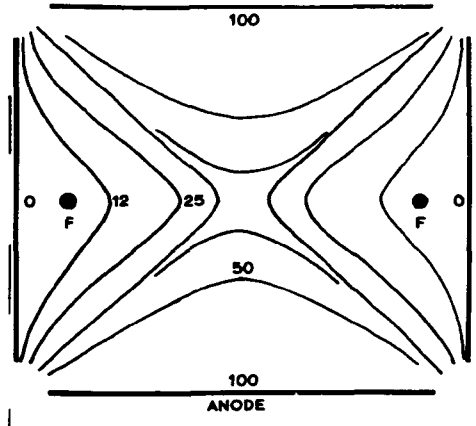

EQUIPOTENTIAL LINES IN A-+- SOURCE

FIG. 4.2

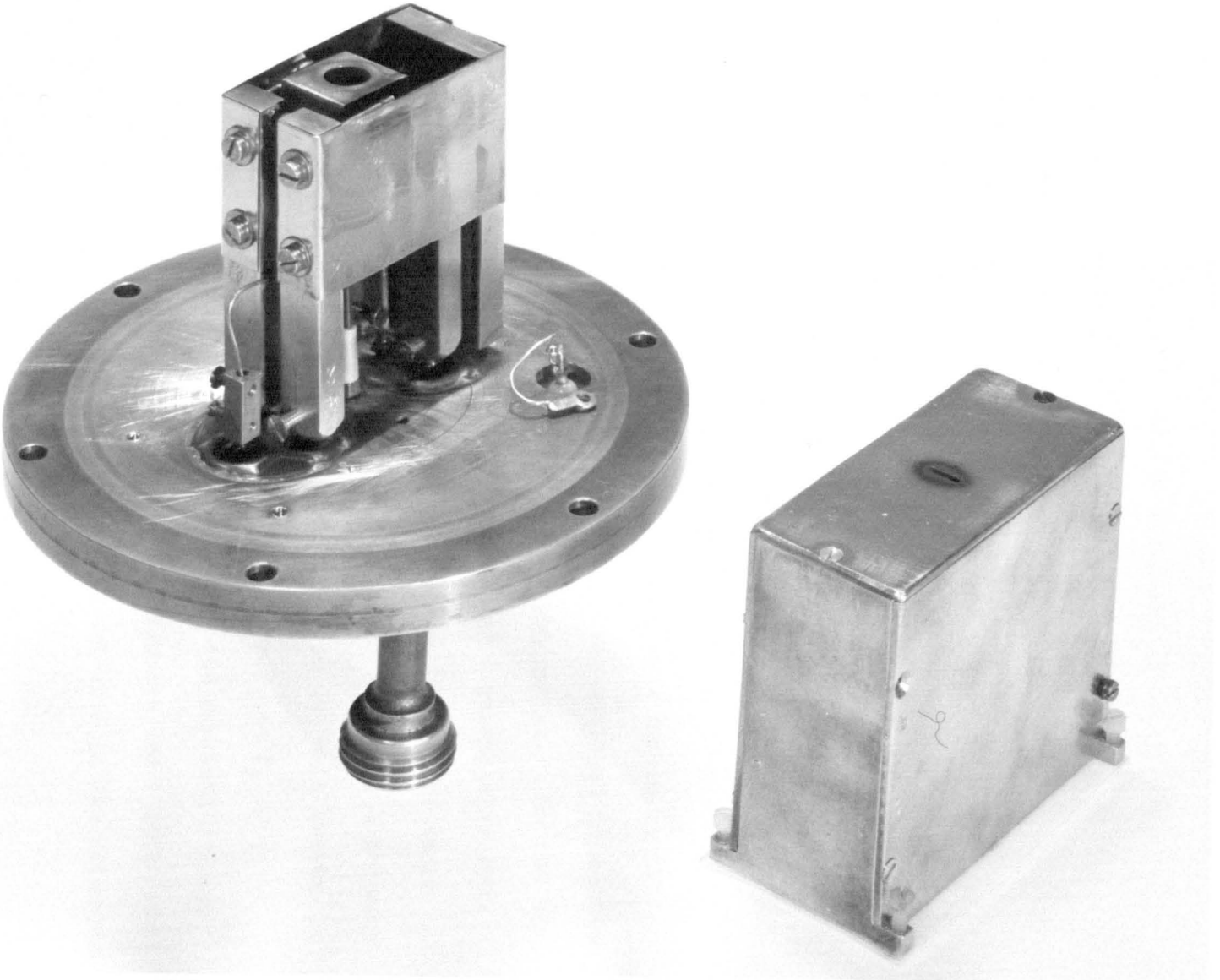

Lateral oscillations between the two cathodes tremendously increase the electron path in the ionization region resulting in an increased ionization efficiency. A magnetic field of the order of 1100 gauss was supplied by extensions attached to the pole faces of the primary analyzing magnet. The source was assembled on a brass plate 5 " in diameter, in which were soldered two three pronged heavy duty lead-in Kovar seals L_1 and L_2. Five brass pillars P_1, P_3, P_4 and P_6 were mounted on seals. These pillars supported two cathode plates made from 0.01" thick ferry sheet and four 2 mm. diameter ferry rods R_1 and R_2 to which two thin tungsten ribbon filaments F were spot welded. The anode was mounted on the brass pillar P_2 which was in turn mounted on a Harwin stand-off insulator. The whole of the electrode assembly was enclosed in a brass box B insulated from the base plate with a teflon gasket. On the top of the box B, a ferry sheet 2mm. thick containing a rectangular slit 5 mm. long and 0.50 mm. wide, was screwed. By enclosing the whole ion source in this box, it was possible to run the source at a pressure of 0.1 mm. of Hg while the background pressure in the main vacuum chamber remained 3×10^{-6} mm. of Hg. The pillars P_1 -- P_6 could be moved upward or downward for final adjustment of the distance between the slits in the slit system S_1 ; one of the filaments was a spare and the design permitted easy replacement in the event of both the filaments burning out.

4.2.3 Power Supply for the ion source.

It is necessary in any collision experiment that the ion beam be

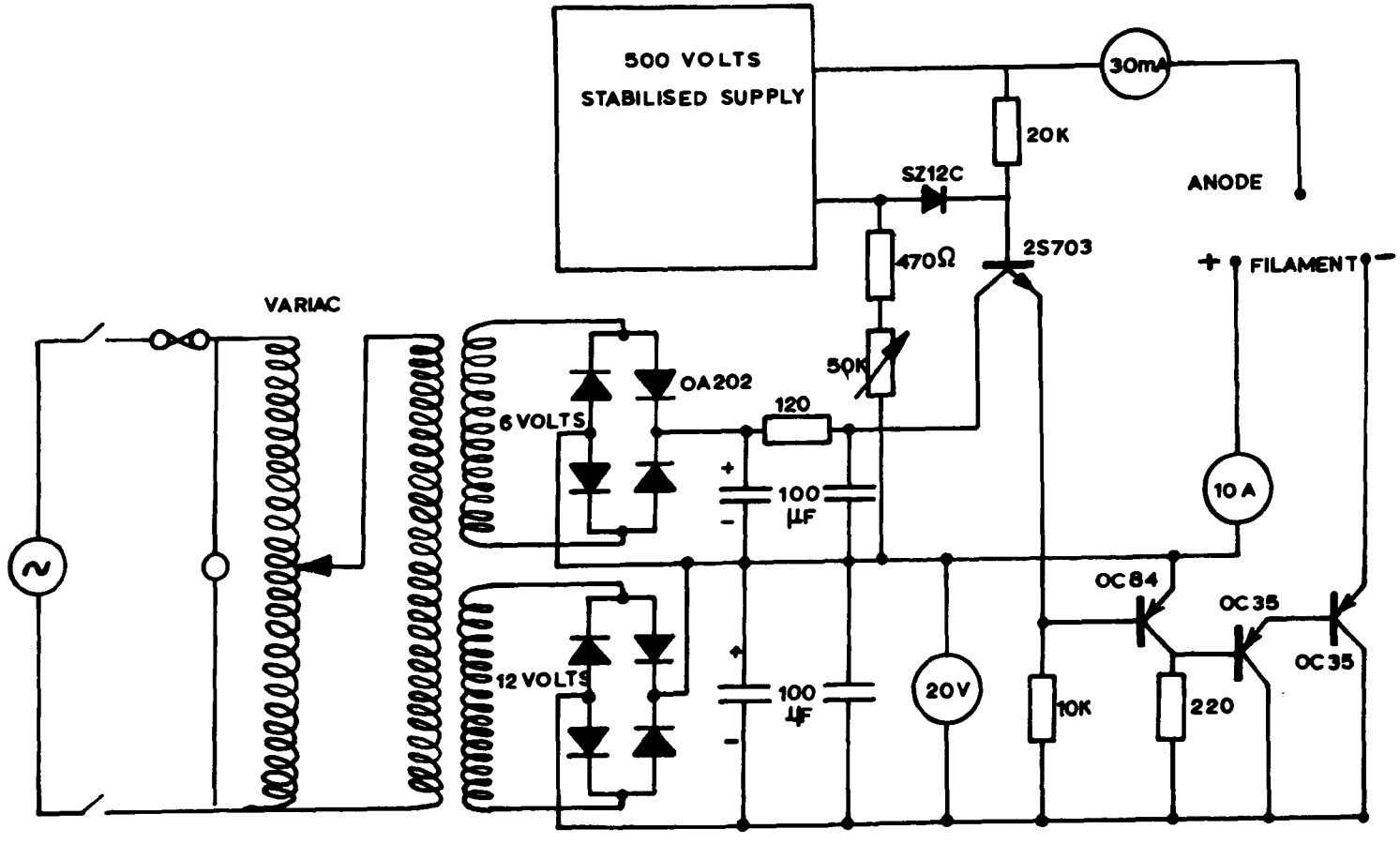

STABILISED EMISSION FILAMENT SUPPLY

FIG. 4.3

highly stable. This was achieved by the stabilized emission filament power supply shown in Figure 4.3. The circuit essentially consists of three units, a stabilised high voltage supply for the electron acceleration, a low voltage high current D.C. supply for the filament and a stabilization circuit. A constant reference voltage of 12 volts is developed across the Zener diode SZ 12C by the high voltage line from the stabilized high voltage supply for the electron acceleration. The voltage developed by the emission current across the variable resistance R_1 and fixed resistor R_2 is compared with the voltage across the Zener diode by the transistor 2S 703. Any change in voltage across R_1 and R_2 due to change in the emission current which in turn may be due either to the mains variations or to the ageing of the filament, is amplified by the transistor OC84 which controls the Darlington pair of OC36 power transistors. For efficient working of this circuit, it was found necessary to use a thin tungsten ribbon filament instead of a tungsten wire since a wire filament has too long a thermal time constant due to which the stabilising circuit frequently became unstable.

4.2.4 Operating conditions for the ion source

It has been observed[75] that by gradually increasing the gas pressure in the source, a critical condition in the arc discharge takes place, a further increase in pressure greatly enhances the current similar to a breakdown condition. A copious number of multiply charged ions can be obtained by working the ion source just below this critical pressure.

A suitable pressure range to obtain doubly charged oxygen ions from carbon monoxide was found to be from 5×10^{-1} to 5×10^{-2} mm. of H.g. Later on to maintain uniform conditions for all the experimental runs, the pressure in the ion source was always kept close to 3×10^{-2} mm. of Hg. It was possible to run the ion source at such high pressures without considerably affecting the background pressure in the main vacuum chamber since two 9" oil diffusion pumps with a pumping speed of 1000 lit/sec used to evacuate the main system.

The ion current drawn out from the source through an aperture of area A is according to Bohm et al[76] that collected by a negative probe of the same area and is given by

$$I_+ = 0.40\, n_+ A \left(\frac{2 K T_e}{m_+}\right)^{\frac{1}{2}}$$

where n_+ and m_+ are respectively the ion density and mass, and T_e the electron temperature. The ion density for the multiply charged ions in the ion source was found to depend upon the electron current and on the mean electron energy. The electron accelerating voltage of 300 volts was found to be suitable to provide an ion current of the order of 10^{-8} amps at the entrance slit of the mass analyser and after mass analysis, an ion current of O^{++} of the order of 10^{-9} amps was obtained.

The gas used in the ion source to obtain doubly charged oxygen ions was carbon monoxide. Oxygen could not be used at such high pressures in the source since it rapidly oxidises the tungsten filament.

4.3.1 Magnetic Analysis

The ion source discussed in the previous sections produces not only singly and multiply charged ions of oxygen and carbon but also the impurity ions of the neighbouring mass numbers due to the background gas. To select O^{++} out of ions possessing different mass numbers and charge states, it is necessary to subject the ions extracted from the source to analysis. A 180^{o} magnetic analysis system was used to separate the required ions.

The electromagnet for the analyser possessed circular pole pieces 7.7" diameter and were introduced into the sides of the vacuum chamber with rubber 'O' ring seals, to reduce the distance between the pole pieces thus achieving stronger field with less magnetic material and fewer ampere turns. An extension 8 " sq. and 3/8" thickness, constructed out of mild steel of relatively low carbon content, was screwed on to the existing circular pole face inside the main vacuum chamber. The final gap between the pole pieces was $2\frac{1}{4}$". The magnet energising current was obtained from a Newport supply which was stabilised to one part in 10,000 and was capable of providing up to 10 amps at 24 volts.

The magnetic field was calibrated by means of an E.M.I. gaussmeter using a small probe which could be inserted between the pole pieces. A typical magnet current/field strength graph is shown in Figure 4.4 . It is necessary that the analysis of the ions be carried out in a uniform magnetic field and it was found that the field was uniform within 1% between two to seven inches from one end of the pole faces,

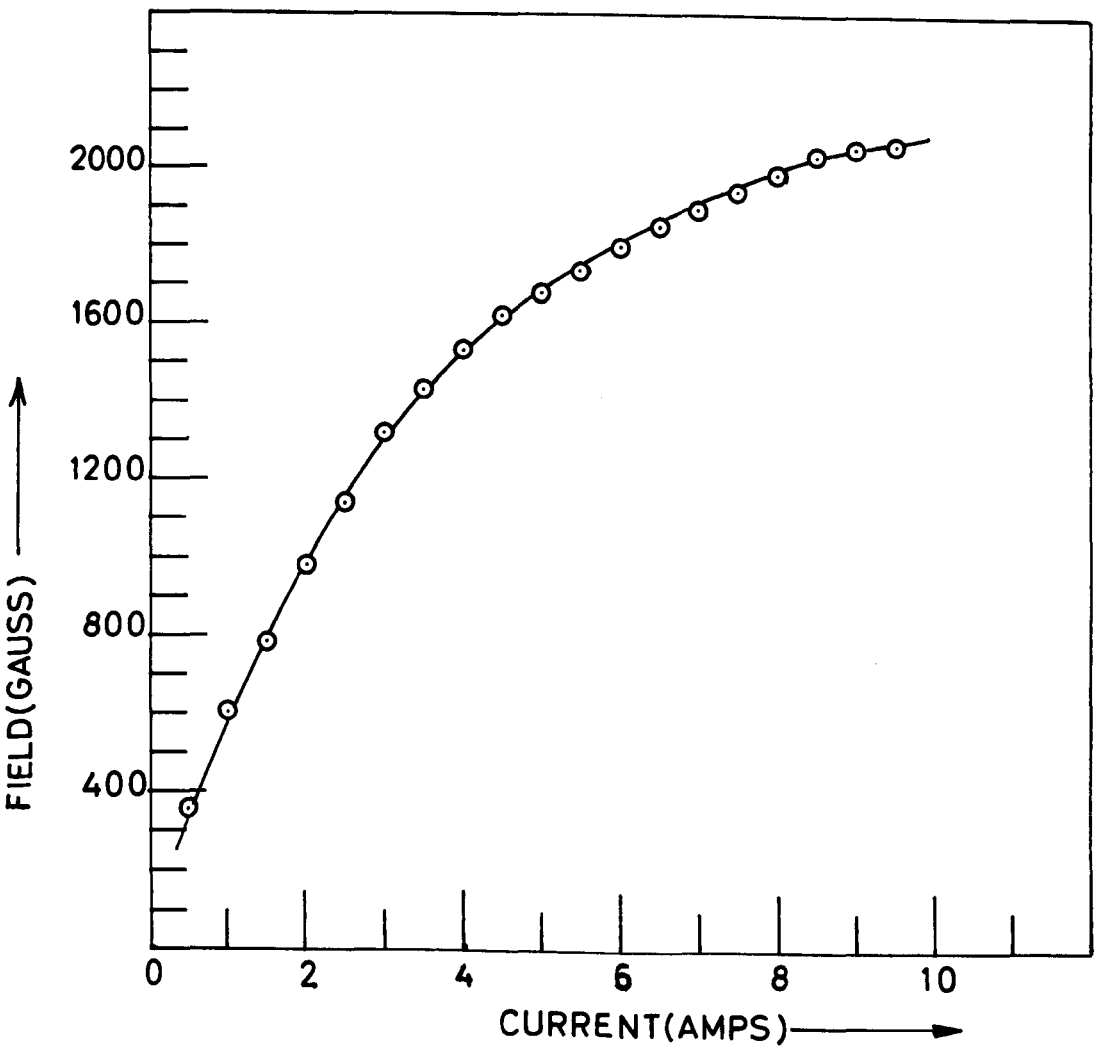

FIG. 4.4

there was a fall of 5% in the magnetic field near the ends.

4.3.2 Analysis chamber

The ion beam after having been extracted and accelerated to appropriate energy must be analysed in an equipotential region. The beam was therefore enclosed in a rectangular analysis chamber, shown in Figure 4.1 which was constructed out of 1/16" brass sheet having dimensions 1" x $8\frac{1}{2}$" with 5" depth. It was found that the bombardment by the unwanted ions on the walls resulted in the formation of insulating surfaces which accumulated charges. This produced electric fields inside the chamber and was responsible for the fluctuation and instability of the ion beam in the collision chamber. The inner surface of the analysis chamber was therefore coated with aquadag, a colloidal solution of graphite in water. Aquadag is believed to have the added advantage of a low secondary emission coefficient. The coating of the surface with dag was however not a permanent solution since due to prolonged use the surface became contaminated and it was necessary to clean and recoat the chamber at regular intervals. This was done whenever the vacuum system was let to air for changing the filament in the ion source.

The analysis chamber was screwed to the top plate by means of four 2BA nylong screws and insulated from it by a teflon sheet. When the top plate was bolted on to the main vacuum chamber the analysis chamber was situated between the square pole faces of the magnet in the region of the maximum homogeneity of the magnetic field.

4.3.3 Resolution of the instrument

In a single focussing instrument of this type, the radius of the trajectory of each particle is proportional to Mv, where M represents the mass and v the velocity of the particle. The system thus yields a momentum spectrum and can be converted into a mass spectrum only if mono-energetic ions are produced in the ion source. If in a 180° mass-spectrometer, the distance between the infinitely narrow entrance and exit slits is 2R, the ions are incident on the entrance slit from the source with an angular divergence 2α and if the region between the pole faces is free from electrostatic fields, then

$$H^2R^2 = \frac{20880\ MV}{\varepsilon} \qquad 4.1$$

where H is the magnetic field in gauss, R is the radius of the trajectory in cms, M is the mass in atomic units, V is the energy in volts, ε is the charge on the ion measured in terms of a single electronic charge. The maximum angle of acceptance, is usually set by an aperture and for experiments requiring a collimated ion beam is necessarily small, less than 5°. Figure 4.5 shows the path for an ion beam with an exaggerated angle of divergence 2α in such an instrument. According to Barnard[77] the mass resolution can be calculated on the following lines. As can be seen, the spherical aberration at the first order focal point F is $r\alpha^2$. The image spread for the two ion rays starting at the point O and making an angle α with each other, in the plane of the exit slit would be $S_1 + r\alpha^2$, where S_1 is the width of the entrance

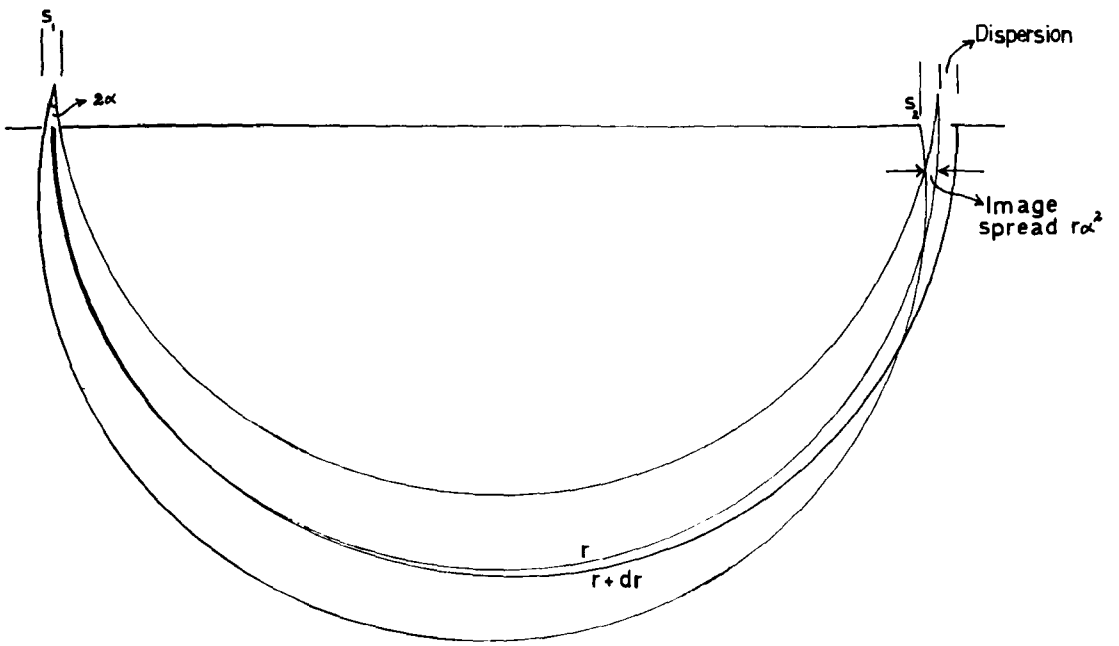

FIG. 4.5

slit. The dotted line shows the path of the central ray of mass $M + \Delta M$ with a trajectory radius of $R + \Delta R$. If both the ions of mass M and $M + \Delta M$ are accelerated through the same energy V, then the two masses will be resolved only if the dispersion $2\Delta R$ is equal to or greater than the exit slit width S_2 plus the total image spread $S_1 + \alpha^2 r$, i.e;

$$2\Delta R = S_1 + S_2 + \alpha^2 r \qquad 4.2$$

making use of equation 1, for the two ions,

$$\frac{M + \Delta M}{(R + \Delta R)} = \frac{M}{R^2} \qquad 4.3$$

Simplifying equation 4.3 with the aid of 4.2 and neglecting ΔR^2, the resolution is given by

$$\frac{M}{\Delta M} = \frac{R}{S_1 + S_2 + \alpha^2 r} \qquad 4.4$$

assuming that the ion beam is parallel at both the entrance and the exit slits, the maximum resolution is then given by

$$\frac{M}{\Delta M} = \frac{R}{S_1 + S_2} \qquad 4.5$$

The energy spread in the ion source introduces a lower limit to the mean energy at which the ions should be analysed. For an angular divergence 2α and radius of trajectory R,

$$\alpha^2 R^2 \propto MV \qquad 4.6$$

where M is the mass of the ion and V the analysis energy. For an energy spread ΔV in the ion source, two neighbouring masses M and M + ΔM will be resolved if

$$MV = (M + \Delta M)(V - \Delta V) \qquad 4.7$$

i.e; the resolution is given by

$$\frac{M}{\Delta M} = \frac{V}{\Delta V} \qquad 4.8$$

For a typical ion source V = 10 volts and to have a resolution of twenty, V $\sim$ 200. Willmore[78] has found that the current extracted from the ion source varies as $V_a^{3/2}$ where V_a is the potential on the accelerating electrode outside the ion source. Therefore if V is used both for extraction and analysis, as was the case in the present work, it is imperative to have V $>$200 to extract a sizeable amount of ion current from the ion source and to have the required mass resolution. The extraction of the ions from the source and the analysis were carried out at 350 volts which gave an initial energy of 700 eV to the doubly charged ions required for the experimental work. Experimental studies below this energy can only be carried out with an elaborate retarding lens system resulting in a considerable loss of ion beam intensity. In fact the present work was confined to only two energies, namely 1200 eV and 2600 eV. The required energy was obtained by accelerating the ions after the analysis. As will be discussed later, studies of angular distribution are not very sensitive to the energy spread within the energy range of the present work.

In the 180^{o} system used for the present experimental study the radius R of the central trajectory was 7.62 cms, S_1 and S_2 were each 1mm x 5mm, which gives a maximum resolution of 38. The experimental resolution determined from the half widths of the various mass peaks was found to be 28, this low value is attributed to the energy spread of the ion source and the acceptance angle of the entrance slit to the mass spectrometer. The angle of acceptance was reduced by placing a 5 m x 5 mm stop at 90^{o} in the analysis chamber. The gas used in the ion source was 99.9% pure CO and it was only necessary to separate O^{++} from C^{+}, C^{++} and the impurity ions N^{++}, very high resolution was therefore not required. The energy spread due to such a low value of the resolution which was measured from the subsequent electrostatic analysis of the beam was found to be 15 volts. The reaction being studied is however not sensitive to such an energy spread.

4.4.1 The Einzel Lens

In an ideal mass spectrometer, the magnetic field must be homogeneous and should possess sharply defined boundaries. This is difficult to realize in practice and in general the trajectory of the emerging ion beam has a curvature due to the fringing flux. This is an undesirable feature particularly in an 180^{o} system since this makes extraction of the beam from the spectrometer far more difficult if the ion-atom collision studies have to be made in a magnetic field free region. The problem is further complicated due to the fact that for the study of the angular distribution of the projectiles after collision,

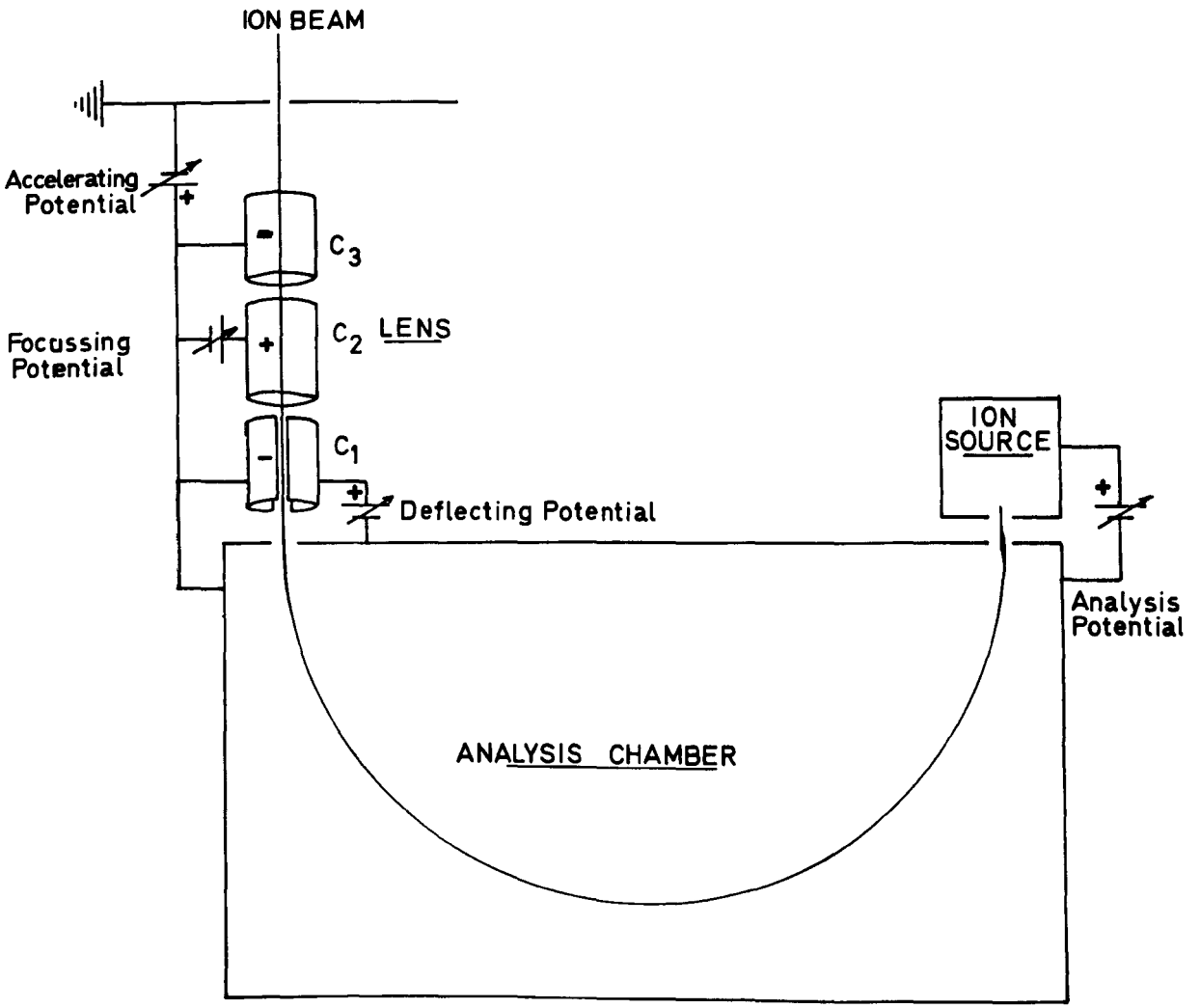
ION BEAM
Accelerating Potential
C3
Focussing Potential
C2 LENS
C1
Deflecting Potential
ION SOURCE
Analysis Potential
ANALYSIS CHAMBER

FIG. 4.6

a narrow and well collimated beam is required. The beam extraction was simplified by removing the exit slit S_2 of the mass spectrometer, using deflector plates to compensate for the curvature of trajectory of the ion beam and by employing an electrostatic lens to cast a virtual image of the entrance slit (Figure 4.1) to the collision chamber at the exit of the spectrometer. It was observed that the removal of the slit S_2 did not impair the resolution of the instrument.

The lens, which was mounted in a soft iron cylinder to screen it from the fringing flux and insulated from it by a Teflon cylinder, consisted of three co-axial brass cylinders C_1, C_2 and C_3 which had the following dimensions;

C_1		C_2		C_3	
diameter	length	diameter	length	diameter	length
0.6"	1.5"	0.8"	3.8"	0.6"	1.5"

Figure 4.1 shows the arrangement of the cylinders to form what is known as the "Einzel", "Univoltage" or "Symmetrical" lens. The cylinders C_1 and C_3 were fixed inside the cylinder C_2 with 10BA brass screws and insulated from it with Teflon washers. C_1 was split along its axis into two halves, so that it was also possible to apply a small potential for the lateral deflection of the beam and were so arranged that the deflection was in the plane containing the circular orbit of the ions in the spectrometer.

Figure 4.6 shows the electrical connections for accelerating and focussing the ion beam after it has been analyzed. C_1 and C_3 were

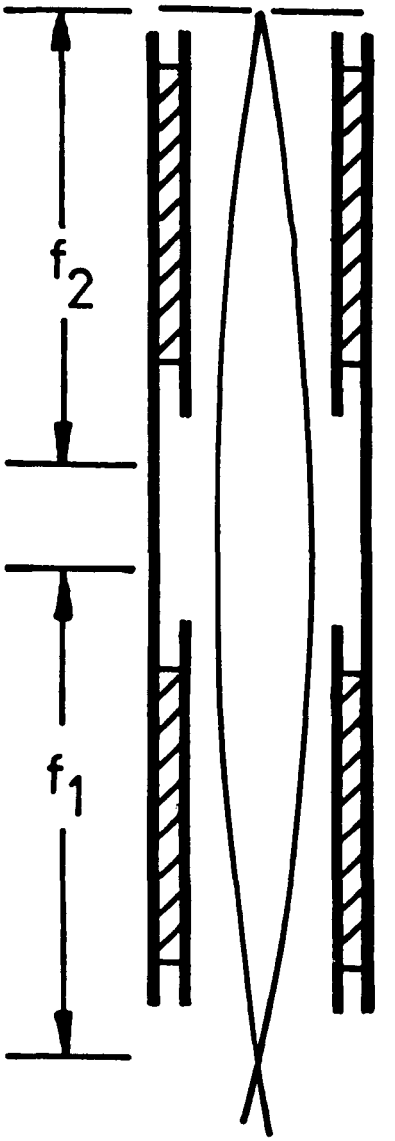

FIG. 4.6a

were connected together and the potential difference between them and C_2 could be varied for focussing the beam while the ion beam could be accelerated by varying the potential difference between C_1, C_3 and the analysis chamber. If V_a is the analysis voltage and V the potential difference between C_1, C_3 and the analyser, then the potential on C_1, C_3 with respect to the ion source is $V_1 = V_a + V$, and if V_2 is the potential of C_2 with respect to the source, then the two focal lengths f_1 and f_2 of the lens shown in Figure 4.6a are given by[79]

$$\frac{f_2}{f_1} = \left(\frac{V_2}{V_1}\right)^{\frac{1}{2}} \qquad 4.9$$

The advantages of using such a lens are obvious from the above equation, namely, the "power of the lens depends on the ratio of the potentials on the outer and inner cylinders and the total effect is always converning for all positive ratios whether $V_1 > V_2$ or $V_1 < V_2$ as long as both have the same sign. For a negative ratio however, the lens acts as a mirror. Thus by varying V_1, the required ion energy could be selected and by varying V_2 the focal length could be adjusted at will over a considerable range.

4.5.a <u>The Scattering Apparatus</u>

The scattering apparatus shown in Figure 4.7 (a,b) consisted of (i) Collimation system, (ii) the collision chamber, (iii) the angular resolution apertures, (iv) the electrostatic analyser and finally (v) the electron multiplier for the detection of the scattered ions.

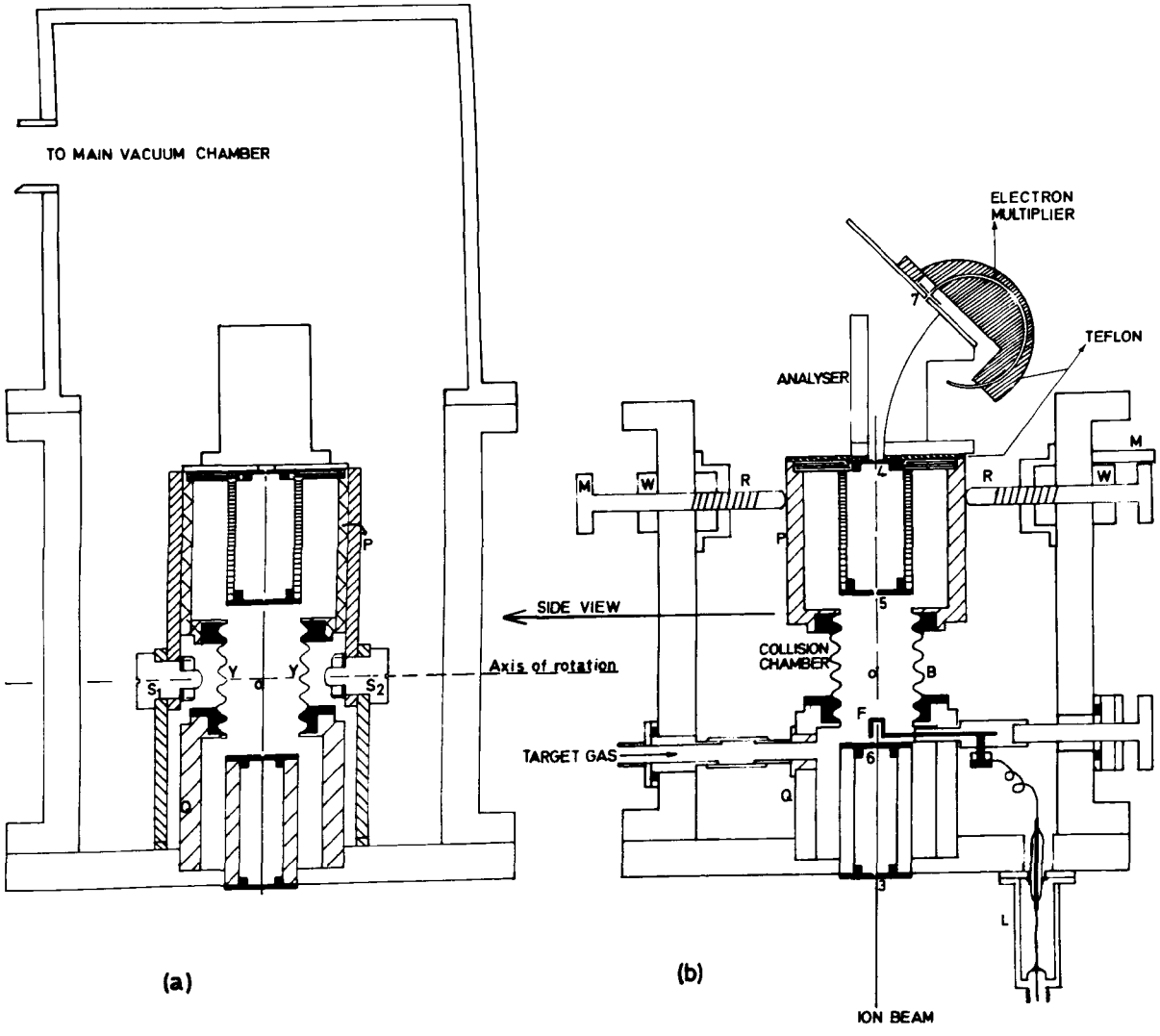

FIG. 4.7 SCATTERING APPARATUS

Different pieces from which the apparatus was assembled were made in the college workshop with tolerances, as far as possible less than 0.001". Accurate alignment was achieved by mounting the separate component on a circular brass plate $\frac{1}{2}$" thick and 7" in diameter. The design was such that any soldering of components was altogether avoided, thus eliminating distortions and imperfections arising from heating. Two brass discs, containing collimation apertures 3 and 6 each countersunk away from the beam and 0.020" in diameter, were screwed on to a brass cylinder which in turn was screwed to the main plate. High vacuum in the collimation region was obtained by differential pumping through four large holes peripheral to the system. This avoided the attenuation of the main ion beam during collimation and before entering the collision chamber. The intrinsic divergence of the ion beam emerging from the 180° mass spectrometer naturally presents difficulties in performing differential measurements since for such measurements a well collimated cylindrical beam is essential. The necessary collimation was, therefore, introduced by focussing the beam on to 3 by the cylindrical lens described in section 4.4.1 and restricting the angular divergence by aperture 6. Unfortunately this technique involves an unavoidable loss of the ion beam intensity in the collision region. Coincidence between the axes of lens and collimation system was achieved by screwing the collimation system into the brass plate and providing an accurately concentric recess to receive the flange carrying the lens system. The assembley of this system therefore automatically provides an accurate

alignment between the scattering apparatus and the lens system.

A small collector cage F placed directly behind the hole 6 acted as a monitor on the incident ion beam, as it could be moved into or out of the path of the incident ion beam as desired, thus providing a direct measurement of the incident beam inside the collision chamber. When maximum of the desired ion beam had been obtained by adjusting the necessary lens and deflecting potentials, the rotary shaft seal attached to the collector cage via an insulating Teflon cylinder permitted the removal of the cage from the path of the beam. The electrical connection from the cage was taken out through the high insulation glass metal seal L.

The collimation system was enclosed by another brass cylinder Q which was also screwed to the brass plate. On the sides of this cylinder, two holes were provided, one for the connection to the target gas supply and the other for the Teflon rod carrying the collector cage. A stainless steel bellows B, 1" long and 1" in diameter carrying a threaded brass flange on one end and a plain flange on the other, was fixed on to the cylinder Q. The brass cylinder P which contained the resolution system (cylinder carrying apertures 4 and 5), was screwed on to the threaded flange of the bellows. The volume inside P, Q and the bellows B, excluding the volume inside the collimation and the resolution system defines the gas filled region. As seen in Figure 4.7a two brass plates 3/16" thick and 1" wide fixed on flattened sides of the cylinder P, were joined by two tight fitting screws S_1, S_2 to two

other similar brass plates fixed on the base plate. This assembly thus held P in position and together with the bellows permitted the resolution holes (4,5) to be rotated about the axis YOY in such a way that the line joining the centres of 4 and 5 always intersected at the same point O on the primary ion beam axis. The tolerances in the lengthwise dimensions of the brass plates and the location of the holes for S_1, S_2 were such that (i) at zero angle, the resolution holes 4,5 were optically in line with the collimating apertures 3, 6 and (ii) as the cylinder P was rotated in angle, the axis YOY remained fixed in position i.e., there was no lateral movement or tilting of the cylinder. The rotation of the cylinder from outside the vacuum was carried out by two $\frac{1}{4}$" rods R of the rotary shaft seals placed diametrically opposite in the outer brass chamber. The portions of the rods R projecting inside the vacuum chamber were threaded with a pitch of 0.025" and were kept in position by two tapped brackets fixed inside the brass chamber. The vertical position of the rods above the axis of rotation YOY was such that 0.040" forward movement of the rod on the right and an equal backward movement of the rod on the left corresponded to an angular rotation of the cylinder P by 1°. The initial alignment of the collimation holes (4,5) with (3,6) for zero angle was made optically, final adjustment was made by setting the position for maximum primary beam intensity.

Two electrodes, one plane and the other curved having a radius of curvature of 2.75", which formed a simple electrostatic analyzer

to separate the two charge state components, were mounted on the cylinder P. These electrodes were insulated from P by nylon screws and a Teflon disc 1/16" thick. The curved electrode was grounded and the ions were deflected towards it by applying a variable positive potential on the plane electrode. The channel multiplier assembly was fixed on the curved electrode. By adjusting the positive potential on the plane electrode desired ions could be allowed to strike on the input end of the multiplier through aperture 7 in the brass disc. Since in this type of analyser, there is no arrangement for focussing of the ions, the aperture 7 was 0.040" i.e., twice as large as the size of the resolution aprtures. This was to account for the defocussing that would occur during the analysis of the ions.

The aperture 7 being at ground potential and the input end of the multiplier at - 3KV, the ions were therefore further accelerated through this potential which enhances the detection efficiency. A ferry electrode with an aperture of 0.040" and held at - 90 V with respect to the input end of the multiplier suppressed the secondary electrons from escaping from the multiplier due to the strong field gradient towards the grounded brass disc containing 7.

The upper half of the outer brass chamber, enveloping the scattering system was connected via a 1" diameter yorkshire tubing to the main vacuum chamber to provide differential pumping for the space outside the collision chamber. The pressure in this part was therefore always less than 5×10^{-6} mm of Hg when the pressure in the

collision chamber was 5×10^{-4} mm of Hg.

The electrical connections to the analysis plate and the multiplier were provided through vacuum glass metal seals similar to L (not shown in the diagram).

The inner surface of the collision chamber was coated with aquadag to prevent anypossible insulating surfacesthat could be formed due to the bombardment of the ions,thus avoiding the build-up of charge on the surface which would then disturb the paths of the scattered ions.

4.5.2 Angular Resolution

Consider the geometry of the scattering region as shown in Figure 4.8. The shaded area, of the primary beam which has a diameter d and is moving along the Z axis, is the target volume defined by the resolution holes set at an angle of θ. If s is the diameter of the resolution holes S_1, S_2 and y_1, y_2 respectively their distances from the scattering centre, then length L of the target volume for a given polar angle θ is given by

$$L = s \operatorname{cosec} \theta \, (y_2 + y_1)/(y_2 - y_1) \qquad 4.10$$

while the number of particle N scattered per second into the resolution holes is

$$N = n N_o L \sigma (\theta) \, d\Omega \qquad 4.11$$

where n is the number of the target particles per unit volume, N_o is the number of incident particles per second, $\sigma(\theta)$ is the particle differential cross-section and $d\Omega$ is the effective solid angle of acceptance. For the present experimental work,

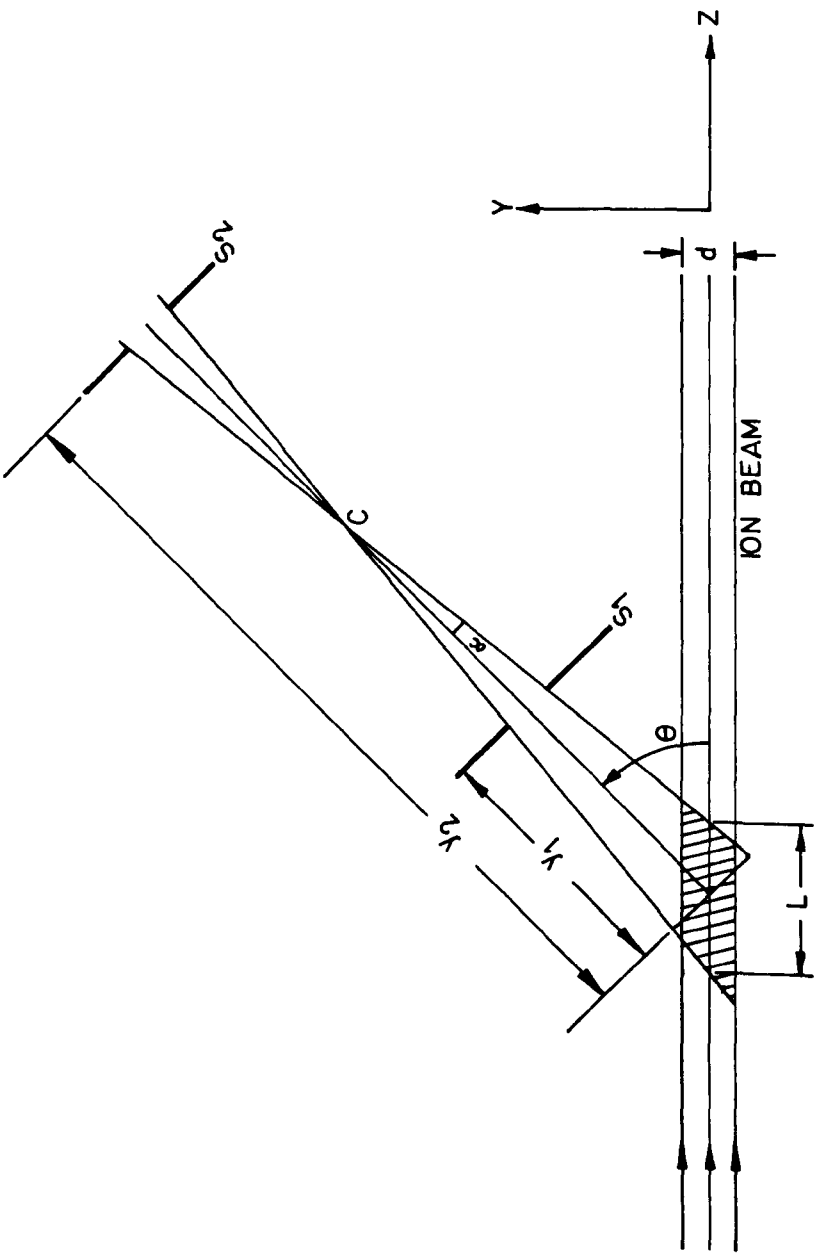

FIG. 4.8

$S_1 = S_2 = 0.020"$, $y_1 = 0.80"$ $y_2 = 3.00"$

which gives an extreme angular resolution of

$$\alpha = \pm \frac{S}{(y_2 - y_1)} = \pm 0.50^{o} \qquad 4.12$$

although due to the cylindrical nature of the primary beam, most of the scattering comes from a more narrow angular range of about 0.3 degree. Such a poor value of the angular resolution as it is, was nevertheless found to be an unavoidable feature mainly due to the fact that the doubly charged ion beam intensity was very low because of the collimation. As seen by equation 4.9, 4.10, the number of particles scattered into a solid angle $d\Omega$ depends upon

i. N_o, which is the primary beam, which was very low

ii. $\sigma(\theta)$ which for most of the measurements decreases with increasing angle

iii. L, the scattering length also decreases with the increasing angle

iv. n_1 the number of target particles which cannot be increased indefinitely due to multiple collisions.

Therefore for given N_o, $\sigma(\theta)$ and n_1 any attempt to increase the angular resolution either by increasing y_2 or decreasing S, severely limits the angular range of the experiment at intermediate energies. Similar studies by Everhart[80] and others[81] did not suffer from these defects because (i) the singly ionized beams they used can be obtained in abundance and (ii) there are less severe collimation problems at higher energies, consequently smaller loss of ions during collimation.

4.6.1 The Particle Counting System

The number of particles scattered in the charge transfer process are very small particularly at large angles, therefore for accurate measurements, single particle counting technique was necessary. For this purpose a continuous channel electron multiplier with a gain of 10^8 was used. The multiplier and the allied counting system employed will be described in the following sections.

4.6.2 The continuous channel electron multiplier.

The continuous channel electron multiplier is a recent development along the lines of windowless particle detectors and is essentially a curved capillary tube having dimensions such that the length to inside diameter ratio ranges from 50 - 100. The inside diameter may be from less than a tenth of a millimetre to about one millimetre. The multipliers obtained from the Bendix corporation and Mullards had an inside diameter of 1 mm and length to diameter ratio of 100. The capillary tube had the form of an arc extending over 3/4" of a circle having a radius of curvature of about 2 cms. A layer of special semi-conducting material, having secondary electron emission characteristic suitable for an electron multiplication process, is deposited over the interior surface of the tube. The ohmic resistance of the semi-conducting layer ranges from 10^8 to 10^{11} ohms. Of the two multipliers used, the one made by Bendix had a resistance of 5×10^8 ohms, while the second made by Mullard had a resistance of 10^9. This resistance is the determining factor for both power dissipated in the channel and any effects associated with its RC

relaxation time. A potential difference applied between the ends of the tube developes an axial electric field. Any electron, ejected from the inside surface either by the photo-electric effect or the secondary emission process, will thus be accelerated down the tube and will also drift across the tube with the lateral velocity acquired during the emission process. The electron multiplication occurs when the potential difference and the dimensions are such that these free electrons gain enough energy from the electric field before they encounter the surface again, normally more than one secondary electron is generated at each encounter. Thus under these conditions a single electron emitted at the input end of the tube will result in an electron cascade at the output end of the channel.

The exact nature of the semi-conducting surface has not been published although it has been shown by Angel[82] that the relative spectral response of the material of the multiplier (made by Bendix) to the photo-electric effect is similar to that of tungsten, implying a work function of 4 eV. Thus the channel has essentially no background noise due to thermionic emission of the electrons. The surface is quite stable with respect to changes in secondary emission ratio after extended and repeated exposure to the atmosphere, which makes it far more easy to handle than the conventional dynode type electron multipliers. Moreover its simplicity, small size, ruggedness and the fact that it can be operated at pressures up to 10^{-4} mm of Hg without any loss of efficiency, make it ideal for use in this experiment.

The experimental set-up is shown in Figure 4.7 and 4.10. The multiplier was supported on a 3/16" thick Teflon block inside a groove of the same radius as the channel and secured to it by small ferry sheet strips. The Teflon block was fixed on to the brass disc in such a way that the input end was in front of the entrance hole of the ion beam. A ferry electrode with 1.5 mm diameter hole was inserted between the disc and the tube and biassed 90 volts negative with respect to the input end. This was necessary due to the reason that the disc being at ground potential and the input end of the multiplier at $\sim$ - 3KV, most of the secondary electrons emitted near the input end of the channel would move towards the disc and not towards the output end of the channel which of course would result in the loss of electrons and the low counting efficiency. The - 90 volts electrode inserted between the disc and the input end effectively eliminated the field penetration and reduced the loss of secondary electrons. The output end of the channel was covered by a foil (the Mullard channel had the output end closed) to collect the total charge of the cascade. The voltage pulse developed across the shunt capacity of the collection system was fed to the counting system. The input end of the tube was operated at a potential of - 3 KV to - 4 KV with respect to the output end which was grounded through the 15 K resistor. The H.T. was supplied by the Harwell 2000 series transistorized supply type 2124 with a stability of 0.01%. The counting response is observed with ions having an energy of a few hundred electron volts, above this threshold the secondary emission ratio and, therefore, the counting efficiency

rapidly increases with increasing ion energy and remains large for ion energies up to several hundred keV. Examination of the diagram in Figure 4.10shows that by applying a negative potential of $\sim$3 kV the ions entering through the aperture 7 in the disc are further accelerated through this potential thus giving a higher counting efficiency.

For a given ion energy, it was observed that the size of the output pulse increased with increase in the potential difference across the tube until saturation sets in, when the electron gain was about 10^7 to 10^8, then the output pulses were of uniform amplitude. A P.D. of 3.3 kV was enough to achieve this gain. It is believed that during the electron multiplication process, a positive charge accumulates upon the walls of the tube because of a net loss of electrons from the surface, the potential gradient flattens out near the output end and the cascade electrons can no longer acquire the energy necessary to support the multiplication process, this is then responsible for the saturation in the gain of the channel.

Inside the channel, the interaction of the cascade electrons with the residual gas molecules,produces ions which are accelerated by the electric field towards the input end of the tube where they may interact with the wall to initiate a new cascade resulting in an increase in the rise time of the output pulse which may be 0.5 μsec for a straight channel, followed by a long tail, giving an overall dead time of 100 μsec. A curved channel multiplier retains the ions in the back where their effect on the overall gain would be clearly negligible and reduces the

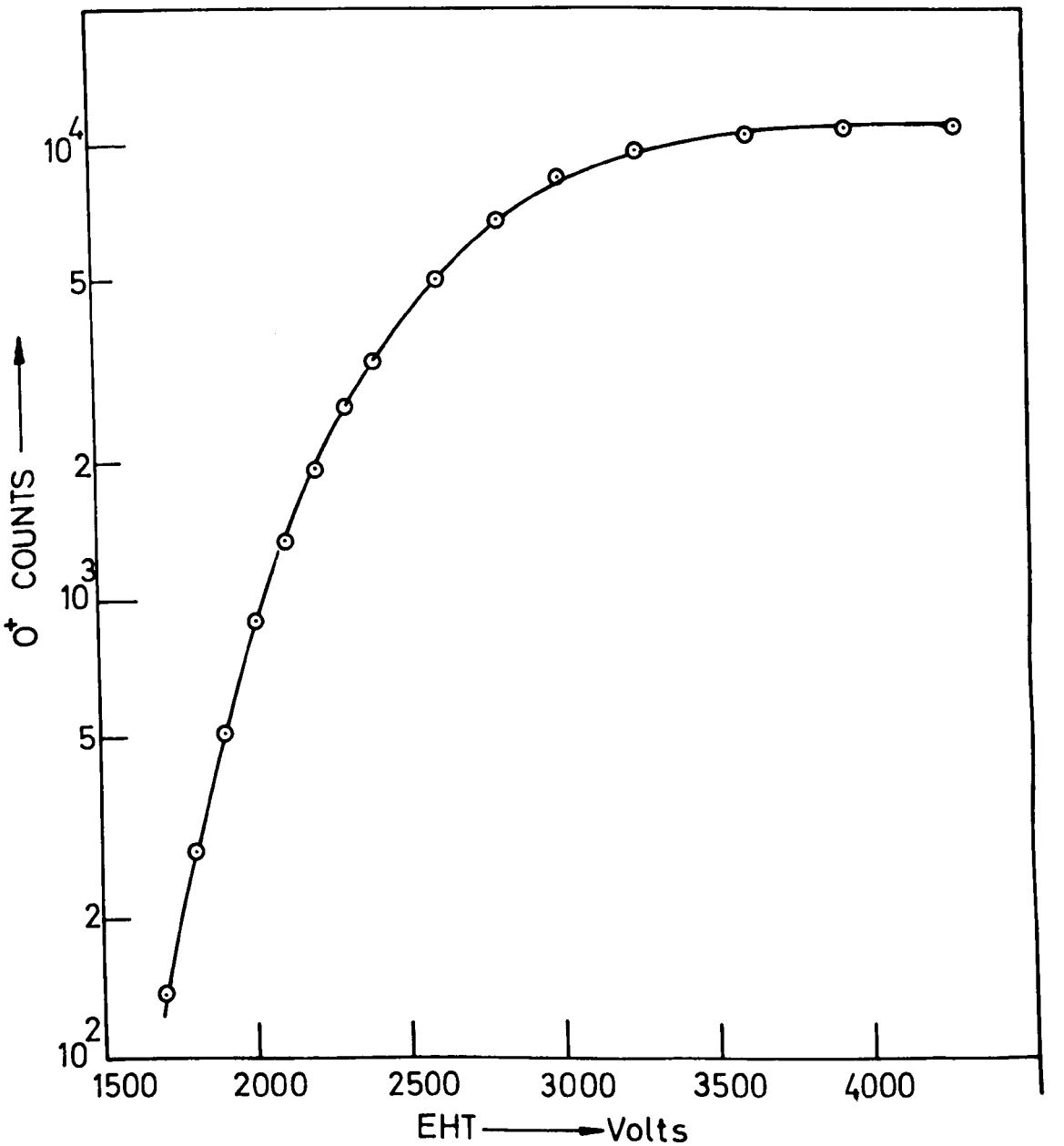
10^4
5
2
10^3
5
2
10^2
O^+ COUNTS
1500
2000
2500
3000
3500
4000
EHT ⟶ Volts

FIG. 4.9

rise time of the pulse to about 20 nanoseconds. The analytical expression relating the radius of curvature, length and inside diameter of the channel for a minimum "regenerative ion-feedback-electron-multiplication process" has been discussed by Evans[82a].

The efficiency of the channel multiplier for the detection of low energy charged particles depends first upon the probability that the incoming primary ion will produce one or more secondary electrons when it strikes the input end of the channel and secondly upon the probability that the initial secondary electron will result after multiplication in a saturated output pulse. No work has so far been reported on the dependence of the detection efficiency of the channel on the energy or the type of the incident particle. The measurement of low energy mono-energetic ion beams is difficult because of the inability to measure the very weak input flux that is necessary to avoid dead-time effects in the channel. No serious attempt was made to measure the efficiency in the present work since only the relative counts of O^{++} and O^{+} were required although by a crude estimate we can put the efficiency between 30 - 40%. It was assumed however that the detection efficiency was the same for O^{++} and O^{+} in the saturated mode of operation of the pulse. Figure 4.9 shows the count rate vs the potential difference across the channel for O^{+} measured at a scattering angle of 1^{o}, where it can be seen that saturation sets in at about 3.3 kV.

It was observed during the experiment that very high counting rates result in fatigue and temporary loss of efficiency in the channel made

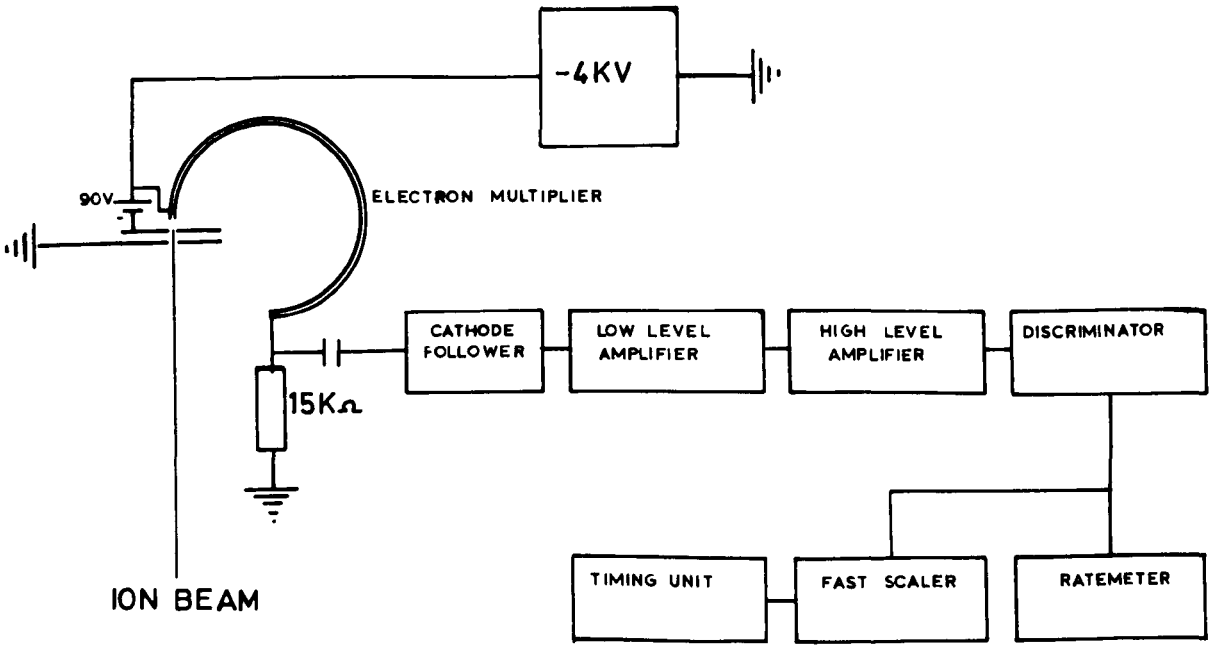
-4KV
90V
ELECTRON MULTIPLIER
CATHODE FOLLOWER
LOW LEVEL AMPLIFIER
HIGH LEVEL AMPLIFIER
DISCRIMINATOR
15KΩ
ION BEAM
TIMING UNIT
FAST SCALER
RATEMETER

FIG. 4.10

by Bendix and eventually after long use a permanent loss of 90% in the efficiency was observed. It is likely that the temporary loss of efficiency may be due to the physical adsorption of oxygen on the surface, whereas the permanent damage may be due to the chemical reaction between the surface and the oxygen ions which might raise the work function at the input end of the channel. The damaged multiplier was replaced by a similar multiplier made by Mullard and the same effect was observed. Namely the loss of efficiency after intensive use.

4.6.3 The counting system.

Figure 4.10 shows a block diagram of the system which consisted of the Harwell 2000 series cathode follower type 1635A (gain = $\frac{1}{2}$), the low level amplifier type 2024A (gain = 60), the high level amplifier type 2025B (gain = 150), a rate meter/integrater type 2101B and the six decade fast scaler type 2130. The overall gain of the system is thus 4500, which is such that in the saturation mode, the amplified pulses were 22 volts. The type 1 pulses (5 - 10 v negative for 200 nanoseconds) from the discriminator were fed in parallel to the ratemeter and the scaler which was controlled by the timing unit type 2041 - 2. The resolution time of the scaler is 100 nanoseconds which is of course offset by the duration of the type 1 pulse from the discriminator and the overall resolving time of the amplifying system which was 3 microseconds. The effect of the finite resolving time of the input circuit of the counting equipment is to give an observed count rate less than the true value. If n is the true count rate, N the observed count rate and t is

the resolution tiem, then

$$n = \frac{N}{1 - Nt}$$

since t 3 μsec, it was only necessary to correct the high counting rates according to the above equation.

4.7.1 The Vacuum System

The ion source described earlier requires a gas pressure of 0.1 mm of Hg while in the collision chamber a pressure of about 5×10^{-4} mm of Hg was maintained for the single collision conditions to prevail. To maintain such a high partial pressure in the ion source with the source gas introducing appreciable impurities in the collision chamber and to maintain sufficiently low background pressure in the analysis chamber, high pumping speeds were required. This was achieved by the pumping system shown in Figure 4.11. It consisted of two brass cylinders 13" in diameter and 18" long, each mounted on a baffle valve with a liquid air trap and a 9" oil diffusion pump with pumping speed of 900 lit/sec. The two cylinders were connected together by a rectangular manifold 3" x 10" in section and 12" long, which was placed between the gap of the electromagnet. The extensions of the poles of the electromagnet were introduced inside the vacuum system with O ring seals through the sides of this rectangular pipe. The experiment was mounted on the lid of the central portion. The two diffusion pumps produced a baffled pumping speed of about 800 lit/secs. This speed was such that when gas was introduced in the ion source at 0.1 mm of Hg, the background pressure

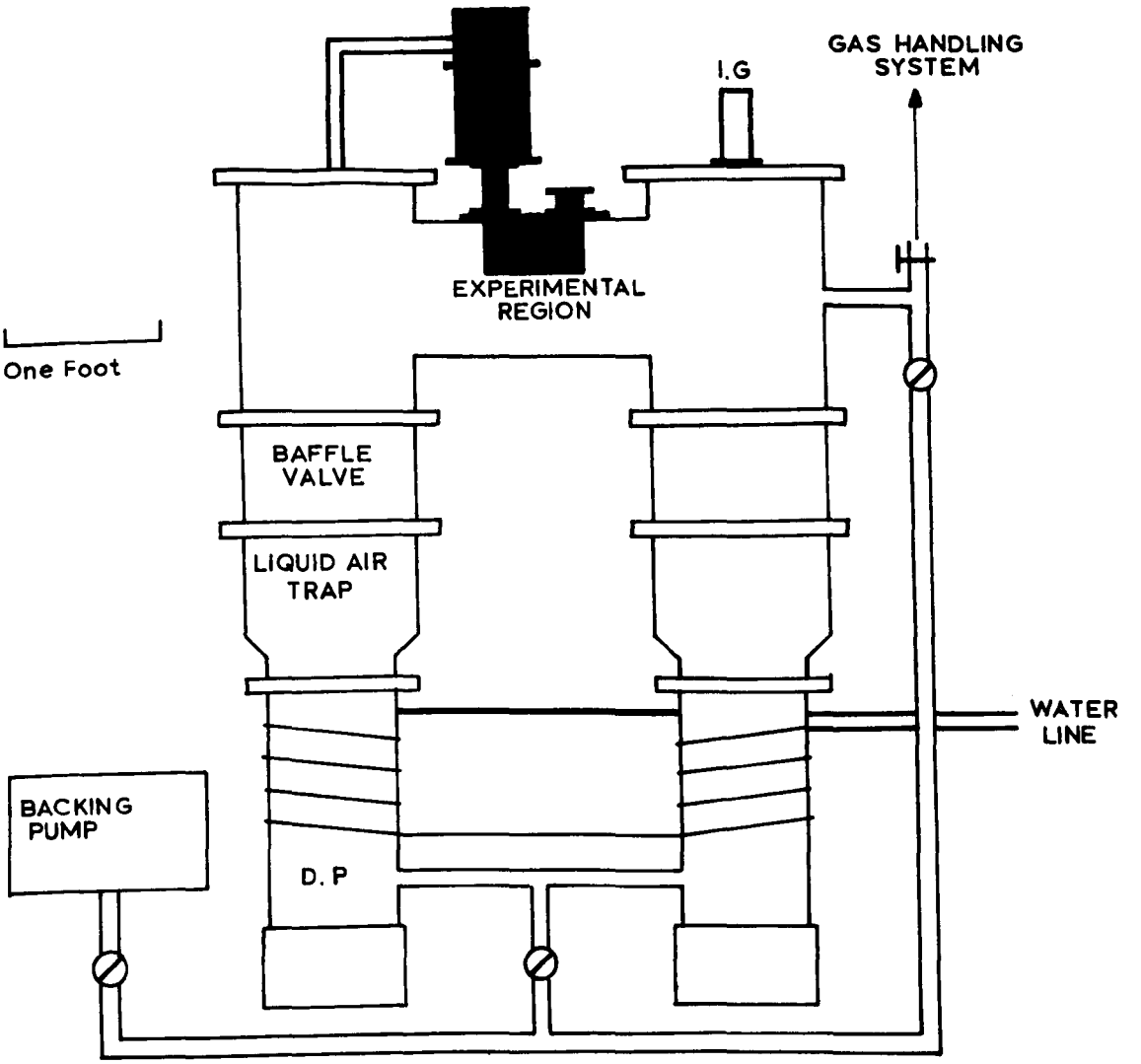
GAS HANDLING SYSTEM
I.G
EXPERIMENTAL REGION
One Foot
BAFFLE VALVE
LIQUID AIR TRAP
WATER LINE
BACKING PUMP
D. P

FIG. 4.

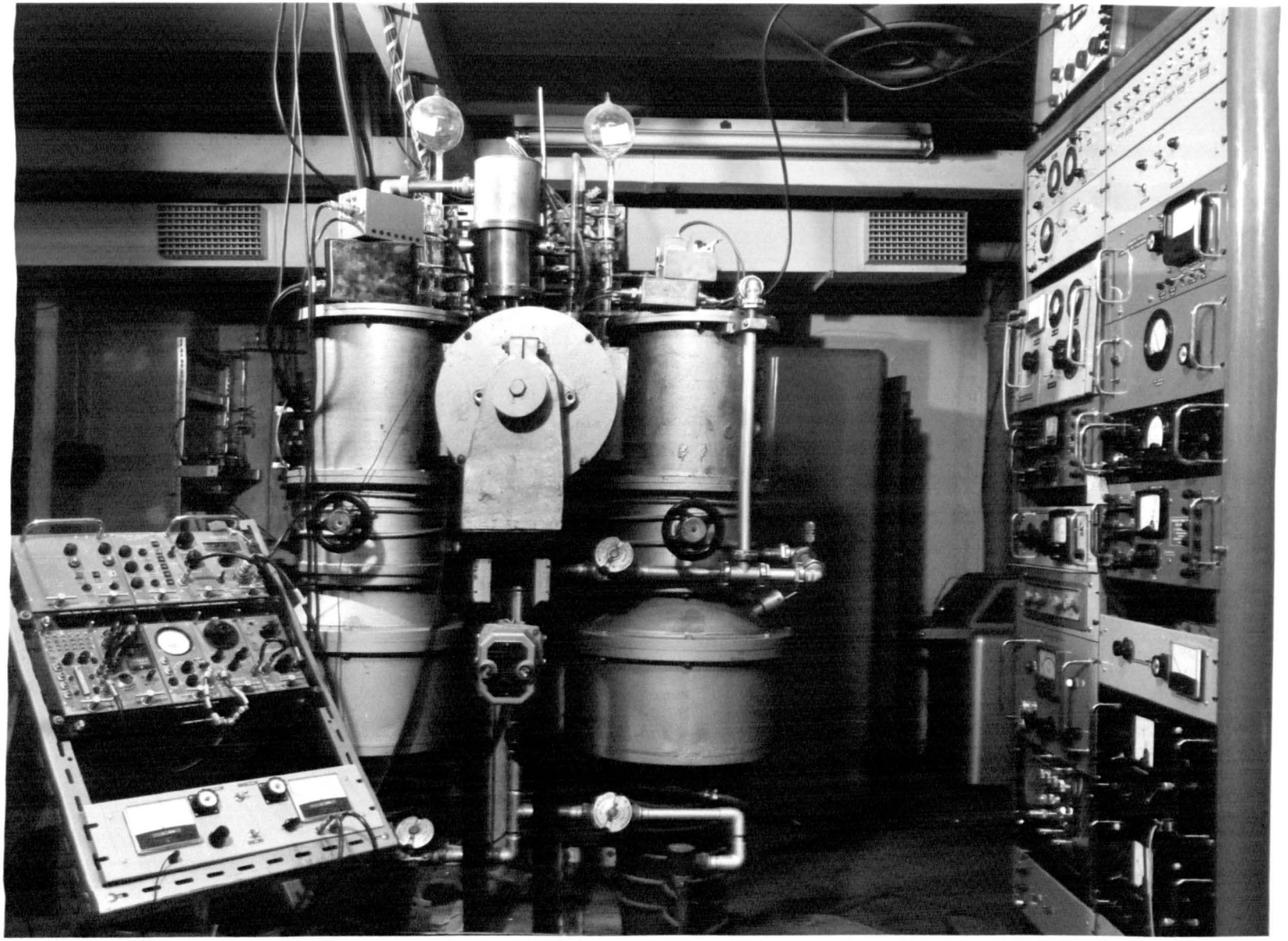

in the main vacuum chamber rose from 1×10^{-6} to 2×10^{-6} mm of Hg while in the collision chamber it increased from 5×10^{-6} to 6×10^{-6} mm of Hg. This was found to be adequate for the present experimental studies.

Spectrally pure gases for the ion source and collision chamber were supplied from 1 litre flasks through independent pyrex glass delivery systems, each consisting of a needle valve, liquid nitrogen trap, a pirani gauge for the ion source and an ionization gauge for the collision chamber pressure measurements. Each of the systems were provided with a by-pass line to the main vacuum chamber for initial evacuation. The pressure gauges were calibrated against a standard high sensitivity McLeod gauge.

CHAPTER V

EXPERIMENTAL MEASUREMENTS AND DISCUSSION OF THE RESULTS

5.1 Method of taking measurements

The vacuum system shown in Figure 4.11 was pumped for about six hours to obtain the lowest possible pressure in the system particularly in the collision chamber. Such a long pumping time was necessary since the volume enclosed by the collision chamber had to be evacuated through a long glass tube connected to the glass handling system by-passed to the main vacuum chamber. The ultimate pressure in the main system was then 8×10^{-7} while in the collision chamber it was $\sim 5 \times 10^{-6}$ mm of Hg. Before introducing carbon monoxide into the ion source to obtain O^{++} ions, the filament was degassed by increasing the current through it in steps of 1 amp. at an interval of $\sim$ 10 minutes until an emission current of <1 ma was obtained. The filament was then left on for about half an hour. This slow heating is necessary for the long-life of the filament. The ion source gas was then introduced through a needle valve so that the partial pressure in the source was $\sim 5 \times 10^{-2}$ mm of Hg. This resulted in an increase of background pressure to 3×10^{-6} mm of Hg. Due to the fast pumping speed the rise of pressure in the collision chamber was hardly detectable. Two Roband 500 volt stabilized supplies were used, one for the electron acceleration and the other for the ion extraction and analysis. The magnetic field for the ion source and the mass-

spectrometer was set to 1000 gauss. For the O^{++} ion, the necessary extraction and analysis voltage was therefore 350 which gives an initial energy of 700 eV to the ions. The focussing potential for the lens and the deflecting potential were respectively supplied by variable 400 volts and 100 volts stabilized supplies. These voltages were adjusted to obtain a maximum ion beam in the collision chamber. This current was monitored by the Faraday cage F placed above the aperture 6. The removal of the Faraday cage from the path allowed the beam to pass through the resolution holes (4,5) set along the axis of the beam. The beam was then monitored by the Faraday chamber T (Figure 4.1) when no potential difference was applied between the two electrodes of the electrostatic analyser. The beam measured at T was 3×10^{-12} amps and was 10% smaller than that measured at F.

The ions were deflected towards aperture 7 into the input end of the channel multiplier by applying a variable positive potential on the plane electrode with respect to the curved electrode which was grounded. The observed counting rate N measured by the multiplier in its saturation mode was 3×10^{5} counts/sec. The overall resolving time t of the detection system being 3μsec, the true counting rate n calculated from the equation

$$n = \frac{N}{1 - Nt} \qquad 5.1$$

is therefore 3×10^{6} ions/sec. Since the ion beam of 3×10^{-12} amp. corresponds to 9×10^{6} O^{++} ions/sec. the multiplier efficiency was therefore

$\sim$ 30%. The analysis potential was further increased to monitor the singly charged component which may have been present due to collisions with the background gas. This number was found to be negligibly small < 100 counts/sec compared to 3×10^6 counts/sec of the primary beam. The target gas (Ne or He) was then introduced through a needle valve, from a separate glass system which resulted in an increase of O^+ ions due to the partial charge transfer.

The angular data requires to demonstrate that the measured currents of O^+ at any angle θ are a linear function of the target gas pressure to insure that the pressure in the chamber is low enough that the scattered O^{++} and O^+ ions resulted from single collisions. This is particularly important for small angles since the path length is maximum, equal to the distance between the apertures 6 and 4. To find such a suitable range of the pressure, the resolution holes were set at an angle of 1^o and O^+ was measured as the pressure of the target gas was slowly increased. One such measurement for the reaction

$$O^{++} + He \longrightarrow O^+ + He^+ \qquad 5.2$$

obtained at the projectile energy of 1200 eV is shown in Figure 5.1 where it is seen that the growth of O^+ is linear up to a pressure of 1×10^{-3} mm of Hg. The arrow marks the termination of the single collision conditions. When the target gas pressure was kept too low i.e. $< 4 \times 10^{-4}$ mm of Hg the number of O^+ ions scattered through $\theta > 1^o$ were substantially small which resulted in a large statistical fluctuation in the count rate. The pressure in the collision chamber was therefore

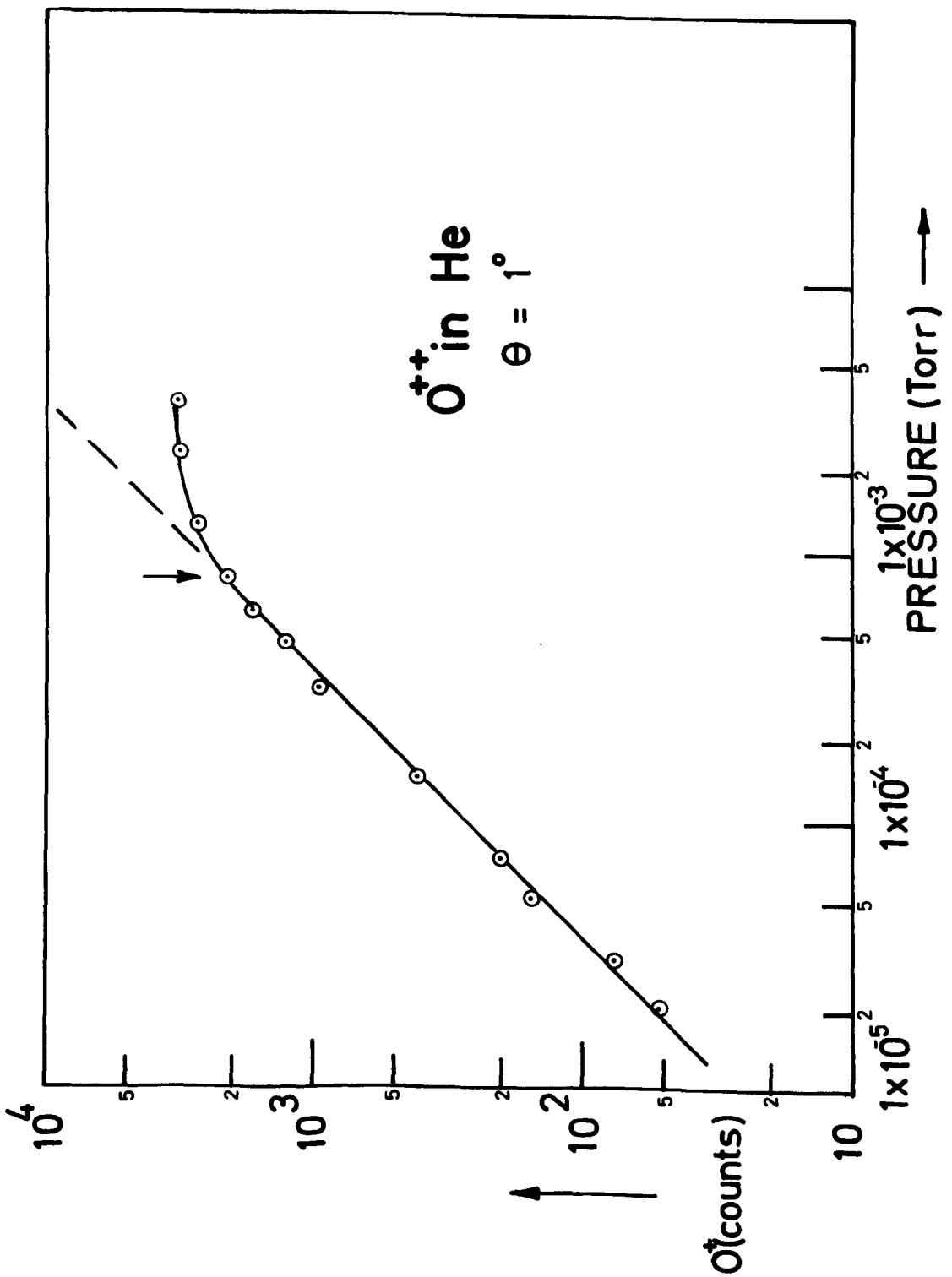
O^{++} in He
θ = 1°
O^{++}(counts)
10^4
10^3
10^2
10
1×10^{-5}
1×10^{-4}
1×10^{-3}
PRESSURE (Torr) ⟶

FIG. 5.1

kept at 8×10^{-4} mm of Hg. This pressure being 100 times larger than the background pressure, the scattered currents from the residual gases were negligibly small. However if the cross-sections for a similar process for the residual gas are larger than those of the reactions under study, then the number of O^{++} and O^{+} ions resulting from collisions with the residual gas must be subtracted from the corresponding ions obtained at the same angle due to the target gas. This correction was found to be very small 0.01%.

Another factor which must be taken into account is the collection efficiency of the aperture 7. If I_o is the number of particles of a particular charge state emerging out of the resolution system (4,5) and I is the number passing through 7 and entering the input end of the multiplier, then we define collection efficiency by the ratio $\frac{I}{I_o}$ which should be 1. This was investigated by measuring the count rate of the species as a function of the electrostatic analyzer potential. The peaks due to individual components must have a flat top for $\frac{I}{I_o} = 1$. One such measurement for the process 5.2 is shown in Figure 5.2. The flat tops of the peaks of O^{++} and O^{+} are evident. Since O^{++} ions do not lose their mechanical kinetic energy in a charge transfer process, the O^{+} peaks occur at twice the analysis voltage for the O^{++} peaks.

The relative counting efficiency for the two species namely O^{++} and O^{+} is also important. The measurement of the efficiency for O^{+} ions was not possible in the present set-up, however it was found that the pulse height distributions for O^{++} and O^{+} were different if the multiplier

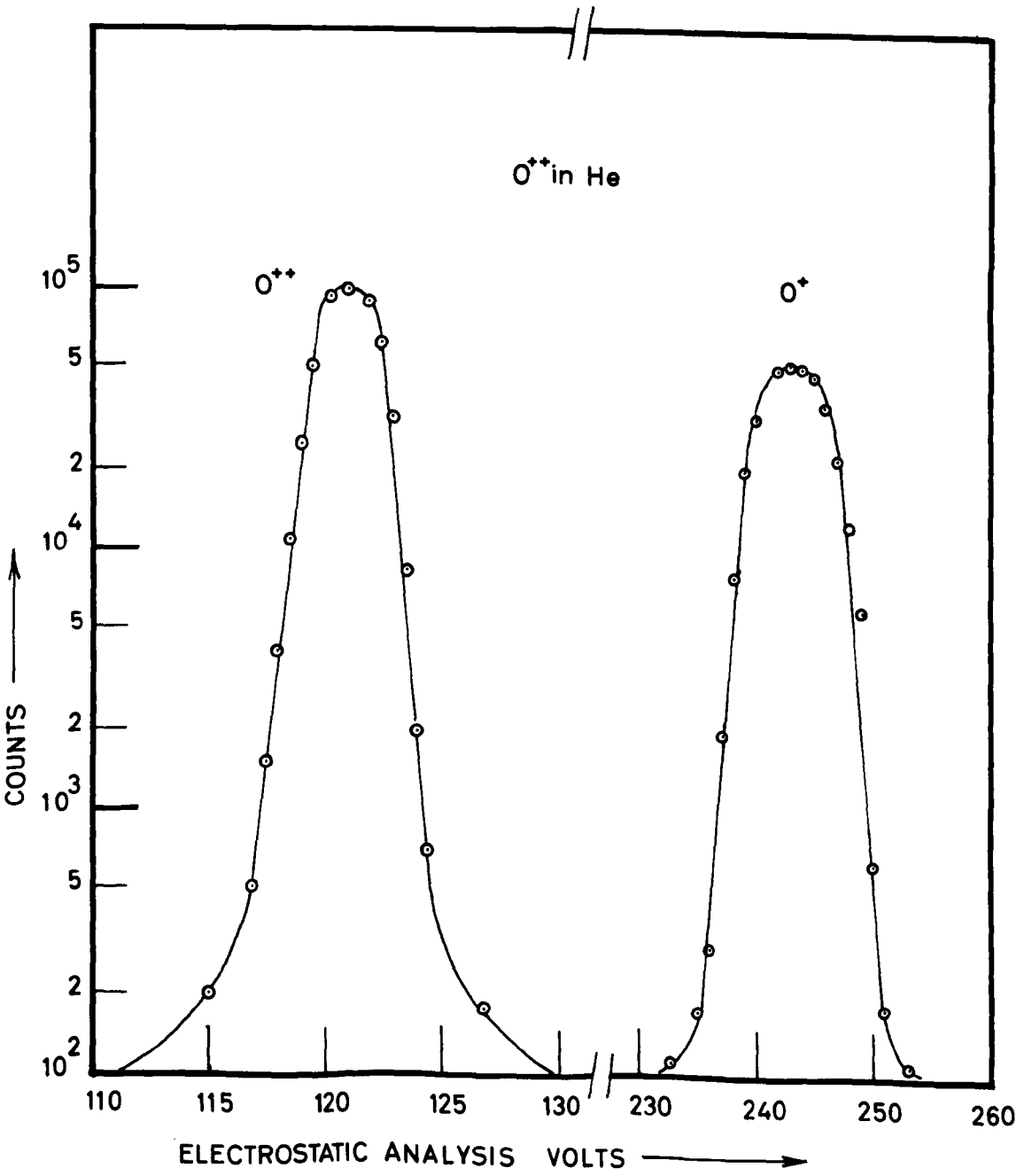
O++ in He
O++
O+
COUNTS
10^5
5
2
10^4
5
2
10^3
5
2
10^2
110
115
120
125
130
230
240
250
260
ELECTROSTATIC ANALYSIS VOLTS

FIG.5.2

was not operated in the saturated pulse mode for both the charge states. To achieve the saturation mode, the ratio O^+/O^{++} was studied as a function of the discrimator voltage at different potential differences across the multiplier. It is obvious that under saturation conditions for O^{++} and O^+, the above ratio is invariant over a certain range of the discriminator voltage. A sharp cut-off was observed for both the components at a discriminator setting of 22 volts.

The angular data was taken for every 0.002" forward movement of the rod R of the right hand rotary shaft seal (Figure 4.7a). The reverse run could not be taken due to the lag in the thread. The position of the rod was noted from a micrometer consisting of a circular disc containing 25 divisions and a fixed scale in which 1" was divided into 40 equal parts.

5.2 Relation between ρ and θ

The differential data obtained is meaningless for the present study unless the probability P, for an angle θ is expressed in terms of the corresponding impact parameter ρ. This requires that the value of the impact parameter for each angle must be known. Unfortunately for the present processes no such calculations are available; however it was pointed out by Massey et al[83] that a classical calculation is valid in so far as the trajectories of the particles are concerned. Such a relationship between ρ and θ was obtained by applying classical mechanics on the following lines.

In the centre of mass system of coordinates, the collision is equivalent to the motion of an imaginary body of mass μ, given by

$$\mu = \frac{M_1 M_2}{M_1 + M_2}$$

where M_1 and M_2 are respectively the masses of the projectile and the target, around a fixed centre of force O as shown in Figure 5.3. If ρ is the impact parameter, v_r the relative velocity and (r,ϕ) the polar coordinates of the particle at a given instant, then the angular momentum conservation about O and the energy conservation give respectively

$$\mu\rho v_r = \mu r^2 \dot{\phi} \qquad 5.4$$

and

$$\tfrac{1}{2}\mu v_r^2 = \tfrac{1}{2}\mu(\dot{r}^2 + r^2\dot{\phi}^2) + V(r) \qquad 5.5$$

where $V(r)$ is the interaction potential energy. Eliminating ϕ from 5.4 and 5.5, we obtain

$$\frac{dr}{dt} = \pm v_r \left[1 - \frac{\rho^2}{r^2} - \frac{V(r)}{\frac{1}{2}\mu v_r^2}\right]^{\frac{1}{2}} \qquad 5.6$$

and

$$\frac{dr}{d\phi} = \frac{dr/dt}{d\phi/dt} = \pm \frac{r^2}{\rho}\left(1 - \frac{\rho^2}{r^2} - \frac{V(r)}{\frac{1}{2}\mu v_r^2}\right)^{\frac{1}{2}} \qquad 5.7$$

the negative sign applies to the incoming branch of the trajectory and the positive to the outgoing branch. The distance of the closest approach r_c is the largest real root of

$$1 - \frac{V(r_c)}{\frac{1}{2}\mu v_r^2} - \frac{\rho^2}{r_c^2} = 0 \qquad 5.8$$

and the corresponding polar angle ϕ_m is then given by

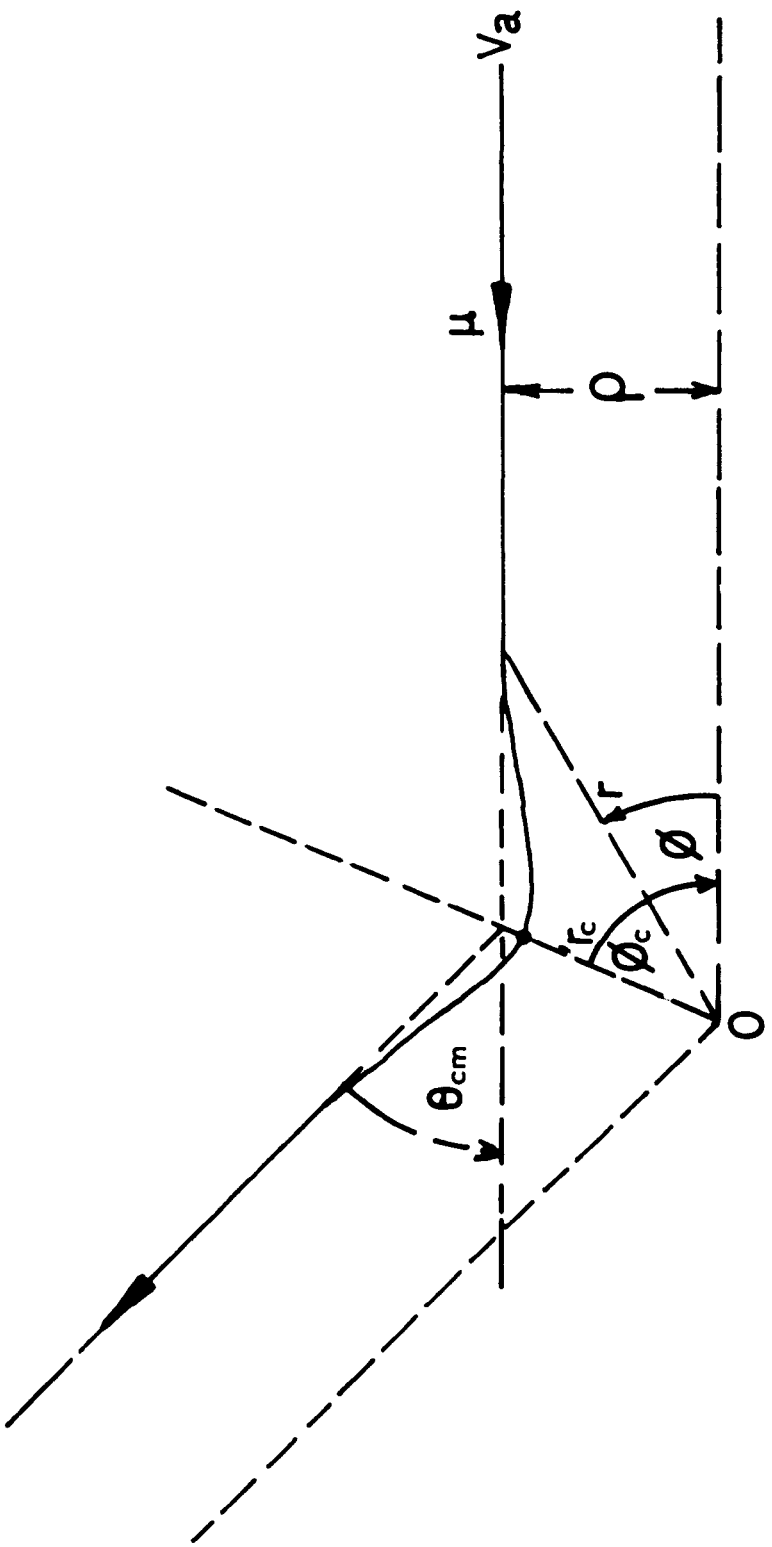

FIG. 5.3

$$\phi_m = -\rho \int_{\infty}^{r_c} \frac{dr}{r^2 \left(1 - V(r)/\frac{1}{2}\mu v_r^2 - \rho^2/r^2\right)^{\frac{1}{2}}} \qquad 5.9$$

Since the centre of mass trajectories are symmetrical about the line of closest approach, an examination of Figure 5.3 shows that the angular deflection θ_c in the centre of the mass system is related to ϕ_m by

$$\theta_c = \pi - 2\phi_m \qquad 5.10$$

therefore

$$\theta_c = \pi - 2\rho \int_{r_c}^{\infty} \frac{dr}{r^2 \left(1 - V(r)/\frac{1}{2}\mu v_r^2 - \rho^2/r^2\right)^{\frac{1}{2}}} \qquad 5.11$$

The deflection θ in the laboratory coordinates may then be determined from the relation,

$$\tan\theta = \frac{M_2 \sin\theta_c}{M_1 + M_2 \cos\theta_c} \qquad 5.12$$

Writing 5.11 in the form

$$\theta_c = \pi - 2\rho I \qquad 5.13$$

where

$$I = \int_{r_c}^{\infty} \frac{dr}{r^2 \left(1 - V(r)/\frac{1}{2}\mu v_r^2 - \rho^2/r^2\right)^{\frac{1}{2}}} \qquad 5.14$$

for a known potential function V(r), the difficulty in the numerical

evaluation of θ_c arises from the pole at r_c in the integral I which can be avoided by applying a method due to Bates, Cook and Smith[84]. Changing the variable to

$$x = \frac{r_c}{r}$$

$$I = \frac{1}{r_c} \int_0^1 f(x)(1 - x^2)^{-\frac{1}{2}} \, dx \qquad 5.15$$

where

$$f(x) = (1 - x^2)^{\frac{1}{2}} \, g(x)$$

$$g(x) = \left(1 - \frac{V(\frac{r_c}{x})}{E} - \frac{\rho^2 x^2}{r_c^2}\right)^{-\frac{1}{2}} \qquad 5.16$$

The solution of 5.15 is

$$I = \frac{\pi}{6r_c}\left[\cos\frac{5\pi}{12}\, g(\cos\frac{\pi}{12}) + \cos\frac{\pi}{4}\, g(\cos\frac{\pi}{4}) + \cos\frac{\pi}{12}\, g(\cos\frac{5\pi}{12})\right] \qquad 5.17$$

The above equation was solved on a digital computer, first using V(r) as the well-known ion-induced dipole polarization force,

$$V(r) = -\frac{\alpha \varepsilon^2}{2 r^4} \qquad 5.18$$

where α is the dipole polarizability of the target atom and ε is the charge on the projectile. However for small impact parameters, the long range inverse sixth power Van der Waals force (induced pole-induced dipole interaction)

$$V_w(r) = -\frac{c}{r^6} \qquad 5.19$$

may have an appreciable correction to the deflection Θ for a given ρ. The constant c in 5.19 can be evaluated from the knowledge of the eigen values of the eigenfunctions and the electric dipole oscillator strength, but for the present calculations an approximate expression

$$c = \frac{3}{2} \frac{I_1 I_2}{I_1+I_2} \alpha_1 \alpha_2 \qquad 5.20$$

due to London[85] was used. Here α_1, α_2 are respectively the dipole polarizabilities of the projectile and target. I_1, I_2 are the corresponding ionization potentials. The values of α_1 and α_2 were obtained from the table compiled by Dalgarno[86].

The values of the polarizabilities and the ionization potentials for the reactants (O^{++} + Ne) and (O^{++} + He) are given in the following table.

	Polarizability	Ionization potential
O^{++}	0.30	54.886
Ne	0.406	21.559
He	0.206	24.581

Figure 5.4 shows the result of the calculations for (O^{++} + Ne) for an impact energy of 1200 eV; curve I is due to the inverse fourth power field only, and II is due to the combined inverse fourth and sixth power fields given by 5.18 and 5.19. It is seen that the correction at $\rho = 1.5\ a_o$ is about 60% and is indeed considerable within the range of the present experimental study viz. $\rho < 3\ a_o$.

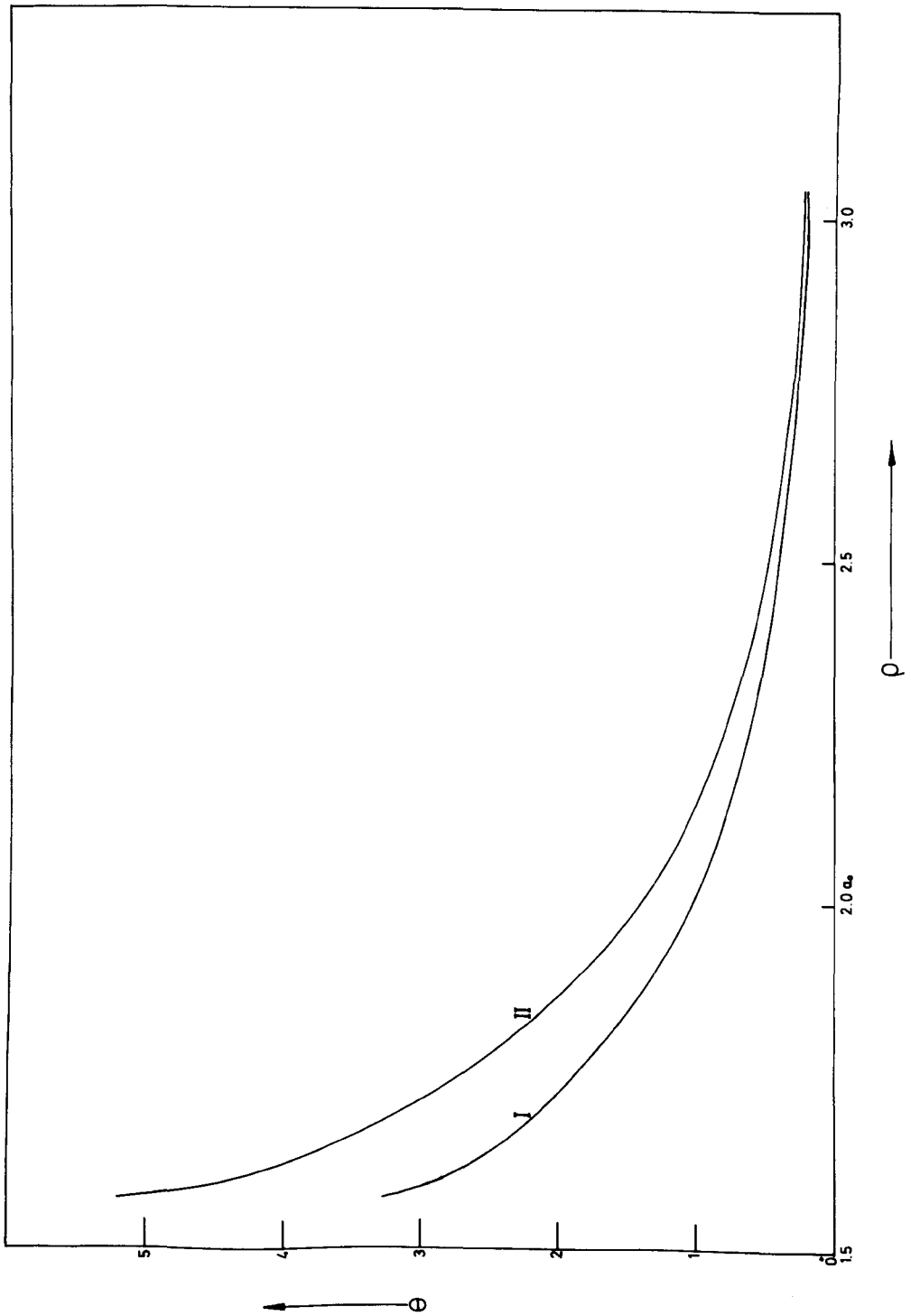

FIG. 5.

A reservation due to quantum mechanics must be placed on these results since the impact parameter is a classical concept and is not measurable everywhere. The uncertainty principle sets an upper limit to the classical validity of its measurements. For scattering due to an impact parameter ρ, there is an uncertainty in the scattering angle given by,

$$\text{Uncertainty of position x Uncertainty of momentum}$$
$$= \rho \cdot Mv\, \delta\theta = \frac{h}{2\pi} \qquad 5.21$$

where the uncertainty of position is taken as the entire impact parameter, and uncertainty of momentum is taken as the entire change $Mv \cdot \delta\theta$ in momentum of the scattered particle. The impact parameter ρ is immeasurable if

$$\delta\theta \sim \theta$$

Thus the uncertainty principle limit is

$$\rho_c \theta_c = \frac{h}{2\pi Mv} \qquad 5.22$$

In this equation 'c' refers to the values at the classical limit. The angle θ decreases rapidly with increasing ρ, so that the product $\rho\theta$ also decreases and 5.22 represents an upper limit on the validity of the measurement of ρ. For O^{++}, this limit is given by

$$(\rho_c \theta_c)_{1200} = 0.0355 \qquad 5.23$$

$$(\rho_c \theta_c)_{2600} = 0.025 \qquad 5.24$$

where ρ_c is in atomic units and θ_c in degrees. From the computed values, the products in 5.23 and 5.24 correspond respectively to $\rho_c = 5.6$ and $5\ a_o$ when the corresponding θ is $\sim 0.001^o$. It would appear therefore, that the range of the present data does not violate the quantum mechanical limitations.

5.3 Results and Discussion

The experimental results obtained by the method described in section 5.1 and reduced in terms of the impact parameter by the classical calculations of section 5.2 for the process

$$O^{++} + Ne \longrightarrow O^{+} + Ne^{+} \qquad 5.25$$

are displayed in Figure 5.5 and 5.6 for the impact energies 1200 eV and 2600 eV respectively. Similar data for the process

$$O^{++} + He \longrightarrow O^{+} + He^{+} \qquad 5.26$$

is shown in Figure 5.7 which was only taken at a single energy of 1200 eV.

Unfortunately the theoretical calculations for the above processes whether based on the Landau-Zener theory or on the semi-classical impact parameter treatment are not available at present due mainly to the inability to assign quantum orbitals to such complex systems. It isnot possible therefore, to discuss these results quantitatively, however it is possible to deduce qualitative information regarding the process which leads to the charge transfer transitions for these reactions.

The comparison of the data, shown in Figure 5.5 taken for an impact

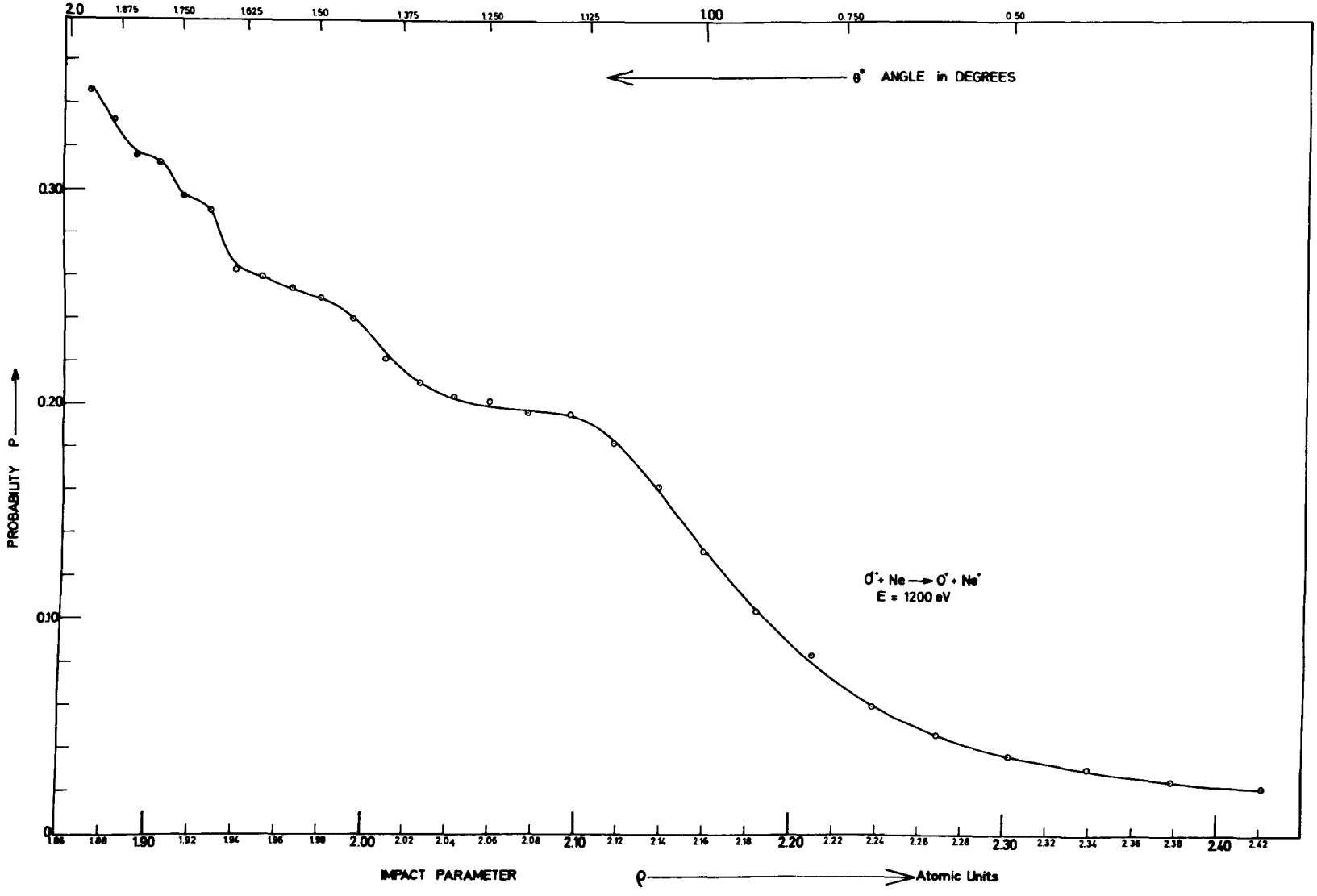
2.0
1.875
1.750
1.625
1.50
1.375
1.250
1.125
1.00
0.750
0.50
θ° ANGLE in DEGREES
PROBABILITY P
0.30
0.20
0.10
0
O⁺ + Ne → O⁺ + Ne⁺
E = 1200 eV
1.86
1.88
1.90
1.92
1.94
1.96
1.98
2.00
2.02
2.04
2.06
2.08
2.10
2.12
2.14
2.16
2.18
2.20
2.22
2.24
2.26
2.28
2.30
2.32
2.34
2.36
2.38
2.40
2.42
IMPACT PARAMETER
ρ
Atomic Units

FIG. 5.5

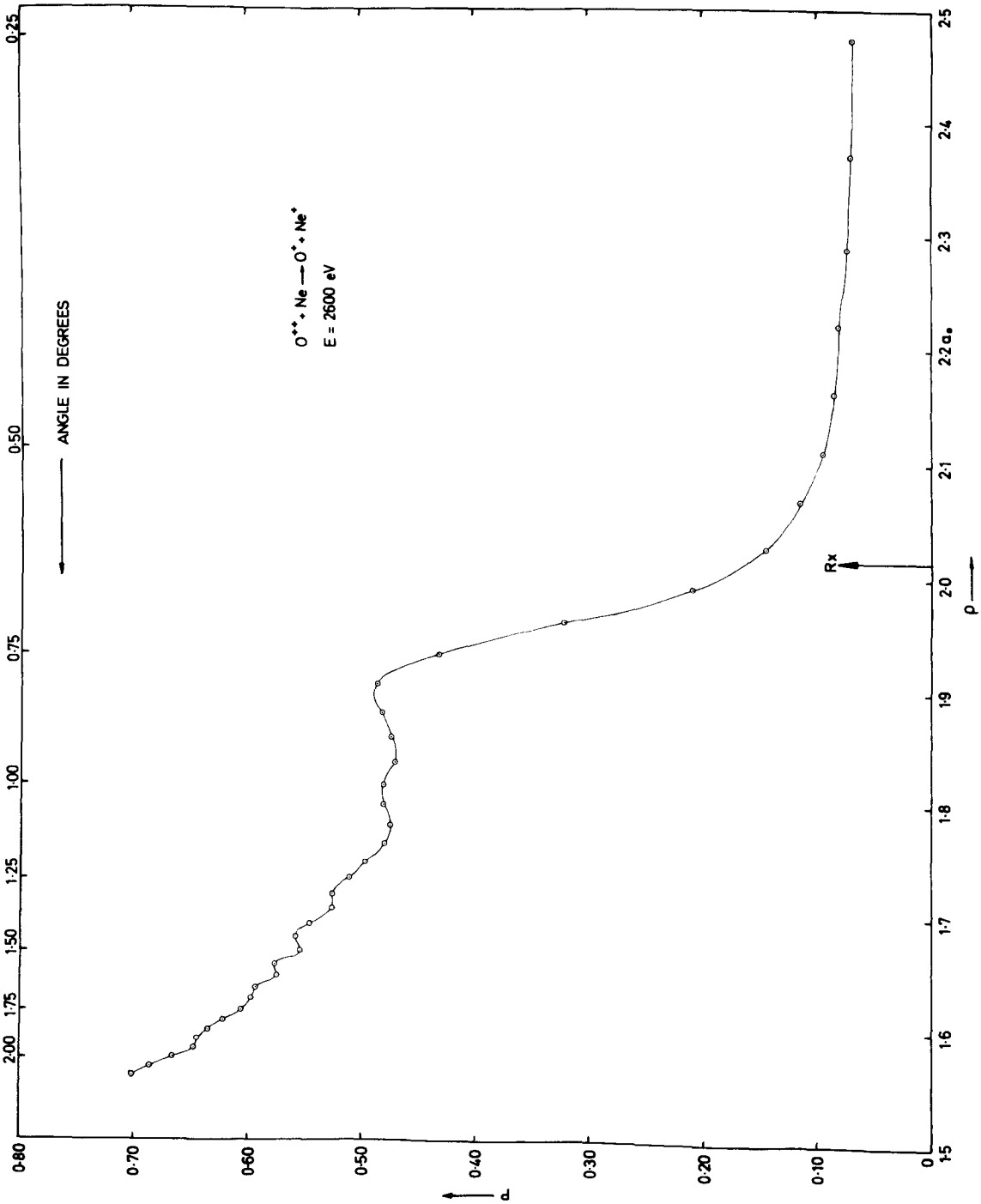
ANGLE IN DEGREES
$O^{++} + Ne \rightarrow O^{+} + Ne^{+}$
E = 2600 eV
Rx
P
ρ
0·80
0·70
0·60
0·50
0·40
0·30
0·20
0·10
0
0·25
0·50
0·75
1·00
1·25
1·50
1·75
2·00
1·5
1·6
1·7
1·8
1·9
2·0
2·1
2·2 a_0
2·3
2·4
2·5

FIG.5.6

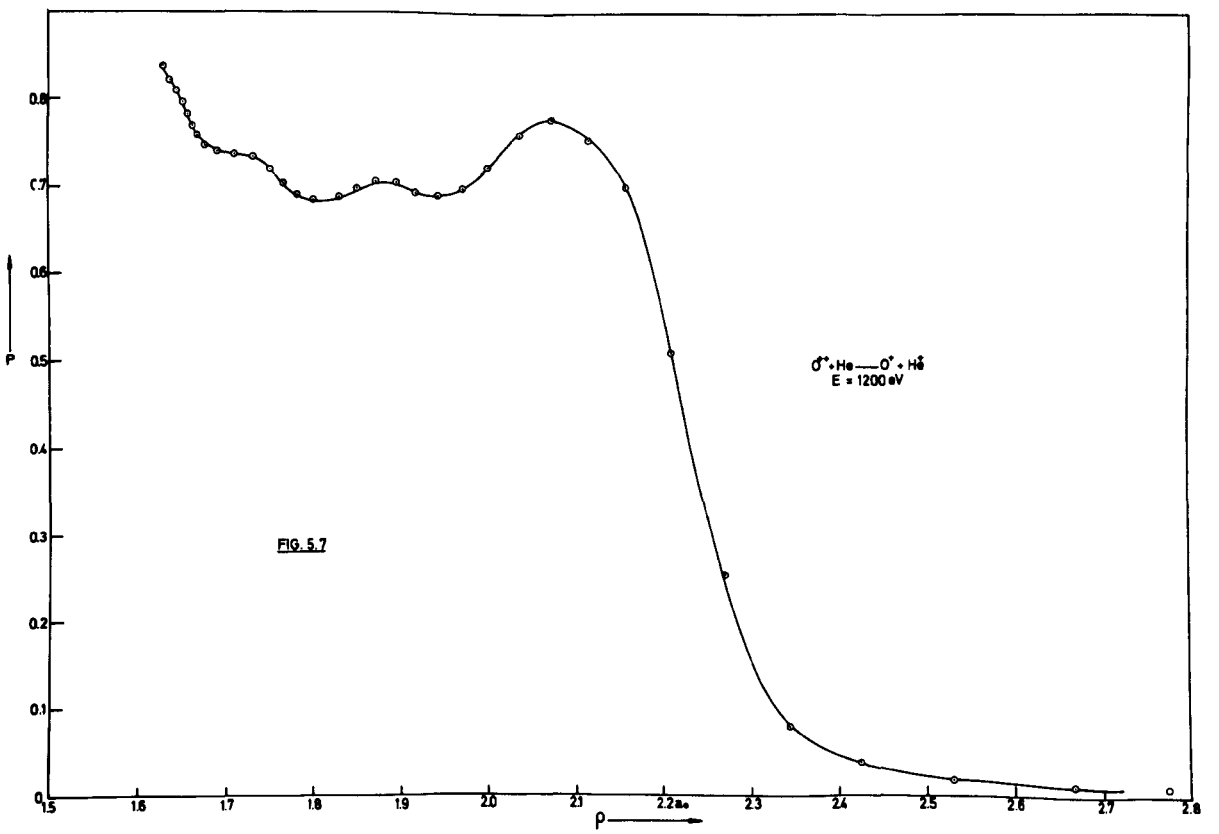
P
0.8
0.7
0.6
0.5
0.4
0.3
0.2
0.1
0
1.5
1.6
1.7
1.8
1.9
2.0
2.1
2.2a₀
2.3
2.4
2.5
2.6
2.7
2.8
ρ
O⁺+He——O⁺+He
E = 1200 eV

FIG. 5.7

energy of 1200 eV with that shown in Figure 5.6 for 2600 eV, reveal a striking difference. For example, the transition probability for 1200 eV is an oscillating function of the impact parameter. The flat portion of the curve can of course be attributed to the poor angular resolution of the instrument. It is not impossible that with improved resolution the oscillations would go down to zero for the flat part of the curve. Referring back to Bates, Smith and Johnston's[7a] numerical calculations for the process

$$Be^{2+} + H \longrightarrow Be^{+} + H^{+} \qquad 5.27$$

Figure 2.9 shows the behaviour of the transition probability as a function of the impact parameter for different impact energies of $10^{2.75}$ eV, $10^{2.75}$, $10^{3.50}$ and $10^{4.50}$ eV. The present data of Figure 5.5 shows a remarkable similarity with the Bates calculation for E = $10^{2.75}$ eV. Here the amplitude of the oscillations of the transition probability grows from 0.30 at large impact parameters to 1 at small parameter. It may be pointed out that these results are also similar to the Rapp and Francis calculations of the simple two state approximation. In Rapp and Francis case, as shown in equation 2.36 and Figure 2.5, the transition probability is a product of the $sech^2$ function and the corresponding transition probability for the symmetric case. At low energies, the product of the two leads to very small amplitudes of the oscillations, which is the same as that shown in Figure 2.9 (for E = $10^{2.25}$) due to Bates. At intermediate energies the oscillations grow in size and attain a maximum amplitude for small impact parameter. Qualitatively the present result

at 1200 eV corresponds to the product of the $sech^2$ function represented by C and Psy of Figure 2.5. Now Bates calculations do not take into account the position of the pseudo-crossing point and the oscillations for $E = 10^{2.75}$ grow independent of the impact parameter corresponding to the distance of the closest approach, but it is evident from Figure 5.5 that the oscillations in P are occurring well away from $R_x = 2.0\ a_o$. Since the number of particles scattered through angles $>2^o$ is very small, it is therefore evident that at this energy most of the contribution to the charge transfer comes from the impact parameter $> 2\ a_o$. The Landau-Zener theory is therefore not a good description of the process.

On the other hand, the data for the same process for E = 2600, it is seen in Figure 5.6 that there is a sharp increase in the transition probability at $\rho = 2.1\ a_o$, the impact parameter for which the distance of closest approach corresponds to the internuclear separation at the crossing point. The transitions at the crossing point in this case dominate compared to those for $\rho > 2.1\ a_o$. However according to the Landau-Zener theory the transition probability would achieve a sharp maximum at this ρ, and should remain constant over the whole range of $\rho < 2\ a_o$. It is evident from Figure 5.6 that this is not the case, in fact P function has a structure (oscillations) for $\rho < 2\ a_o$, and that it is a continuously increasing function of ρ. It would appear that at this impact energy the Landau-Zener approximation is applicable, however there is a better agreement between these results and the

62a

calculations of Ellison and Borowitz. Instead of assigning a constant

value β to the matrix elements $h_{nm}(Z)$ and $h_{mm}(Z)$ and $h_{nn}(Z) - h_{mm}(Z) = \alpha(Z - Z_c)$ (equations 2.58 and 2.59), they assume that

$$h_{nm} = h_{mn} = \beta \exp\left\{-\gamma(R - R_x)\right\}$$

and

$$h_{mm} - h_{nn} = \Delta E\left[1 - \exp - \left\{\gamma(R - R_x)\right\}\right]$$

where γ is an additional constant and R_x is given by

$$R_x = \frac{27.2\ (n-1)}{E}\ a_o$$

n being the charge on the projectile.

Their result for the process

$$H^- + Li^+ \longrightarrow H + Li$$

shown in Figure 5.9, calculated for an impact energy of 12 eV is that there is a sharp increase in P at R_x, followed by small oscillations about the Landau-Zener mean value of 0.82. In form the results at 2600 eV correspond to these predictions.

We assume, therefore, that at such energies where $R_x \gtrsim R_c$ where R_c is the distance of closest approach, as is the case in Figure 5.5, two state approximation or Bates numerical analysis is a good description of the way the transitions take place. Here in this case for most of the projectiles, the distance of closest approach is greater than R_x and the Landau-Zener theory therefore inapplicable. On the other hand for impact energies at which most of the projectiles come closer than R_x, the transitions by way of the pseudo-crossing of the potential energy curves dominate. In this case then Ellison and Borowitz'

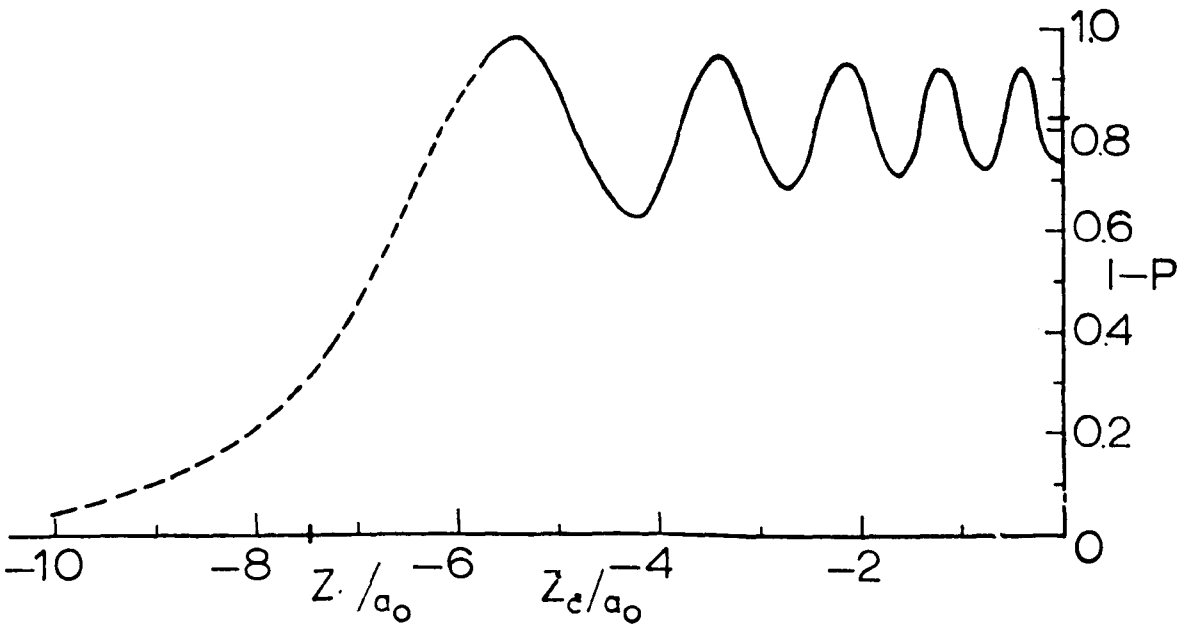

FIG. 5.9

equal exponential model should be applied for the computation of the total charge transfer cross-sections.

In the case of the process 5.26, most of the O^{++} come closer than R_x = 2.50 at 1200 eV, the behaviour is therefore, as shown in Figure 5.7 similar to that for the process 5.25 at 2600 eV, as expected on the Ellison-Borowitz equal exponential model i.e. a sharp increase in the probability for an impact parameter which corresponds to the $R_c = R_x$, followed by an oscillatory behaviour. It seems that the behaviour of the process 5.26 similar to that of 5.25 at 1200 eV, will be obtainable at impact energies perhaps $\ll$600 eV, which was not possible in the present arrangement since the primary ion beam had to be retarded after the analysis which would have entailed a necessary loss of the ion beam intensity. It was not tried to study this reaction at 2600 eV, for the same reason that $R_c < R_x$ for the range of the experiment.

An important conclusion that can be drawn from the (O^{++}, Ne) data at two impact energies is that it lends information as to whether the transitions are taking place via pseudo-crossing of the potential energy curves i.e. an oscillatory pattern with increasing amplitude will correspond to no influence due to the potential energy curves and a steep rise will mean the domination of the pseudo-crossing. Study of the differential data can therefore be applied to a number of processes in which it is believed that the curve-crossing influences the cross-sections. One of such processes is

$$Ne^+ + Ar \longrightarrow Ne + Ar^+ + (5.8\ eV) \qquad 5.28$$

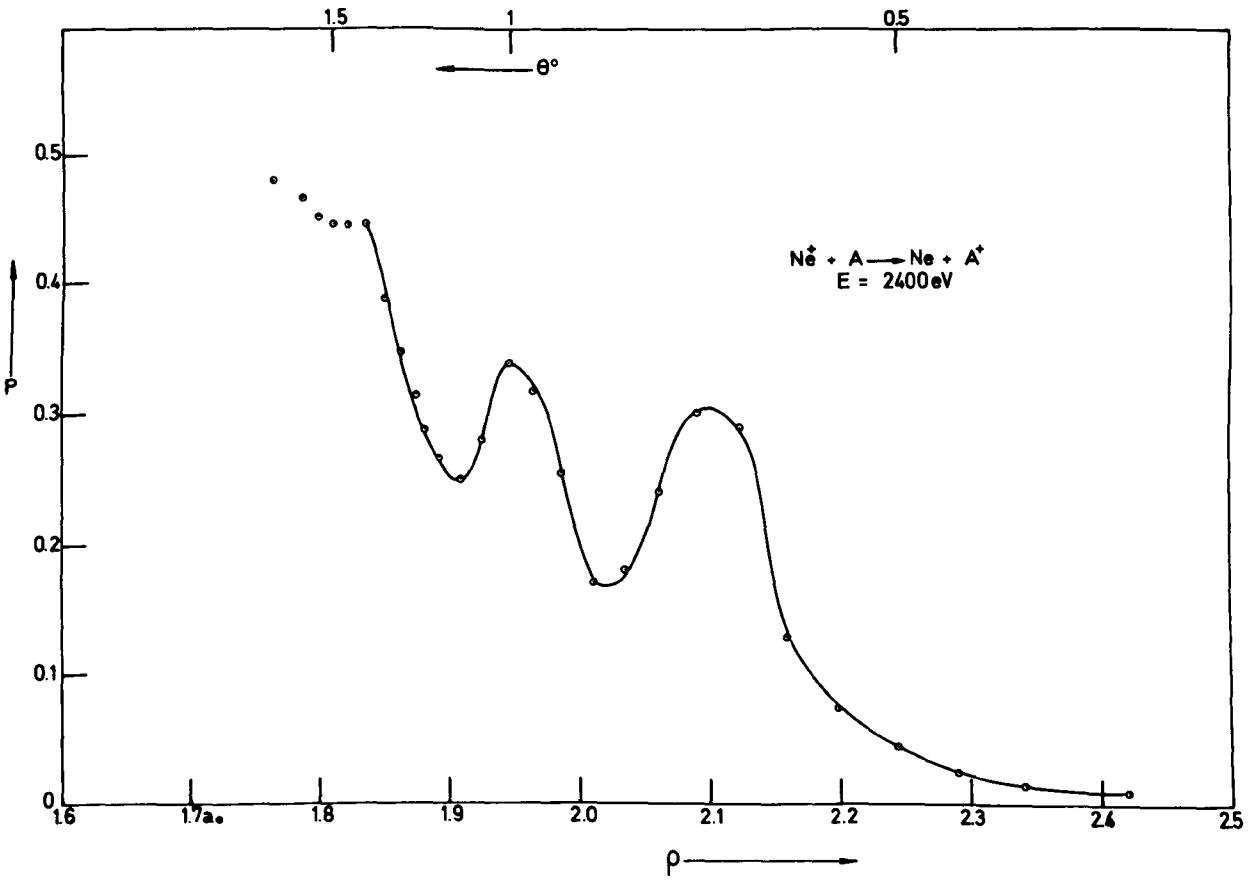
1.5
1
0.5
θ°
0.5
0.4
0.3
0.2
0.1
0
P
Ne⁺ + A → Ne + A⁺
E = 2400eV
1.6
1.7a₀
1.8
1.9
2.0
2.1
2.2
2.3
2.4
2.5
ρ

FIG. 5.8

for which charge transfer cross-sections have been observed by Gilbody and Hasted[20], and by Bohme et al[87] to be large within the adiabatic region. By introducing a modification in the present experimental set-up it was possible to take differential data for the above reaction. The fast collision products in this reaction are Ne^+ and Ne^o and by setting the input end of the channel multiplier in line with the resolution apertures (4,5) of Figure 4.7, the total current $I = Ne^+ + Ne^o$ can be measured when no deflector potential is applied to the electrostatic analyser, and I_o the neutral component by deflecting the Ne^+ away with the analyser. The fraction $\frac{I_o}{I}$, therefore gives the charge transfer probability. No attempt was made to compare the detection efficiency of the multiplier for Ne^+ and Ne^o. The primary Ne^+ beam was substantially large $\sim$ 10 times larger than O^{++}, the resolution of the instrument was improved to 0.02^o. The reduced data taken at the impact energy of 2400 eV is shown in Figure 5.8. The oscillations indicate that there is no observable influence due to the curve crossing. The reason for this is the limitations of the experimental set-up in which, due to the beam intensity problems, observation could not be extended to angles $> 2.5^o$. Within the present range of $\theta \sim 2^o$, the smallest impact parameter is $\approx 1.7\ a_o$ corresponding to a distance of closest approach of $1.6\ a_o$ whereas the crossing point is believed to be $\sim 1.4\ a_o$. In the measurements of the total cross-sections the curve crossing can influence at all energies since total cross-sections are built up from contributions of impact parameters ranging from 0 to ∞. At low energies

therefore small impact parameters may give rise to $R_c \sim R_x$ whereas for differential measurements, a particular impact parameter and R_c are chosen for a particular angle and within the angular range of the experiment, R_c may be greater than R_x for all angles. ($Ne^+ + Ar$) studies should therefore be carried out at such energies that within the angular range $R_c \sim R_x = 1.4\ a_o$. This energy can of course be calculated from the classical equation 5.8. Unfortunately in this experimental arrangement the maximum energy range is 2.5 keV, which is too small for the effect of the curve crossing to be detectable by differential measurements but a similar experiment conducted at 7KeV may decide whether the cross-sections for the process 5.28 are influenced by the curve crossing.

ACKNOWLEDGMENTS

The author avails himself of the opportunity to express his thanks to Professor Sir Harrie Massey F.R.S. for his continued interest in this work, and is indebted to Dr. J.B. Hasted for his patient guidance and supervision. Helpful discussions with the members of Group 7, particularly Dr. D.K. Bohme are acknowledged.

Thanks are due to the Pakistan Atomic Energy Commission and The British Council for the award of the Colombo Plan Fellowship without which this work could not have been undertaken.

In conclusion, the author would like to express his appreciation to Mrs. C. Sansom for typing the thesis.

REFERENCES

1a. Massey, H.S.W. Rep. Prog. Phys. 12 (1949) 248

2a. Landau,L. Phys. Z. Sowjet, 2 (1932) 46.

3a. Zener, C. Proc. Roy. Soc. A137 (1932) 696

4a.i.Hasted J.B. and Chong, A.Y.J. Proc.Phys.Soc. London 80 (1962) 893.

ii.Hasted J.B. and Smith, R.A. Proc.Roy. Soc. A235, (1956) 349.

5a. Bates, D.R. Stewart and Johnston, Proc. Roy . Soc. A258 (1960) 22

6a. Ellison W.D. and Borowitz S. Atomic Collision Processes. Ed. M.R.C. McDowell (1964) 790.

7a. Bates, D.R. Stewart J,and Johnson H. Proc. Phys. Soc. 84 (1964) 517.

8a. Everhart, E. Stone, G. and Carbone, R.J. Phys. Rev. 99 (1955) 1287.

9a. Fedorenko, N.V. Filipenko, L.G. and Flaks, I.P.J. tech.Phys. Moscow, 30 (1960) 49.

1. Rapp D. and Francis, W.E. J.Chem. Phys. 37 (1962) 2631.

2. McCarrol R. Proc. Roy. Soc. A246 (1961) 547.

3. Schiff, H. Canad. J. Phys. 32 (1954) 393.

4. Bransden, B.H. Dalgarno, A. King. N.M. Proc. Roy. Soc. A67 (1954) 1075.

5. Gurnee, E.F. and Magee J.L. J. Chem. Phys. 26 (1957) 1237.

6. Pauling L. and Wilson E.B. Intro' to Quantum Mechanics.McGraw-Hill,1935.

8. Bates D.R. et al. Trans. Roy. Soc. A246(1953) 215.

9. Moiseiwitsch B.L. et al. Proc. Phys. Soc. A69 (1956) 653.

10. Slater J.C. Phys. Rev. 35 (1930) 210.

11. Dalgarno, A. Phil. Trans. Soc. A72 (1958) 694.

12. Popesko, Iovitsu I, and Ionescu-Pallas, N., Soviet Phys. Tech. Phys. 4.(1960) 780.

13. i. Everhart, E. Lockwood, G.J. and Helbig H.F. Phys.Rev. (1963)
ii.Everhart, E. Helbig, H.F. and Lockwood G.J., Atomic Collision Processes. Ed. M.R.C.McDowell (1964) 865.

14. Jones O.R. van Dyk G. Eddy N. Atomic Collision Processes, Ed. M.R.C.McDowell (1964) 862.

15. Fite W.L. Brackmann R.T. and Snow, W.R. Phys. Rev. 112 (1958) 1161.

16. Hasted. J.B. Proc. Roy. Soc. A205 (1951) 421.

17. Kushnir R.M., Palyukh B.M. and Sena L.A. Bull. Acad. Sci. U.S.S.R. Phys. Ser. 23 (1959) 995.

18. Flaks, I.P. and Solov'ev E.S., Soviet Phy.Tech.Phys. 3 (1958) 564.

19. Massey H.S.W. Rep. Prog.Phys. 12 (1949) 248.

20. Gilbody H.B. and Hasted J.B., Proc.Roy. Soc. A238 (1956) 334.

21. Hasted J.B., Advances in Electronics and Electron Physics.13 (1960) 3.

22. Hasted, J.B. and Lee, A.R. Proc. Roy. Soc. A79 (1962) 702.

23. Hasted J.B. and Lee, A.R. Proc. Phys. Soc. 85 (1965) 673.

24. Hasted, J.B. and Stedeford, J.B.H. Proc. Roy. Soc. A227 (1955) 466.

25. Jones P.R. Ziemba F.B. and Moses, H.A. Everhart, E. Phys.Rev. 113 (1959) 182.

26. Fedorenko, N.V. Afrosimov, V.V. and Kaminker D.M. J. Tech. Phys. (U.S.S.R) 26 (1957) 1861.

27. Hasted, J.B. and Smith R.A. Proc. Roy. Soc. A235 (1956) 349.

28. Bates D.R. Johnston H.C. and Stewart J. Proc. Phys. Soc. 84 (1964) 517.

29. Landau L.D. and Lifshitz E.M. Quantum Mechanics, Pergamon Press (1958).

30. Bates, D.R. and Moiseiwitsch B.L. Proc. Phys. Soc. A67 (1954) 805.

31. Bates, D.R. Atomic and Molecular Processes (1962) 608.

32. Landau, L. Phys. Z. Sowjet, 2 (1932) 46.

33. Zener, C., Proc. Roy. Soc. A137 (1932) 696.

34. Bates D.R. and Moiseiwitsch B.L., Proc. Phys. Soc. A67 (1959) 805.

35. Moiseiwitsch B.L., Atmosphere and Terrestial Physics, 23, Spec. Supp. Vol 2, (1955) 23.

36. Hasted J.B., Lee, A.R. Hussain M., Atomic Collision Processes, Ed. M.R.C.McDowell (1964) 802.

37. Hasted. J.B. and Hussain M. Proc. Phys. Soc. 83, (1964) 911.

38. i. Hasted, J.B. and Chong A.Y.J. Proc. Phys. Soc. 80 (1962) 441.
ii. Hasted, J.B. and Smith, R.A. Proc. Phys. Soc. A235 (1956) 349.

39. Dalgarno, A., Proc. Phys. Soc. A67 (1954) 1010.
Bates, D.R. and Lewis, J.T. Proc. Phys. Soc. A68 (1955) 173.

40. Bates, D.R. and Moiseiwitsch, B.L., Proc. Phys. Soc. A67 (1954) 805.
Bates, D.R.and Boyd T.J.M., Proc. Phys. Soc. A69 (1956) 910.

41. Boyd, T.J.M. and Moiseiwitsch,B.L. Proc. Phys. Soc. A70 (1957) 309.

42. Bates, D.R. Proc. Roy. Soc. A258 (1960) 22.

43. Massey, H.W.S. and Burhop, E.H.S. Electronic and Ionic Impact Phen. (1956) Chapter VII and VIII.

44. Allison S.K., Rev. of Modern Phys. 30 (1958) 1137.

45. Allison S.K., Garcia-Munoz, M. Atomic and Molecular Processes 13 (1962) 721.

46. i.Hasted, J.B. Atomic and Molecular Processes 13 (1962) 696.
ii. Advances in Electronics and Electron Physics 13 (1960) 1

47. Keene J.P. Phil. Mag (7) 40 (1949) 369.

48. Gilbody, H.B. and Hasted, J.B. Proc. Roy. Soc. A238 (1956) 334.

49. Dunahoe T.H. and Hushfar F., Phys. Rev. Letters, 3 (1959) 470.
Nature 186 (1960) 1038.

50. Wolf F. Ann.Phys. 23 (1936) 185, 627 : 25 (1936) 527, 737 :
Ann. Phys. 29 (1937) 33.
Ann. Phys. 34 (1938) 341.

51. i. Hasted J.B., Proc. Roy. Soc.A205 (1951) 421.
ii. Proc. Roy. Soc.A212 (1952) 235.

52. Fite W.L., Stebbings R.F and Hummer D.G. J.Chem.Phys. 33 (1960) 1226.

53. Fite W.L. Stebbings R.F. Proc. Roy. Soc. A268 (1962) 527.

54. Fite W.L., Brackmann R.T. and Snow, W.R. Phys. Rev. 112 (1958) 1161.

55. Fedorenko N.V., Afrosimov V.V. J. Tech. Phys. Moscow, 26 (1957) 1872.

56. Fedorenko N.V., and Afrosimov, V.V. J. Tech. Phys. 34 (1958) 1398.

57. Lindholm, E. Proc. Phys. Soc. A66 (1953) 1068.

58. Hasted J.B. Hussain, M. Proc. Phys. Soc. 83 (1964) 911.

59. Morgan G.H. and Everhart E., Phys. Rev. 128 (1962) 667.

60. Stier P.M. and Barnet C.F. Phys. Rev. 96 (1954) 973.

61. Stier P.M. and Barnet C.F. Phys. Rev. 103 (1956) 896.

62. Stier P.M. and Barnet C.F. Phys. Rev. 109 (1958) 385.

63. Allison S.K. Phy. Rev. 110 (1958) 670.

64. Flaks I.P. and Solov'ev E.S. Soviet Phys. Tech. Phys. 3 (1958) 564.

65. Filipenko L.G., Societ Phys. Tech.Phys. 5 (1960) 45.

66. Fogel M., J. Expt. Theo. Phys. 35 (1959) 565.

67. Fogel M., J. Expt. Theo. Phys. 35 (1959) 868.

68. Fogel M., J. Expt. Theo. Phys. 34 (1959) 579.

69. Everhart E. Carbone R.J. and Stone G. Phys. Rev. 98 (1955) 1045.

70. Fuls. E.N., Jones P.R. Ziemba F.P. and Everhart E.R. 107 (1957) 704.

71. Ziemba F.P. Moses H.A. and Everhart E., 113 (1959) 182.

72. i.Fedorenko N.V., Filipenko. L.G. and Flaks I.P. Soviet Phys. Tech. Phys. 5 (1960) 45.
ii.Afrosimov, V.V. Il'in R.N. and Solov'ev, Soviet Phys. Tech.Phys. 5 (1960) 661.

73. Ardienne von M., Phys. Z. 43 (1942) 91.

74. i.Heil, H., Z. Phys. 120 (1944) 212.
ii.Finkelstein, A.T. and Smith L.P., Rev. Sci. Instrum. 11 (1940) 94.

75. Hasted, J.B. and Chong, A.Y.J., Proc. Phys. Soc. 80 (1962) 441.

76. Bohm, D. Burhop, E.H.S. and Massey, H.S.W. Gaseous Discharges in Magnetic Fields, Chap.II. (1949) McGraw-Hill,N.Y.

77. Barnard, B.P. Mass Spectrometer Researches, National Physical Laboratory, H.M. Stationery Office (1956).

78. Willmore, A.P. Thesis. University of London (1955).

79. Klemperer, O. Electron Physics. Butterworths, London (1961) Chapter 3.

80. Everhart, E. Lockwood, G.J. and Helbig, H.F. Phy. Rev. (1963)

81. Jones, P.R. van Dyk G. and Eddy N., Atomic Collision Processes, Ed. M.R.C. McDowell (1964) 862.

82. Angel, D.W. Cooper,H.W. Hunter, W.R. and Tousey, R. "Extreme Ultraviolet Detection with the Bendix Single Channel Photomultiplier". Paper presented at the Image Intensifier Symposium, Fort Belvoir, Virginia, 24-26, October 1961.

82a. Evan D.S., Rev. Sci. Instrum. 36 (1965) 375.

83. Massey, H.S.W. and Mohr,C.B.O., Proc. Roy. Soc. A144 (1934) 188.

84. Bates, D.R. Cook, C.J. and Smith, F.J., Proc. Phys. Soc. 83 (1964) 49.

85. London, F., Z. Phys. 63 (1930) 245.

86. Dalgarno, A. Atomic Polarisabilities and Shielding factor. National Aeronautics and Space Administration (1963).

87. Bohme, D.K. and Ong, P.P., (Private Communication).